

WL-TR-94-1038

COMPARISON OF COHERENT TO INCOHERENT
DETECTION AT 2.09 μm USING A SOLID STATE
LADAR SYSTEM

AD-A277 159



JAY A. OVERBECK

AVIONICS DIRECTORATE
WRIGHT LABORATORY
AIR FORCE MATERIEL COMMAND
WRIGHT PATTERSON AFB OH 45433-7409

FEBRUARY 1994

FINAL REPORT FOR 03/27/91-09/21/93

DTIC
ELECTED
MAR 21 1994
S E D

APPROVED FOR PUBLIC RELEASE; DISTRIBUTION IS UNLIMITED.

94-08820



AVIONICS DIRECTORATE
WRIGHT LABORATORY
AIR FORCE MATERIEL COMMAND
WRIGHT PATTERSON AFB OH 45433-7409

DTIC QUALITY INSPECTED 1

94 3 18 0 69

NOTICE

When Government drawings, specifications, or other data are used for any purpose other than in connection with a definitely Government-related procurement, the United States Government incurs no responsibility of any obligation whatsoever. The fact that the Government may have formulated or in any way supplied the said drawings, specifications, or other data, is not to be regarded by implication, or otherwise in any manner construed, as licensing the holder, or any other person or corporation; or as conveying any right or permission to manufacture, use or sell any patented invention that may in any way be related thereto.

This report is releasable to the National Technical Information Service (NTIS). At NTIS, it will be available to the general public, including foreign nations.

This technical report has been reviewed and is approved for publication.

Jay A. Overbeck
JAY A. OVERBECK, Contractor, T/SSI
Electro-Optics Techniques Group
Electro-Optics Branch

Donald L. Tomlinson
DONALD L. TOMLINSON, Chief
Electro-Optics Techniques Group
Electro-Optics Branch

Paul F. McManamon
PAUL F. McMANAMON, Acting Chief
Mission Avionics Division
Avionics Directorate

Accession For	
NTIS	CRA&I
DTIC	TAB
Unannounced	
Justification	
By _____	
Distribution /	
Availability Codes	
Dist	Avail and/or Special
A-1	

If your address has changed, if you wish to be removed from our mailing list, or if the addressee is no longer employed by your organization, please notify WL/AARI-2, Wright-Patterson AFB OH 45433-7700, to help maintain a current mailing list.

Copies of this report should not be returned unless return is required by security considerations, contractual obligations, or notice on a specific document.

REPORT DOCUMENTATION PAGE

Form Approved
OMB No. 0704 0188

Public reporting burden for this collection of information is estimated to be 1 hour per report. In addition, the time for review is estimated to be 1 hour per report. This burden includes the time for reviewing instructions, gathering information, and completing and reviewing the information and comments required for this collection. (Aeronautics Directorate, Washington Headquarters Services, Directorate for Information Operations and Resources, 1215 Jefferson Davis Highway, Suite 1200, Arlington, VA 22202-4302, and to the Office of Management and Budget, Paperwork Reduction Project 0704-0188, Washington, DC 20585.)

1. AGENCY USE ONLY (Leave blank)	2. REPORT DATE	3. REPORT TYPE AND DATES COVERED	
		Final Report 27 Mar 91 - 21 Sep 93	
4. TITLE AND SUBTITLE Comparison of Coherent to Incoherent Detection at 2.09μm Microns Using a Solid State Ladar System			5. FUNDING NUMBERS
			C PE 62204 PR 0100 TA AA WU 16
6. AUTHOR(S) Jay A. Overbeck			8. PERFORMING ORGANIZATION REPORT NUMBER
7. PERFORMING ORGANIZATION NAME(S) AND ADDRESS(ES) AVIONICS DIRECTORATE WRIGHT LABORATORY AIR FORCE MATERIEL COMMAND WRIGHT PATTERSON AFB OH 45433-7409			10. SPONSORING / MONITORING AGENCY REPORT NUMBER WL-TR-94-1038
9. SPONSORING / MONITORING AGENCY NAME(S) AND ADDRESS(ES) AVIONICS DIRECTORATE WRIGHT LABORATORY AIR FORCE MATERIEL COMMAND WRIGHT PATTERSON AFB OH 45433-7409			
11. SUPPLEMENTARY NOTES			
12a. DISTRIBUTION / AVAILABILITY STATEMENT Approved for public release; distribution is unlimited.		12b. DISTRIBUTION CODE	
13. ABSTRACT (Maximum 200 words) A 2.09 LADAR system has been built to compare coherent to incoherent detection. The 2.09 um wavelength is of interest for its high atmospheric transmission and because it is eye safe. The 2.09um system presented within is capable of either a coherent or incoherent operational mode, is tunable in a small region around 2.09um, and is being used to look at the statistical nature of the LADAR return pulses for typical glint and speckle targets. In order to compare coherent to incoherent detection the probability of detection will be investigated as the primary performance criterion of interest. The probability of detection is dependent on both the probability of false alarm and the probability density function representing the signal current output from the detector. These probability distributions are different for each detection technique and for each type of target. Furthermore, the probability of detection and the probability of false alarm are both functions of the dominating noise source(s) in the system. A description of the theoretical expectations of this system along with the setup of the LADAR system and how it is being used to collect data for both coherent and incoherent detection will be presented.			
14. SUBJECT TERMS Coherent detection, incoherent detection, lidar, ladar		15. NUMBER OF PAGES 128	
16. PRICE CODE			
17. SECURITY CLASSIFICATION OF REPORT UNCLASSIFIED		18. SECURITY CLASSIFICATION OF THIS PAGE UNCLASSIFIED	
19. SECURITY CLASSIFICATION OF ABSTRACT UNCLASSIFIED		20. LIMITATION OF ABSTRACT UNLIMITED	

FOREWORD

This Technical Report was prepared by the Electro-Optics Techniques Group, Electro-Optics Branch, Mission Avionics Division, Wright Laboratory, Wright-Patterson Air Force Base, Ohio.

The following personnel contributed to the formulation and review of this report:

Jay A Overbeck, T/SSI

This Technical Report was submitted by Jay A Overbeck in February 1994.

TABLE OF CONTENTS

APPROVAL.....	ii
REPORT DOCUMENTATION	iii
FOREWORD	iv
TABLE OF CONTENTS	v
LIST OF FIGURES.....	ix
LIST OF TABLES	xiii
LIST OF VARIABLES	xiv
1.0 INTRODUCTION.....	1
2.0 EYE SAFE LADAR REQUIREMENTS	5
3.0 THEORY	8
3.1 Noise Sources	10
3.1.1 Shot Noise.....	10
3.1.2 Dark Current Noise	11
3.1.3 Johnson Noise	11
3.1.4 Background Noise	12
3.1.5 Amplifier Noise.....	12
3.2 Probability Distributions of Noise	13
3.2.1 Probability Distribution of Noise for Incoherent Detection	13
3.2.2 Probability Distribution of Noise for Coherent Detection.....	14
3.3 PDF's Representing the Combination of Signal and Noise.....	14
3.3.1 The PDF's for Incoherent Detection	15
3.3.1.1 Glint Targets	15

3.3.1.2 Speckle of Diffuse Targets	17
3.3.2 Probability Distribution for Coherent Detection.....	20
3.3.2.1 A Speckle/Diffuse Target	21
3.3.2.2 A Glint/Specular Target	22
3.4 The Probability of False Alarm	23
3.4.1 The Probability of False Alarm for Incoherent Detection	24
3.4.2 The Probability of False Alarm for Coherent Detection	25
3.5 The Probability of Detection.....	25
3.5.1 The Probability of Incoherent Detection.....	26
3.5.1.1 The Probability of Incoherent Detection with a Glint Target.....	26
3.5.1.2 The Probability of Incoherent Detection for a Speckle Target.....	27
3.5.2 The Probability of Coherent Detection	28
3.5.2.1 The Probability of Coherent Detection with a Glint Target.....	28
3.5.2.2 The Probability of Coherent Detection with a Speckle Target.....	28
4.0 SYSTEM CONFIGURATION	30
4.1 System Layout	30
4.1.1 Master Oscillator	30
4.1.2 Slave Oscillator.....	32
4.2 Detection Scheme	39
5.0 THEORETICAL COMPUTATIONS	43
5.1 Evaluation of Noise in the 2 μm LADAR System	43
5.1.1 Dark Current Noise	44
5.1.2 Johnson Noise	44

5.1.3	Background Noise	45
5.1.4	Amplifier Noise.....	46
5.1.5	Shot Noise.....	47
5.1.5.1	Shot Noise in the Coherent Detection Case	48
5.1.5.2	Shot Noise in the Incoherent Detection Case	50
5.2	Calculation of the Probability of False Alarm	53
5.2.1	The Probability of False Alarm for Incoherent Detection	53
5.2.2	The Probability of False Alarm for Coherent Detection	54
5.3	Calculation of the Probabilities of Detection	55
5.3.1	Calculation of the Probability of Incoherent Detection with a Glint Target	55
5.3.2	Calculation of the Probability of Incoherent Detection with a Speckle Target.....	56
5.3.3	Calculation of the Probability of Coherent Detection with a Glint Target	58
5.3.4	Calculation of the Probability of Coherent Detection with a Speckle Target.....	59
5.3.5	Comparison of Coherent to Incoherent Detection for a Glint Taget Using the Probability of Detection.....	60
5.3.6	Comparison of Coherent to Incoherent Detection for a Speckle Taget Using the Probability of Detection.....	61
6.0	EXPERIMENTAL PLAN	64
6.1	Required Data	64
6.2	Data Acquisition	66
6.2.1	Targets Used	66
6.2.2	Data Format	66
6.2.3	Data Collection.....	70

6.3 Experimental Procedure	70
7.0 ANALYSIS OF DATA.....	72
7.1 Peak Detection.....	72
7.2 Comparison of Data with Theoretical Expectations	73
7.2.1 Normalization of Transmitted Pulse	73
7.2.2 Chi ² Goodness of Fit Test.....	74
7.2.3 Analysis of Incoherent Detection with a Speckle Target.....	75
7.2.4 Analysis of Incoherent Detection with a Glint Target	81
7.2.5 Analysis of Coherent Detection with a Speckle Target	85
7.2.6 Analysis of Coherent Detection with a Glint Target.....	89
7.2.7 Analysis on the Probability of Detection.....	95
8.0 CONCLUSIONS AND RECOMMENDATIONS.....	97
8.1 List of Original Contributions.....	100
APPENDIX A	101
APPENDIX B	106
BIBLOGRAPHY	109
VITA	112

LIST OF FIGURES

Figure 1: Probability density functions representing both signal and noise distributions with graphical representation of the probabilities of detection, false alarm and miss	8
Figure 2: Poisson distributions with different mean values.	16
Figure 3: Comparison between Poisson and a Gaussian distribution.....	16
Figure 4: This is an example of the distribution of the return energy and the noise for incoherent detection with a speckle target.	19
Figure 5: A Rician distribution with different components of diffuse and glint targets.....	20
Figure 6: This shows a Rayleigh probability density with an increasing diffuse component.....	22
Figure 7: A Rician distribution for a totally glint target (no diffuse component).....	23
Figure 8: Layout of LADAR system.....	31
Figure 9: Description of output coupling from slave oscillator.	33
Figure 10: Energy level diagram for Cr,Tm,Ho:YAG, laser rod.	35
Figure 11: Slave oscillator long pulse output.	36
Figure 12: Slave oscillator output when Q-switched.	37
Figure 13: One side of Airy disk pattern.	40
Figure 14: Theoretical heterodyne efficiency.	41
Figure 15: Detection package from CTI.	42

Figure 16: Spectrum analyzer display of output of coherent detection electronics using a 10 Hz resolution bandwidth.....	49
Figure 17: Spectrum analyzer output of coherent detection electronics with 1.25 mW of power incident on the detector	50
Figure 18: Curves representing the probability of detection for incoherent detection with a glint target for various probabilities of false alarm.....	57
Figure 19: Curves representing the probability of detection for incoherent detection with a speckle target for various probabilities of false alarm.....	58
Figure 20: Curves representing the probability of detection for coherent detection with a glint target for various probabilities of false alarm.....	59
Figure 21: Curves representing the probability of detection for coherent detection with a speckle target for various probabilities of false alarm.....	60
Figure 22: Comparison of the probability of detection for coherent vs. incoherent detection with a glint target.....	61
Figure 23: Comparision of the probability of detection for coherent vs. incoherent detection with a speckle target.	63
Figure 24: Fluctuation in output energy of slave oscillator.....	65
Figure 25: Coherent return as seen on the Tektronix DSA 602A oscilloscope.....	67
Figure 26: Fourier Transform of coherent waveform.	68
Figure 27: Output of incoherent detection electronics.....	68
Figure 28: Average Transmitted pulse energy as displayed on the DSA 602A oscilloscope.....	69
Figure 29: Incoherent detection with the lambertian (speckle) target. This data was taken on April 12, 1993.	76

Figure 30: Theoretical fit to data taken using incoherent detection with the lambertian (speckle) target on April 12, 1993. There are 449 data points in this figure.....	79
Figure 31: Theoretical fit to data taken using incoherent detection with the lambertian (speckle) target on April 12, 1993. There are 898 data points in this figure.....	80
Figure 32: Theoretical fit to data taken using incoherent detection with flame sprayed aluminum target on April 8, 1993. There are 898 data points in this figure.....	80
Figure 33: Theoretical fit to data taken using incoherent detection with the lambertian target on April 15, 1993. There are 449 data points in this figure.....	81
Figure 34: Data taken using incoherent detection with the corner cube reflector.....	82
Figure 35: Incoherent detection with the bicycle reflector (glint) target. This data was taken on April 7, 1993 at 9:20am. There are 449 data points.....	83
Figure 36: Incoherent detection with the bicycle reflector (glint) target. This data was taken on April 7, 1993.....	84
Figure 37: Incoherent detection with the bicycle reflector (glint) target. This data was taken on April 22, 1993.....	84
Figure 38: Coherent detection with the lambertian target taken on April 1, 1993. Shown is the best fit Rayleigh distribution with a χ^2 of 48.7 with 27 degrees of freedom. (Needs to be less than 36.7).....	86
Figure 39: Coherent detection with the lambertian target taken on April 12, 1993. There are 898 data points. This is the best fit Rayleigh probability distribution which gives a $\chi^2=450$	87
Figure 40: Data taken April 1, 1993 with log-normal distribution used as best fit curve, $\sigma=0.05$, $\chi^2=22.5$ with 27 degrees of freedom.....	88
Figure 41: Data taken April 12, 1993, with best fit log-normal, $\sigma=0.055$, $\chi^2=19.2$ with 29 degrees of freedom.....	89
Figure 42: Data taken with a glint target on April 5, 1993.	91

Figure 43: Data taken with a glint target on April 7, 1993.	91
Figure 44: Data taken with a glint target on April 8, 1993. There are 1353 data points in this histogram.	92
Figure 45: Theoretical probability distribution for coherent detection with a glint target for data taken on April 5. Chi ² =37.0 with 30 degrees of freedom; good fit to data.	93
Figure 46: Theoretical probability distribution for coherent detection with a glint target for data taken on April 7. Chi ² =41.8 with 29 degrees of freedom; this is a poor fit to theory.....	93
Figure 47: Coherent detection data taken from a glint target on April 8th. The theoretical fit gives a chi ² =76 with 49 degrees of freedom. This is a poor fit to the experimental data.	94

LIST OF TABLES

Table 1: Exposure limits for direct exposure to a laser beam for IR-B&C wavelengths.....	6
Table 2. Summary of values for background noise calculation.	46
Table 3: Data used to obtain an estimate of the return power from the target.....	51
Table 4: Summary of theoretically calculated values for the discussed noise sources	52
Table 5: Threshold currents for different probabilities of false alarm for incoherent detection.....	54
Table 6: Threshold currents for different probabilities of false alarm for coherent detection.....	55
Table 7: Comparison of calculated and measured probabilities of detection for coherent detection with a speckle target.	95
Table 8: Comparison of calculated and measured probabilities of detection for incoherent detection with a speckle target.	96
Table B1: Tabulated values of Chi ²	107

LIST OF VARIABLES

α^2	$\sigma_\beta^2/(2 - \frac{\gamma}{\eta})$
$\langle i_{Glint} \rangle$	average current produced by the return energy from a glint target
$\langle n \rangle$	average noise
θ_s	beam divergence
σ_{Exp}^2	experimentally measured variance
$\langle W \rangle$	mean return energy
$\langle i_{Dominating Noise}^2 \rangle$	mean squared dominating noise
$\langle i_{Coh,SN}^2 \rangle$	mean squared shot noise current for coherent detection
$\langle i_{Coh,SN}^2 \rangle$	mean squared shot noise current for coherent detection
$\langle i_{Incoh,SN}^2 \rangle$	mean squared shot noise current for incoherent detection
$\langle i_{Diffuse}^2 \rangle$	mean squared signal current from a diffuse target
$P_s(k W)$	Poisson PDF representing k signal photoelectrons being emitted by the detector
Δt	pulse length
σ^2	variance
σ_β^2	variance of the data
γ	heterodyne efficiency
μ	mean of negative binomial distribution
ν	optical frequency
η	quantum efficiency of the detector
θ	variable in negative binomial distribution
λ	wavelength
χ^2	chi ² statistic
$\langle k \rangle$	average number of photoelectrons emitted by the detector
a	limiting optical aperture
A_R	area of the receiver
b	$\eta/h\nu$

c	number of classes
D	diameter of the receiver
D_B	diameter of laser beam
$\Delta\lambda$	wavelength band of the optical bandpass filter
E_{Actual}	actual radiant exposure
E_j	expected (theoretical) frequency
E_{Limit}	exposure limit
f	focal length
$F_r()$	frustration function
g	i_{Glint}/σ
h	Plank's constant
η_{ATM}	atmospheric transmission factor
η_{SYS}	optical efficiency of the LADAR system
i	the instantaneous detector output current
i_N	individual peak data point
i_{Glint}	current amplitude of the signal from a glint target
I_0	zeroth order modified Bessel function of the first kind
i_T	threshold current
j	index variable
$J_0(x)$	zero order Bessel function
$J_1(x)$	first order Bessel function
k	number of photoelectrons emitted by the detector
k_I	fraction of solar radiation that penetrates the Earth's atmosphere
k_w	wave number
m	mean
M	number of spatial correlation cells received by the detector
n	index variable
O_j	observed frequency (experimentally measured)
$p(W)$	probability density function of the return energy
$P_{CG\ Bin}$	probability function for coherent detection with a glint target over a bin
$p_{CG}(i)$	PDF for coherent detection with a glint target representing the fluctuation in the detector output current
$P_{co}(i)$	probability density function representing noise for coherent detection
P_{coFA}	probability of false alarm for coherent detection
$P_{CS\ Bin}$	probability function for coherent detection with a speckle target over a bin

$p_{CS}(i)$	PDF for coherent detection with a speckle target representing the fluctuation in the detector output current
Pd_{CG}	probability of detection for coherent detection with a glint target
Pd_{CS}	probability of detection for coherent detection with a speckle target
Pd_{IG}	probability of detection for incoherent detection with a glint target
Pd_{IS}	probability of detection for incoherent detection with a speckle target
$P_{IG\ Bin}$	probability function for incoherent detection with a glint target over a bin
$p_{IG}(i)$	PDF for incoherent detection with a glint target representing the fluctuation in the detector output current
$P_{in}(i)$	probability density function representing noise for incoherent detection
P_{inFA}	probability of false alarm for incoherent detection
$p_{IS}(i)$	PDF for incoherent detection with a speckle target representing the fluctuation in the detector output current
$P_{S+N}(k/W)$	PDF representing fluctuation in detection circuit caused by signal and noise for incoherent detection with a speckle target
P_{SB}	power incident on the detector produced by solar backscatter
P_T	transmitted power
P_x	cumulative probability distribution
P_x	log-normal density function
q_R	radius of airy disk
r	radius of detector
R	range to the target
ρ	reflectivity of the target
ρ	target reflectivity
R_{Det}	responsivity of the detector
R_i	distance from aperture to image
σ	target cross section given as $\sigma_T = \pi \rho R^2 \theta_B^2$
S_{IRR}	solar irradiance
t	pulse length
W	return energy from target
w	variable in negative binomial distribution
Ω_R	solid angle over which energy radiates from a radiating body
x	$k_W a q_R / R_i$
x_T	threshold current expressed in terms of photoelectrons
y	$\pi r D_B / f \lambda$

CHAPTER I

1.0 INTRODUCTION

To demonstrate Maxwell's theory, that light waves and radio waves will behave in a similar fashion, Heinrich Hertz, in 1886, experimentally reflected radio waves (66cm) off of a metallic surface. By demonstrating that light waves and radio waves are both part of the electromagnetic spectrum and can be reflected off metallic or dielectric bodies, Hertz set the stage for radar technology[1]. The first RADAR (RAdio Detection And Ranging) systems were used to warn of approaching hostile aircraft in the 1930's but with the invention of the laser in 1960, distance and velocity could be measured more accurately because of the shorter wavelengths that light provides over those provided with conventional radar.

The first laser radar systems were known as LIDAR (Light Detection And Ranging) systems. Although it was recognized that the Light was laser light, work has been done with Xenon and other flash lamps so the name has been changed to LADAR (LAser Detection And Ranging) [2] when referring specifically to laser light. Laser range finders were first used in many aspects of the Vietnam war; ground troops used hand held lidars, lidars were mounted on tanks to aid in measuring distances, and "smart" bombs used lasers to track targets. Other applications for laser radars include remote target tracking, aircraft altimeters, and atmospheric studies including wind profiling and pollution monitoring [3].

Ladar wavelengths commonly used today are $10.6\mu\text{m}$ (CO_2), $1.06\mu\text{m}$ (Nd:YAG), and, recently, $2.09\mu\text{m}$ (Tm, Ho:YAG), where the information in parentheses indicates the appropriate gain medium used for the corresponding wavelengths. In 1968, Raytheon demonstrated the first coherent detection ladar system [4] using a CO_2 laser. Coherent detection differs from direct detection in that the return frequency shifted signal is mixed with a reference signal called a local oscillator. This produces a beat signal that is easier to detect than just the return from a target. CO_2 ladars are used in the coherent mode of operation because of the background noise produced by the environment at $10.6\mu\text{m}$. To partially reduce this background noise, the optics used in a CO_2 system, along with the detectors, have to be cooled with liquid nitrogen. This, along with the heavy rf power supplies, make CO_2 systems heavy and expensive to operate [5].

Nd:YAG ladar systems are being used because they are solid state systems. They do not, however, have the efficiencies or the output energies of the $10.6\mu\text{m}$ CO_2 systems, though, as they are solid state systems they are light-weight and less expensive to produce. There are also efficient detectors at this wavelength that do not require cooling with liquid nitrogen and the laser source is continuously tunable over a few nanometer region [5]. CO_2 systems are also tunable but only to other discrete molecular lines. All solid state $1.06\mu\text{m}$ ladar systems were direct detection systems until 1986 when Stanford University successfully demonstrated coherent detection of signals from clouds and atmospheric aerosols particles [6]. A more efficient second generation Nd:YAG ladar system was built in 1988-89 by Coherent Technologies, Inc. (CTI) in Boulder, Colorado. The experimental design is such that the system is more operational and the data analysis is more real time than the system built by Stanford University. CTI has used their system to do atmospheric absorption studies and wind profiling. At this time it is the only known, mobile coherent $1.06\mu\text{m}$ Nd:YAG ladar system [7].

In 1987 the U.S. Air Force approached CTI about designing an eye safe, coherent, solid state ladar system. The primary desire for an eye safe system is so that a pilot will

not blind his wing man, or other personnel, when he has his ladar system engaged. This is just an example of a scenario in which it would be desirable to have an eye safe system. The wavelength chosen by CTI was 2.09 μm because materials have been developed that emit in the 2.09 μm region. These materials can be efficiently pumped using laser diodes, and there are high quantum efficiency detectors as well as a high atmospheric transmission in that region [6]. Along with CTI's 1.06 μm system their 2.09 μm system is used to do wind profiling, range-resolved wind velocity and aerosol backscatter measurements. Until now CTI had the only operating 2.09 μm coherent ladar system [6].

CTI then released its research to Wright Research and Development Center at Wright-Patterson Air Force Base, Ohio in 1990. Their 2.09 μm system has been duplicated and is being used to compare coherent (i.e. heterodyne) detection to incoherent (i.e. direct) detection at 2.09 μm . In 1966, J. W. Goodman compared the detection techniques for wavelengths shorter than 1 μm . He found that when there is a large amount of background noise, coherent detection systems have greater sensitivity. Coherent systems also perform better than incoherent systems when high velocity resolution is needed. However incoherent systems perform with higher signal-to-noise ratios than coherent systems when operated in low noise environments, such as space based applications, and at small rates of false alarm [8]. Robert J. Keyes' analysis in 1986 found that incoherent detection could perform with nearly the same signal-to-noise ratio or even higher signal-to-noise ratio than coherent detection for wavelengths in the near-infrared and visible regions. In the mid- to far-infrared regions the detection schemes gave similar results [9]. A comparison of the detection techniques, however, has never been done for a coherent solid state system and it has never been done specifically at 2.09 μm which is in the mid-infrared region.

The comparison of the detection techniques will be done using a 2 μm ladar system that is capable of both coherent and incoherent modes of operation. The comparison is made based on the probability of detection for each detection scheme as an analysis of this

type has not yet been performed for an eye safe coherent solid state ladar system. The probability of detection is a function of the statistics of detected light returning from a distant target. These statistics are dependent on the type of target, the detection scheme, the electronics in the detection circuit and the types of noise in the system. An analysis of these factors is pursued in this text to compare the detection techniques.

CHAPTER II

2.0 Eye safe LADAR Requirements

For a system to be considered eye safe, direct exposure to the transmitted laser beam must not damage the eye under normal conditions. Different parts of the eye are sensitive to different wavelengths of light. For example, the retina is sensitive to visible light (400-700nm) and IR-A (700-1400nm) radiation, whereas, the lens, aqueous humor and cornea absorb UV (200-400nm), IR-B (1.4-3 μ m) and IR-C (3-1000 μ m) wavelengths. At 2.09 μ m, the cornea absorbs about 75% of the incident energy, while the remaining 25% is absorbed by the aqueous humor. The primary mechanisms, then, by which the eye may be damaged by 2.09 μ m radiation are excess heat generation in the mostly water based aqueous humor and, more importantly, the formation of corneal cataracts [8]. Limits must therefore be set with regard to exposure duration and intensity so as to minimize eye damaging effects.

The American National Standards Institute (ANSI) has issued standards for maximum permissible exposure (MPE), which is defined as the radiant exposure which individuals may receive without harmful biological effects [8]. Since damage to the eye depends on the wavelength and the exposure duration, the standards vary according to wavelength and exposure time. For IR-B&C wavelengths, the standards are given in Table 1.

For our system (see Fig. 9, which will be more fully described later) the beam internal to the system will damage the eye. Once the system is aligned the only beam that

Table I:
Exposure limits for direct exposure to a laser beam for IR-B&C wavelengths.

Wavelength	Exposure Time (t) seconds	Exposure Limits
1.4μm to 10 ³ μm	10 ⁻⁹ to 10 ⁻⁷	10 ⁻² J/cm ²
1.4μm to 10 ³ μm	10 ⁻⁷ to 10	0.56·4√t J/cm ²
1.4μm to 10 ³ μm	10 to 3×10 ⁴	0.1 W/cm ²

escapes the system is the expanded transmitted beam. The exposure limit for this transmitted pulse of length 500 ns is [8]

$$\begin{aligned}
 E_{Limit}(t) &= 0.56 \cdot 4\sqrt{t} \text{ J/cm}^2 \\
 E_{Limit}(t) &= 0.56 \cdot 4\sqrt{500 \times 10^{-9}} \text{ J/cm}^2 \\
 &= 1.489 \times 10^{-2} \text{ J/cm}^2 \\
 &= 14.9 \text{ mJ/cm}^2.
 \end{aligned} \tag{2.1}$$

For our system with a typical transmitted energy of 15 mJ, with an expanded beam diameter of 4 cm at the exit aperture of the telescope, the radiant exposure an individual would receive by glancing into the exit aperture of the telescope can be calculated as

$$\begin{aligned}
 E_{Actual} &= \frac{(\text{Output Energy})}{(\text{Area of Beam})} \\
 &= \frac{15 \text{ mJ}}{4^2 \pi \text{ cm}^2} = 0.298 \text{ mJ/cm}^2,
 \end{aligned} \tag{2.2}$$

for a single pulse. This is only 2% of the single pulse MPE of 14.9 mJ/cm² for this system, according to ANSI standards [8].

In order to assess the effects of extended exposure to 2.09μm radiation, the laser hazard assessment program LHAZ, developed by Armstrong Laboratory according to ANSI standard 136.1-1986, has been used [9]. According to this program, an individual could stare directly into the exit aperture of the telescope of our system (see Figure 9) for 8.3 hours and only receive 68% of the extended MPE of 71.5 J/cm². Based then on single

pulse and extended exposure limits our 2.09 μm LADAR system is considered to be eye safe with respect to the transmitted laser radiation.

By contrast, using the same pulse duration, beam diameter and pulse energy, the single pulse MPE is given by ANSI to be 5 $\mu\text{J}/\text{cm}^2$ for 1.06 μm radiation [9]. The actual radiant exposure from a single pulse (0.298 mJ/cm^2) would thus be enough to damage the eye at this wavelength. For this reason, a comparable 1.06 μm LADAR system would not be considered eye safe. However, the transmitted beams of CO₂ LADARs, under the same conditions as considered for the 2.09 μm system, are eye safe since the single pulse MPE is the same as for 2.09 μm [9], as can be seen in Table 1. As discussed previously, though, CO₂ systems do not have the tuneability of the 2.09 μm systems allowing for tuning around atmospheric absorption lines and unlike solid state systems they have to be cooled with liquid nitrogen.

CHAPTER III

3.0 THEORY

The comparison of coherent to incoherent detection will be performed assuming both a speckle and a glint target. The basis for this comparison will be the probability of detection. To understand the probability of detection, the role of the statistical nature of the noise and the return signal plus noise must first be understood. The noise distribution shown in Fig. 1 [1] is the probability density function (PDF) that represents, generally, the fluctuation of the noise current in a radar system when there is no target present.

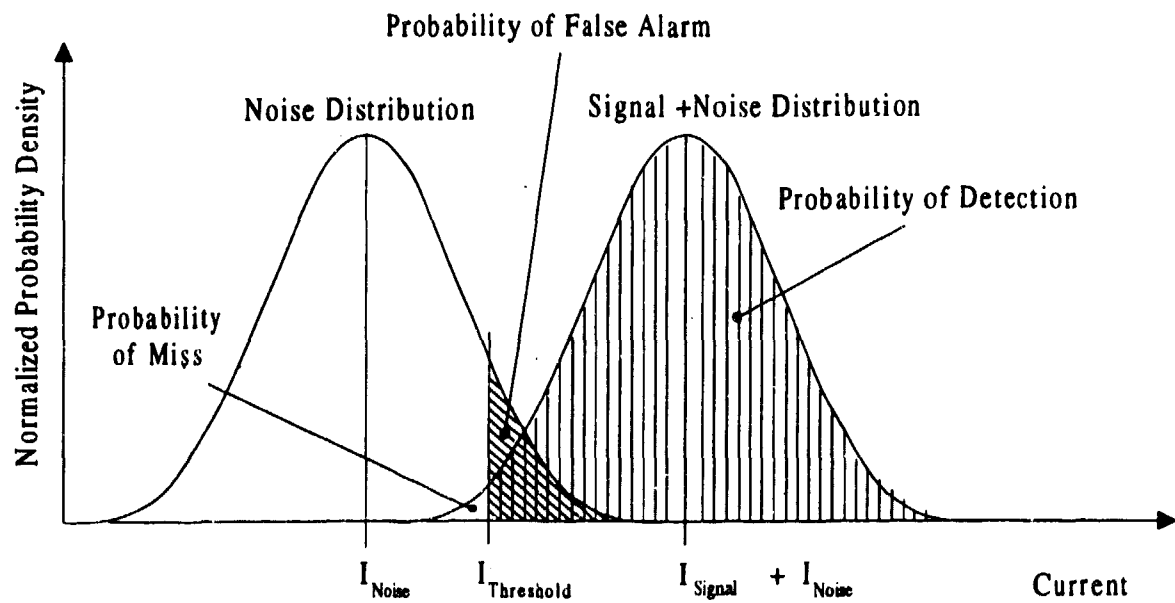


Figure 1: Probability density functions representing both signal and noise distributions, with graphical representation of the probabilities of detection, false alarm and miss.

The shape and the position of this probability distribution is dependent on the detection technique used and on the average value of the noise current, I_{Noise} . When a signal is present, the average value of the signal current I_{Signal} is generally greater than the average value of the noise current, so that the PDF representing the fluctuation in the combined return signal, plus noise current, is centered about an average value of the return signal plus noise. The second distribution shown in Fig. 1 represents, generally, the sum of the signal and noise currents.

In order to decide whether a value measured by the detector is from an actual target or whether it is noise, a threshold current $I_{Threshold}$ is set as shown in Fig. 1. Whenever a current produced by the detector is larger than the threshold current, a target is said to have been detected. Whether or not a real target exists has yet to be determined. The probability that a target has been detected is called the probability of detection, which is, mathematically, the area under the PDF for the signal and noise greater than the set threshold. There is also the probability that the current produced by the detector exceeds the threshold due to noise effects only. The probability of this occurring is called the probability of false alarm and is, mathematically, the area under the noise current distribution greater than the set threshold current. And finally, there is a small, undesirable possibility that a signal from a real target can produce a detected current less than the threshold current, causing the target not to be detected. This is called the probability of miss.

In order to find the probability of detection for the $2.09 \mu\text{m}$ LADAR system the average value of the dominating noise source(s) needs to be determined as will be discussed in the following section. The PDF that the dominating noise source(s) exhibit will then be discussed for both coherent and incoherent detection. The probability distributions of the noise will then be used in conjunction with desired probabilities of false alarm to find the needed threshold for that false alarm rate. The PDF representing the

fluctuations in the detector output caused by the type of target and the detection process will then be identified for a glint and a speckle target for both coherent and incoherent detection. Once these four distributions are identified, the threshold values found when calculating the probabilities of false alarm will be used with the PDF's representing the fluctuation in the detector output current to calculate the corresponding probabilities of detection.

3.1 Noise Sources

When trying to detect a signal there is always noise present. Electrically, noise is expressed as a mean squared current or voltage fluctuation around a DC value, which is also called the variance. This noise may be generated by the randomness associated with the detection of a signal (shot noise), the leakage current from the detector (dark current noise), or the current flowing through a resistor in the detection circuit (thermal noise or Johnson noise). Other sources of noise are stray light striking the detector that is not from the intended source (background noise), and noise in the post-detection circuit caused by an amplifier (amplifier noise). The following is a discussion of these noise sources.

3.1.1 Shot Noise

Shot noise is the fluctuation in the current due to the discrete nature in which charge carriers are produced. This fluctuation can be seen if a DC current is looked at on a short time scale. This fluctuation has a Poisson probability density function where the variance is equal to the mean [10]. The mean squared current fluctuation seen at the output of an electronic filter coupled with the detector is (see Appendix A) [10]

$$\langle i_{SN}^2 \rangle = 2qIB, \quad (3.1.1)$$

where q is the charge on an electron, I is the average current and B is the electrical bandwidth of the detection circuit determined by the electrical filter.

3.1.2 Dark Current Noise

The dark current of a detector is the leakage current produced when there is no energy incident of the surface of the detector. This leakage current is always there and the value of the leakage current differs from detector to detector even if the detectors were produced in the same batch. The equation for the mean square value of the dark current noise is the same as the equation for shot noise [11] except I_{Dk} is used to represent the average dark current , that is

$$\langle i_{Dk}^2 \rangle = 2qI_{Dk}B \quad (3.1.2)$$

3.1.3 Johnson Noise

Johnson noise or thermal noise is fluctuation caused by the thermal motion of charge carriers in a dissipative element. An example of a dissipative element that produces thermal noise is the resistive load used to measure the signal. The equation used to calculate the mean squared Johnson noise is [11]

$$\langle i_j^2 \rangle = \frac{4kTB}{R_{Load}}, \quad (3.1.3)$$

where k is Boltzman's constant, T is the temperature of the element in Kelvin, and R_{Load} is the resistance of the load as seen by the detector.

3.1.4 Background Noise

Another source of noise in a ladar system is background noise. Background noise is the shot noise produced by the detection of radiation that has reflected off or comes from the earth, clouds, the atmosphere and the sun. The shot noise current produced by the background is [4]

$$\langle i_{Bk}^2 \rangle = 2qBP_{SB}R_{Det}, \quad (3.1.4)$$

where R_{Det} is the responsivity of the detector and P_{SB} is the power incident on the detector produced by solar backscatter. The power from solar backscatter, P_{SB} , has been shown to be [4]

$$P_{SB} = k_1 S_{IRR} \Delta\lambda \Omega_R \rho \eta_{SYS} A_R, \quad (3.1.5)$$

where k_1 is the fraction of the solar radiation that penetrates the Earth's atmosphere, S_{IRR} is the solar irradiance, Ω_R is the solid angle over which energy radiates from the radiating body, ρ is the target reflectivity, η_{SYS} is the optical efficiency of the system, A_R is the area of the receiver, and $\Delta\lambda$ is the wavelength band of the optical bandpass filter to be placed directly in front of the detector, which will be centered around the wavelength of interest. Such a filter will eliminate wavelengths other than the laser wavelength of interest, thus decreasing the background noise.

3.1.5 Amplifier Noise

Amplifier noise is the noise added to the signal through the process of amplification. The noise added to a system by an amplifier is either defined as a noise equivalent temperature or a noise power spectral density. When the noise is specified as a equivalent noise temperature the noise current added by the amplifier can be calculated by using Eq. (3.1.3) which is the equation for Johnson noise. The equivalent noise temperature is used as the temperature instead of room temperature which is used in most

cases. When the noise power spectral density is given it is usually given in units of $\text{nV}/\sqrt{\text{Hz}}$. To find the noise current added by the amplifier the noise spectral density is squared, multiplied by the bandwidth and then divided by the square of the input impedance. These calculations are shown in Chapter 5 for specific specified values given by the manufacturer.

3.2 Probability Distributions of Noise

The fluctuations of current in the detection circuit are caused by the detection process and other noise sources as described earlier. These fluctuations, being random, can be expressed using probability density functions (PDF's). Both coherent and incoherent detection techniques have PDF's representing the probability distribution of the primary noise source. Using these distributions, equations for the probability of false alarm can be found.

3.2.1 Probability Distribution of Noise for Incoherent Detection

For incoherent detection the dominating noise source, as will be shown later in section 5.1.5.2, is return signal shot noise. The shot noise current fluctuation around a DC average current is a Poisson PDF but at these high event densities it is approximated as a Gaussian PDF with a zero mean expressed as [1,12]

$$Pin(i) = \frac{1}{\sqrt{2\pi\langle i_{Incoh,SN}^2 \rangle}} \exp\left[-\frac{i^2}{2\langle i_{Incoh,SN}^2 \rangle}\right], \quad (3.2.1)$$

where i is the instantaneous detector output current and $\langle i_{Incoh,SN}^2 \rangle$ is the mean squared dominating noise current, which for this case is signal shot noise.

3.2.2 Probability Distribution of Noise for Coherent Detection

For the heterodyne or coherent detection case, the desired dominating noise is local oscillator (LO) shot noise. Shot noise can be represented by a Gaussian PDF before it is peak envelope detected, which is the common method of analysis used when doing coherent detection [12]. Once peak envelope detected, Rice [14] has shown that the noise current envelope follows a Rayleigh PDF $P_{co}(i)$ given by [12]

$$P_{co}(i) = \frac{i}{\langle i_{coh,SN}^2 \rangle} \exp\left[-\frac{i^2}{2\langle i_{coh,SN}^2 \rangle}\right], \quad (3.2.2)$$

where the dominating mean squared noise current for coherent detection is LO shot noise, $\langle i_{coh,SN}^2 \rangle$, as will be discussed later.

3.3 PDF's Representing the Combination of Signal and Noise

Not unlike the noise in the detection process, the return energy also fluctuates and the combination of that fluctuation and the fluctuation of the noise in the system can be represented by appropriate probability density functions (PDF's). These distributions will be different depending on the detection scheme used, the type of target, and the amount of atmospheric turbulence. The targets of interest are glint and speckle targets.

This section includes a description of the different PDF's for each of the detection schemes for each type of target. Once the PDF's for each case are established, the probability of detection can be calculated and these detection techniques can be compared.

3.3.1 The PDF's for Incoherent Detection

For incoherent (or energy) detection there are different PDF's for the sum of the noise and the signal currents, for both glint and speckle targets. A discussion of the PDF's for both targets follows.

3.3.1.1 Glint Target returns, or specular reflections, have return energies that can be calculated because the characteristics of the particular target are known. The process of detecting the return energy causes fluctuations in the output current. This fluctuation can be described by a Poisson probability distribution given as [12]

$$P(k) = \frac{\langle k \rangle^k \cdot e^{-\langle k \rangle}}{k!}, \quad (3.3.1)$$

where k is the number of photoelectrons emitted by the detector and $\langle k \rangle$ is the average number of photoelectrons emitted by the detector. An example of a Poisson distribution is shown in Fig. 2 for only a few incident photons. In our situation however, there is a much larger number of photons striking the detector producing a larger current. The central limit theorem states that as the number of statistically independent events occur without limit, the Poisson probability distribution will tend toward a Gaussian distribution [2,12,15] given generally as

$$p(k) = \frac{1}{\sqrt{2\pi\sigma^2}} \exp\left[-\frac{(k-m)^2}{2\sigma^2}\right], \quad (3.3.2)$$

which has a mean, m , equal to the variance, σ^2 , (see Appendix A)

$$\sigma^2 = m. \quad (3.3.3)$$

This can also be shown graphically as in Fig 3.

Since the target of interest for this case is a glint target, the return will be very large and the Poisson distribution can be approximated by a Gaussian distribution. The

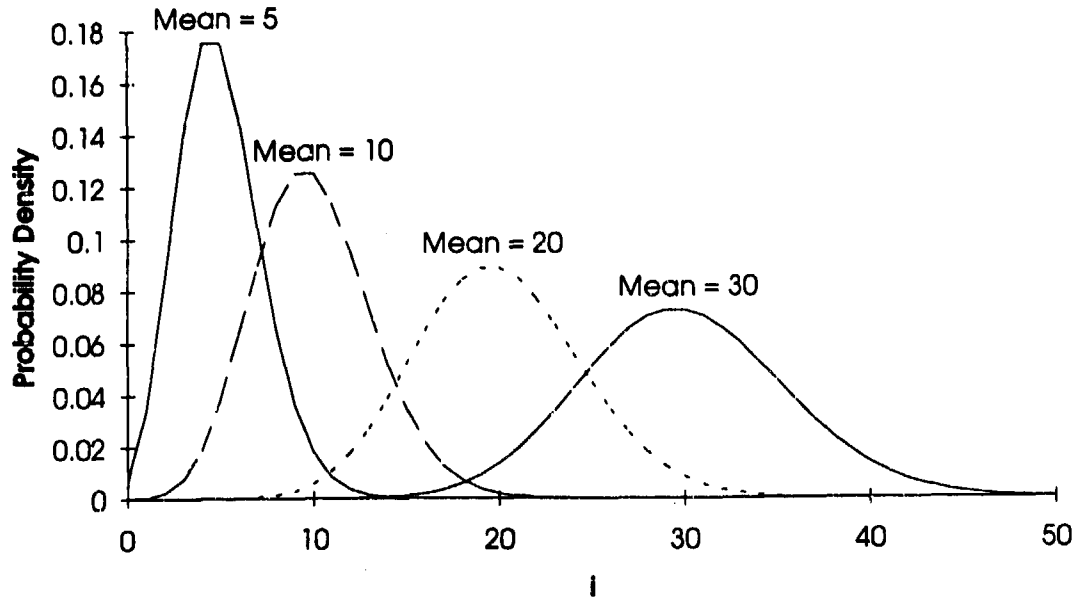


Figure 2: Poisson distributions with different mean values.

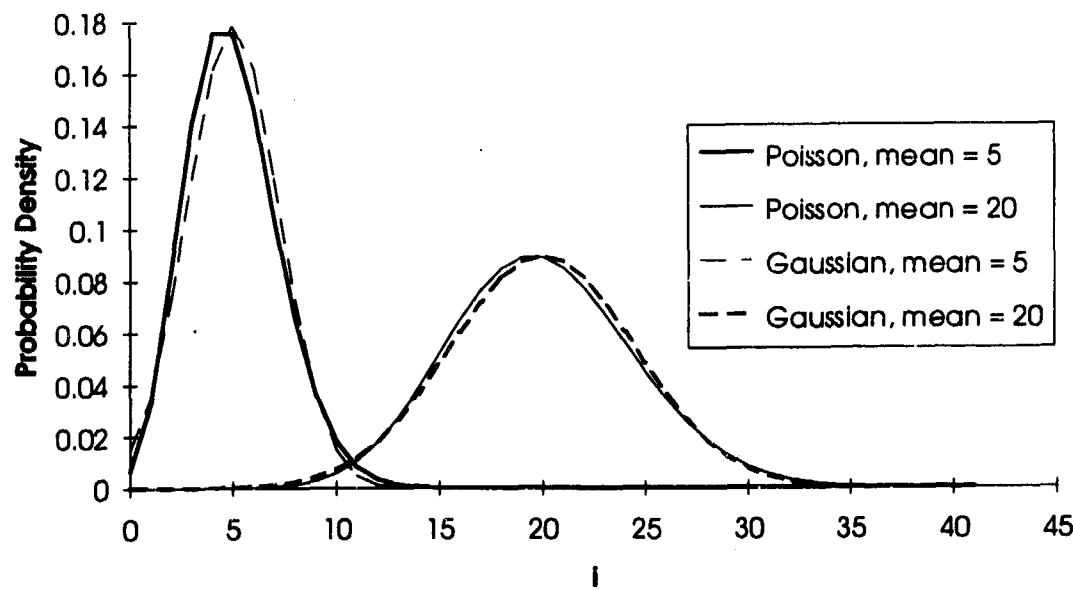


Figure 3: Comparison between Poisson and a Gaussian distribution.

dominant noise for the incoherent detection case (signal shot noise) also has a Gaussian distribution with zero mean as stated earlier. So the combined distribution of the two independent Gaussian variables is a Gaussian distribution where the mean is equal to the sum of the signal and noise current means and the variance is equal to the sum of the independent signal and noise current variances [16]. The PDF representing the fluctuation in the current i for incoherent detection with a glint target p_{IG} is [12]

$$p_{IG}(i) = \frac{1}{\sqrt{2\pi(\langle i_{Incoh,SN}^2 \rangle + 2qB\langle i_{Glint} \rangle)}} \exp\left[-\frac{(i - \langle i_{Glint} \rangle)^2}{2(\langle i_{Incoh,SN}^2 \rangle + 2qB\langle i_{Glint} \rangle)}\right], \quad (3.3.4)$$

where $\langle i_{Glint} \rangle$ is the average current produced by the return energy from a glint target, q is the charge on an electron, B is the bandwidth of the detection electronics, and $2qB\langle i_{Glint} \rangle$ is the mean squared signal current. (Further explanation is found in Appendix A.)

3.3.1.2 Speckle or Diffuse Targets have return energies that are random due to the surface irregularities in the targets. The detection statistics for this case are conditionally Poisson conditioned on knowing the amount of return energy. Since the return energy is random, the unconditional PDF that represents k signal photoelectrons emitted is a negative binomial distribution given by Goodman as [15]

$$p_{IS}(k) = \int_0^\infty P_{S+N}(k|W)p(W)dW \quad (3.3.5)$$

where k , the number of photoelectrons can be converted to current by multiplying by $q/\Delta t$ where q is the charge on an electron and Δt is the transmitted pulse length which will be discussed later in Section 4.1.2, $p(W)$ is the probability density function of the return energy (W) incident on the detector during a pulse and is given by the Gamma density as,

$$p(W) = \begin{cases} \frac{a^M W^{M-1} \exp(-aW)}{\Gamma(M)} & ; W \geq 0 \\ 0 & ; \text{Otherwise} \end{cases} \quad (3.3.6)$$

where M is the number of spatial correlation cells received by the detector, $a = M/\langle W \rangle$, $\langle W \rangle$ is the average return energy and Γ is the gamma function. M can be thought of as a measure of the spatial granularity of the target as seen by the receiver. Furthermore, $P_{s+N}(k|W)$ is the conditional PDF of the total (signal and noise) photoelectron count emitted by the detector. The conditional PDF for the signal photoelectron count alone ($P_s(k|W)$) is a Poisson probability density function given as

$$P_s(k|W) = \frac{(\eta W/hv)^k}{k!} \exp\left(-\frac{\eta W}{hv}\right), \quad (3.3.7)$$

where η is the quantum efficiency of the detector, h is Plank's constant, v is the optical frequency and $\eta W/hv$ is the mean number of detected photoelectrons. Fortunately, in the presence of a large photoelectron count rate, a Poisson distribution can be approximated as a Gaussian distribution. Thus the probability that k photoelectrons are emitted by the detector is approximately

$$P_s(k|W) = \frac{1}{\sqrt{2\pi bW}} \exp\left(-\frac{(k - bW)^2}{2bW}\right), \quad (3.3.8)$$

where $b = \eta/hv$, which is just a constant chosen to simplify the equation.

The dominant noise for incoherent detection, which is signal shot noise, also has a Gaussian PDF. The sum of two Gaussian random variables (signal and noise) has a Gaussian PDF where the variance is equal to the sum of the variances of the random variables. So the PDF representing the number of electrons in the detector circuit is a Gaussian PDF of the form

$$P_{S+N}(k|W) = \frac{1}{\sqrt{2\pi(\langle n \rangle + bW)}} \exp\left[-\frac{(k - (\langle n \rangle + bW))^2}{2(\langle n \rangle + bW)}\right]. \quad (3.3.9)$$

where $\langle n \rangle$ is the mean number (and the variance) of noise photoelectrons. Now using Eqs. (3.3.5), (3.3.6), and (3.3.9) the distribution of the return signal and noise is given by

$$\begin{aligned} p_{IS}(k) &= \int_0^\infty P_{S+N}(k|W)p(W)dW \\ &= \int_0^\infty \frac{1}{\sqrt{2\pi(\langle n \rangle + bW)}} \exp\left[-\frac{(k - (\langle n \rangle + bW))^2}{2(\langle n \rangle + bW)}\right] \frac{a^M W^{M-1} \exp(-aW)}{\Gamma(M)} dW. \end{aligned} \quad (3.3.10)$$

An example of this distribution is plotted in Fig. 5 using 1 as the average noise ($\langle n \rangle$), 2 as the mean return signal ($\langle W \rangle$), and 4 for the number of speckle lobes (M).

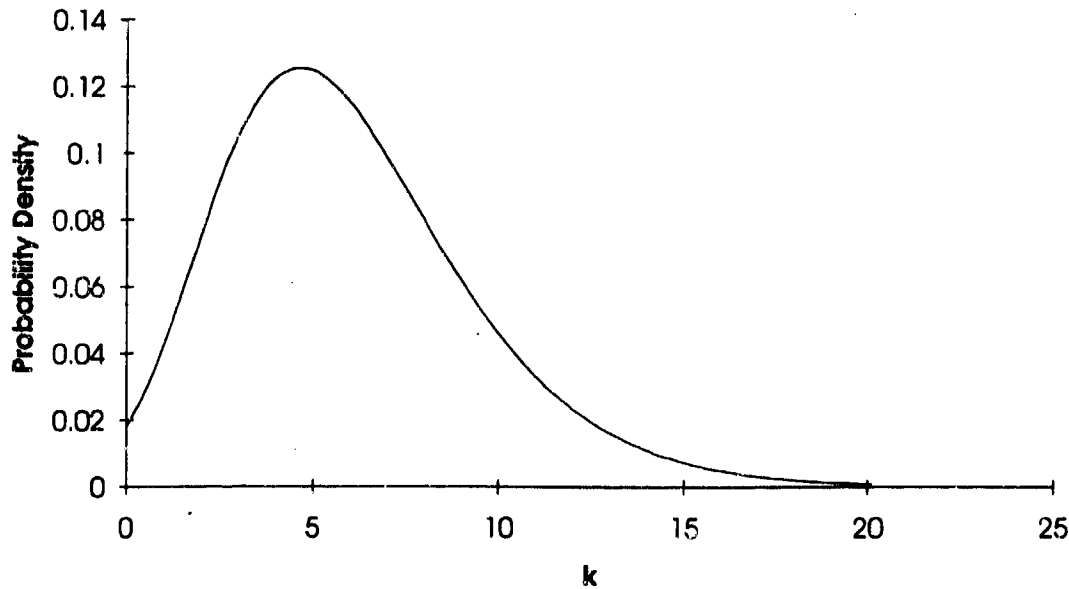


Figure 4: This is an example of the distribution of the return energy and the noise for incoherent detection with a speckle target.

3.3.2 Probability Distribution for Coherent Detection

For coherent (or heterodyne) detection the same probability density function can be used to represent the signal current due to either a glint or a speckle target, or even a target containing both glint and speckle components. This density is called the Rician PDF and has the form [2]

$$p(i) = \frac{2i}{\sigma^2} \exp\left[-\frac{i^2 + i_{Glint}^2}{\sigma^2}\right] I_0\left(\frac{2ii_{Glint}}{\sigma^2}\right) \quad (3.3.11)$$

where i represent the total instantaneous peak envelope detected signal, σ^2 is the mean squared strength of the speckle plus shot noise component expressed as $\sigma^2 = (\langle i_{Coh,SN}^2 \rangle + \langle i_{Diffuse}^2 \rangle)$, $\langle i_{Diffuse}^2 \rangle$ represents the mean squared signal current from a diffuse target, $\langle i_{Coh,SN}^2 \rangle$ is the mean squared noise current (shot noise) for coherent detection, I_0 is the zeroth order modified Bessel function of the first kind, and i_{Glint} is the portion of the total signal arising from a glint target component. An example of this combined distribution is shown in Fig. 5 where $\langle i_{Coh,SN}^2 \rangle$ was set to 5 and $\langle i_{Diffuse}^2 \rangle$ was set

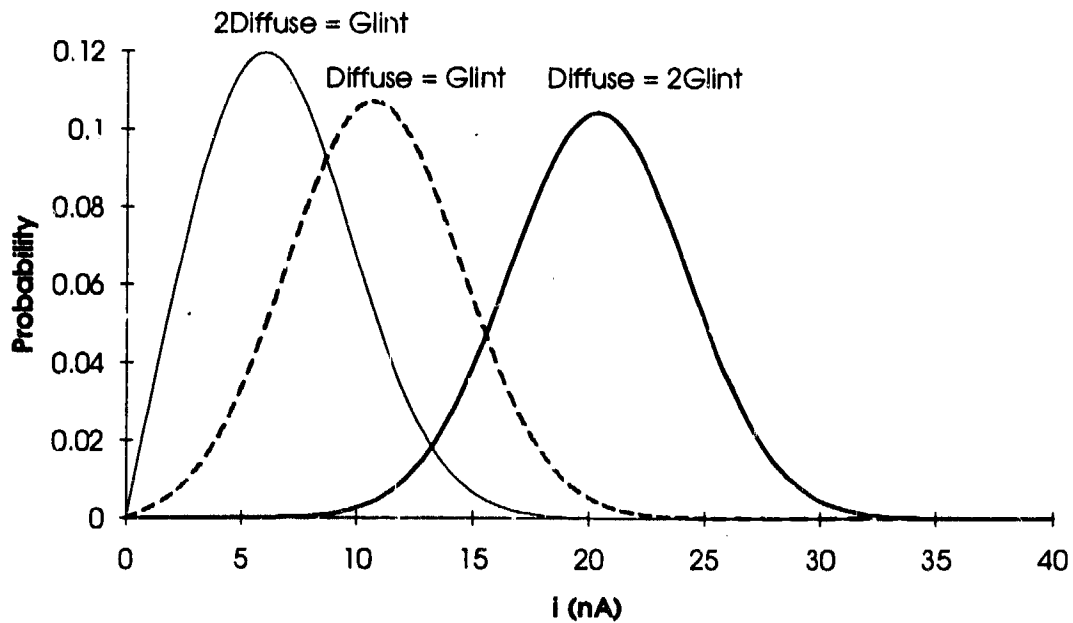


Figure 5: A Rician distribution with different components of diffuse and glint targets.

to 10, while i_{Glint} was varied to give different glint to noise ratios. The discussion of the probability distributions for each target individually follows.

3.3.2.1 A Speckle/Diffuse Target is by definition optically rough and scatters incident light randomly. The light scattered from each individual scattering centers interfere with each other to produce a speckle pattern, which when viewed, resembles random light and dark patches. The randomness in the speckle pattern and the randomness associated with the random phase of these speckles produces a random fluctuation in the current produced by the detector which can be represented by a Gaussian distribution [2] prior to envelope detection. Since both the signal and the noise currents are represented by Gaussian PDF's, their combination can be represented by a Gaussian PDF where the mean squared value is equal to the sum of the mean squared values of the signal and noise currents. With coherent detection, the detected Gaussian distributed signal will be passed through a bandpass filter centered around the intermediate frequency. As previously mentioned (see Section 3.2.2), the envelope detected output of the bandpass filter has been shown by Rice [14] to have a Rayleigh PDF. Therefore, the PDF for coherent detection with a speckle target, p_{CS} , is given as [10]

$$p_{CS}(i) = \frac{2i}{\langle i_{Coh,SN}^2 \rangle + \langle i_{Diffuse}^2 \rangle} \exp\left(-\frac{i^2}{\langle i_{Coh,SN}^2 \rangle + \langle i_{Diffuse}^2 \rangle}\right) \quad (3.3.12)$$

where i represent the instantaneous peak envelope detected signal.. This same distribution could be found by substituting zero in for i_{Glint} in Eq. (3.3.11). An example of the Rayleigh PDF is shown in Fig. 6 where the mean squared values used are shown.

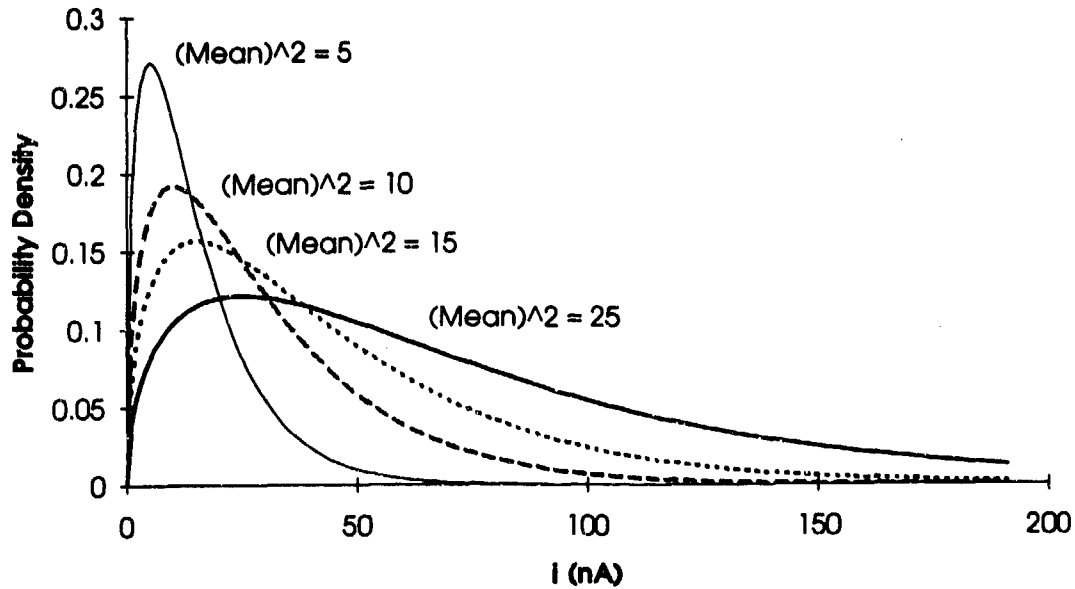


Figure 6: This shows a Rayleigh probability density with an increasing diffuse component.

3.3.2.2 *A Glint/Specular Target* produces a deterministic (non-statistically varying) return [2]. The combination of this return signal and the Gaussian noise gives a complex Gaussian distribution for the overall detected current. The return is complex because there are both in-phase and out-of-phase components due to differences in range to the target. The PDF representing the envelope of the current fluctuations (signal and noise) at the output of the bandpass filter for coherent detection with a glint target, p_{CG} , is given by [1,2,12,14]

$$p_{CG}(i) = \frac{2i}{\langle i_{Coh,SN}^2 \rangle} \cdot \exp\left[-\frac{i_{Glint}^2 + i^2}{\langle i_{Coh,SN}^2 \rangle}\right] I_0\left(\frac{2i_{Glint}i}{\langle i_{Coh,SN}^2 \rangle}\right). \quad (3.3.13)$$

This is known as the Rician PDF. This same distribution can be obtained by substitution in zero for $\langle i_{Diffuse}^2 \rangle$ in Eq. (3.3.11) since this discussion is for an entirely glint target. An example of different Rician distributions with no diffuse component, a mean glint component of 10 nA, and an increasing noise component are shown in Fig. 7.

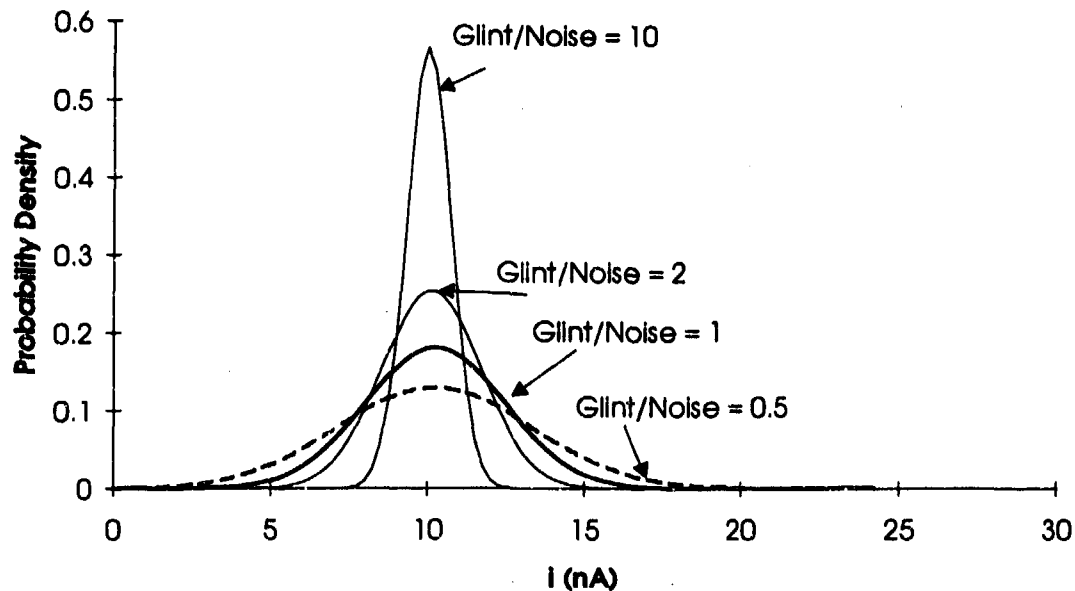


Figure 7: A Rician distribution for a totally glint target (no diffuse component).

3.4 The Probabilities of False Alarm

A false alarm occurs when a return signal has been declared a target when in actuality there is no target present. For a given threshold level, the probability of false alarm is the probability that the noise level will exceed that threshold level. Mathematically, it is defined as the area under the noise PDF which exceeds the set threshold level, i_T . To find the probability of false alarm, the area under the noise probability density curve is calculated from the threshold level to infinity (see Figure 1). As seen in the previous sections, the dominating noise for each detection technique is different, therefore there are two different probability density functions representing the noise. The following two sections discuss the probability of false alarm for incoherent and coherent detection.

3.4.1 The Probability of False Alarm for Incoherent detection

As stated above the probability of false alarm is the area under the probability density function of the noise, greater than a set threshold level. For incoherent detection the probability distribution for the signal shot noise current fluctuation is a Gaussian PDF given in Eq. (3.2.1) as [2,12]

$$Pin(i) = \frac{1}{\sqrt{2\pi\langle i_{Incoh,SN}^2 \rangle}} \exp\left(-\frac{i^2}{2\langle i_{Incoh,SN}^2 \rangle}\right). \quad (3.4.1)$$

where i is the instantaneous detector output current and $\langle i_{Incoh,SN}^2 \rangle$ is the mean squared noise current for incoherent detection. The probability of false alarm can then be expressed as

$$\begin{aligned} Pin_{FA} &= \int_{i_T}^{\infty} Pin(i) di \\ &= \frac{1}{\sqrt{2\pi\langle i_{Incoh,SN}^2 \rangle}} \int_{i_T}^{\infty} \exp\left(-\frac{i^2}{2\langle i_{Incoh,SN}^2 \rangle}\right) di, \end{aligned} \quad (3.4.2)$$

where i_T is the threshold current level. Equation (3.4.2) can be simplified for easier use by substituting in the complementary error function, $ERFC(x)$, where

$$ERFC(x) = \frac{2}{\sqrt{\pi}} \int_x^{\infty} e^{-t^2} dt. \quad (3.4.3)$$

Substituting Eq.(3.4.3) into Eq. (3.4.2) results in

$$Pin_{FA} = 0.5ERFC\left(\frac{i_T}{\sqrt{2\langle i_{Incoh,SN}^2 \rangle}}\right). \quad (3.4.4)$$

3.4.2 The Probability of False Alarm for Coherent Detection

The noise probability density function for coherent detection was given in Eq. (3.2.2) as [12]

$$P_{co}(i) = \frac{i}{\langle i_{Coh,SN}^2 \rangle} \exp\left(-\frac{i^2}{2\langle i_{Coh,SN}^2 \rangle}\right). \quad (3.4.5)$$

The probability of false alarm is therefore

$$\begin{aligned} P_{CO_{FA}} &= \int_{i_T}^{\infty} P_{co}(i) di \\ &= \int_{i_T}^{\infty} \frac{i}{\langle i_{Coh,SN}^2 \rangle} \exp\left(-\frac{i^2}{2\langle i_{Coh,SN}^2 \rangle}\right) di \\ P_{CO_{FA}} &= \exp\left(-\frac{i_T^2}{2\langle i_{Coh,SN}^2 \rangle}\right). \end{aligned} \quad (3.4.6)$$

A desired probability of false alarm can be obtained by knowing the mean squared noise current and by then manipulating the threshold current i_T . Once the desired probability of false alarm is achieved the threshold current used to achieve that probability of false alarm can be used to determine the probability of detection.

3.5 The Probability of Detection

The probability of detection is the probability that a received signal is correctly declared a return from a target. Mathematically speaking, the probability of detection is the area under the probability density function representing the signal and noise greater than the decision threshold (see Figure 1). Since there are two detection techniques of interest and two targets of interest the following discussion is broken down into four

sections. Each section presents the probability of detection for a specific detection scheme for an individual type of target.

3.5.1 The Probability of Incoherent Detection

The probability of detection for incoherent detection will be discussed in this section. To find the probability of detection the probability density function for each type of target will be integrated from a threshold level, determined by calculating the probability of false alarm, to infinity.

3.5.1.1 The Probability of Incoherent Detection with a Glint Target is the integral of the probability density function for combined signal and noise. This probability density function was given in Eq. (3.3.4) as [12]

$$p_{IG}(i) = \frac{1}{\sqrt{2\pi(\langle i_{Incoh,SN}^2 \rangle + 2qB\langle i_{Glint} \rangle)}} \exp\left[-\frac{(i - \langle i_{Glint} \rangle)^2}{2(\langle i_{Incoh,SN}^2 \rangle + 2qB\langle i_{Glint} \rangle)}\right]. \quad (3.5.1)$$

The probability of detection, Pd_{IG} , is then calculated as

$$Pd_{IG} = \frac{1}{\sqrt{2\pi(\langle i_{Incoh,SN}^2 \rangle + 2qB\langle i_{Glint} \rangle)}} \int_{i_T}^{\infty} \exp\left[-\frac{(i - \langle i_{Glint} \rangle)^2}{2(\langle i_{Incoh,SN}^2 \rangle + 2qB\langle i_{Glint} \rangle)}\right] di. \quad (3.5.2)$$

This can be simplified by expressing the equation in terms of the complementary error function (ERFC), when $(i_T - \langle i_{Glint} \rangle \geq 0)$ and the error function (ERF) when $(i_T - \langle i_{Glint} \rangle < 0)$. We thus find

$$Pd_{IG} = \begin{cases} 0.5ERFC\left(\frac{(i_T - \langle i_{GInt} \rangle)^2}{(2(\langle i_{Incoh,SN}^2 \rangle + 2qB\langle i_{GInt} \rangle))^{\frac{1}{2}}}\right) & \text{where } i_T - \langle i_{GInt} \rangle \geq 0 \\ 0.5 \left[1 + ERF\left(\frac{(\langle i_{GInt} \rangle - i_T)^2}{(2(\langle i_{Incoh,SN}^2 \rangle + 2qB\langle i_{GInt} \rangle))^{\frac{1}{2}}}\right) \right] & \text{where } i_T - \langle i_{GInt} \rangle < 0 \end{cases} \quad (3.5.3)$$

where the error function is represented as

$$ERF(z) = \frac{2}{\sqrt{\pi}} \int_0^z e^{-t^2} dt, \quad (3.5.4)$$

and i_T is the threshold current discussed earlier. Once i_T is determined using the probability of false alarm the probability of detection can be determined.

3.5.1.2 The Probability of Incoherent Detection for a Speckle Target is the integral from a threshold to infinity over the probability density function given in Eq. (3.3.10) which is

$$p_{IS}(k) = \int_0^\infty \frac{1}{\sqrt{2\pi(\langle n \rangle + bW)}} \exp\left[-\frac{(k - (\langle n \rangle + bW))^2}{2(\langle n \rangle + bW)}\right] \frac{a^M W^{M-1} \exp(-aW)}{\Gamma(M)} dW \quad (3.5.5)$$

So the probability of detection is

$$Pd_{IS} = \int_{x_T}^\infty \int_0^\infty \frac{1}{\sqrt{2\pi(\langle n \rangle + bW)}} \exp\left[-\frac{(k - (\langle n \rangle + bW))^2}{2(\langle n \rangle + bW)}\right] \frac{a^M W^{M-1} \exp(-aW)}{\Gamma(M)} dW dk, \quad (3.5.6)$$

where x_T is the threshold current expressed in terms of photoelectrons (Photoelectrons can be converted to current by multiplying by $q/\Delta t$ where q is the charge on an electron and Δt is the transmitted pulse length which will be discussed later in Section 4.1.2.) This is somewhat of an intimidating expression. To simplify this expression the outer integral can be reduced using the ERFC(z) function given in Eq. (3.5.4). The result is

$$Pd_{IS} = \frac{1}{2} \int_0^{\infty} ERF C \left(\frac{x_T - (\langle n \rangle + bW)}{\sqrt{2(\langle n \rangle + bW)}} \right) \frac{a^M W^{M-1} \exp(-aW)}{\Gamma(M)} dW. \quad (3.5.7)$$

3.5.2 The Probability of Coherent Detection

In the following section the probability of detection will be discussed for coherent detection with a glint and a speckle target.

3.5.2.1 The Probability of Coherent Detection with a Glint Target is calculated using the Rician PDF given in Eq. (3.3.13) as

$$p_{CG}(i) = \frac{2i}{\langle i_{Coh,SN}^2 \rangle} \exp \left[-\frac{i_{Glint}^2 + i^2}{\langle i_{Coh,SN}^2 \rangle} \right] I_0 \left(\frac{2i_{Glint}i}{\langle i_{Coh,SN}^2 \rangle} \right) \quad (3.5.8)$$

The probability of detection for coherent detection with a glint target, Pd_{CG} , is then given by

$$Pd_{CG} = \int_{i_T}^{\infty} \frac{2i}{\langle i_{Coh,SN}^2 \rangle} \exp \left[-\frac{i_{Glint}^2 + i^2}{\langle i_{Coh,SN}^2 \rangle} \right] I_0 \left(\frac{2i_{Glint}i}{\langle i_{Coh,SN}^2 \rangle} \right) di. \quad (3.5.9)$$

where due to the Bessel function in the equation there is no clear way to simplify this equation further.

3.5.2.2 The Probability of Coherent Detection with a Speckle Target is the integral from a threshold current to infinity over a Rayleigh probability distribution given in Eq. (3.3.12). The probability of detection for this case is

$$\begin{aligned}
 Pd_{CS} &= \int_{i_r}^{\infty} p_{CS}(i) di \\
 &= \int_{i_r}^{\infty} \frac{2i}{\langle i_{Coh,SN}^2 \rangle + \langle i_{Diffuse}^2 \rangle} \exp\left[-\frac{i^2}{\langle i_{Coh,SN}^2 \rangle + \langle i_{Diffuse}^2 \rangle}\right] di,
 \end{aligned} \tag{3.5.10}$$

which can be easily integrated and reduced to

$$Pd_{CS} = \exp\left[-\frac{i_r^2}{\langle i_{Coh,SN}^2 \rangle + \langle i_{Diffuse}^2 \rangle}\right]. \tag{3.5.11}$$

Now that the equations for the probability of detection are known the characteristics of the experimental setup need to be known in order to do a numerical analysis to determine the probability of detection for each case for both detection schemes.

CHAPTER IV

4.0 SYSTEM CONFIGURATION

This chapter consists of a detailed description of the components of the LADAR system used to compare coherent to incoherent detection. This discussion consists of a component by component description of the system and how each component aids in the operation of the system and a discussion on the optimization of the both detection schemes.

4.1 System Layout

4.1.1 Master Oscillator

A top view of the laser radar system is shown in Figure 8. The master oscillator (MO) in the system is a diode pumped, CW, room temperature, Thulium (Tm), Holmium (Ho):YAG laser. This laser was developed for this project by CLR Photonics Inc. This laser has a maximum output of 80 mW. The output of the MO is used for injection seeding the slave oscillator and it is also used as the local oscillator (LO) signal when the ladar system is used in the coherent mode of detection. The first mirror and most of the

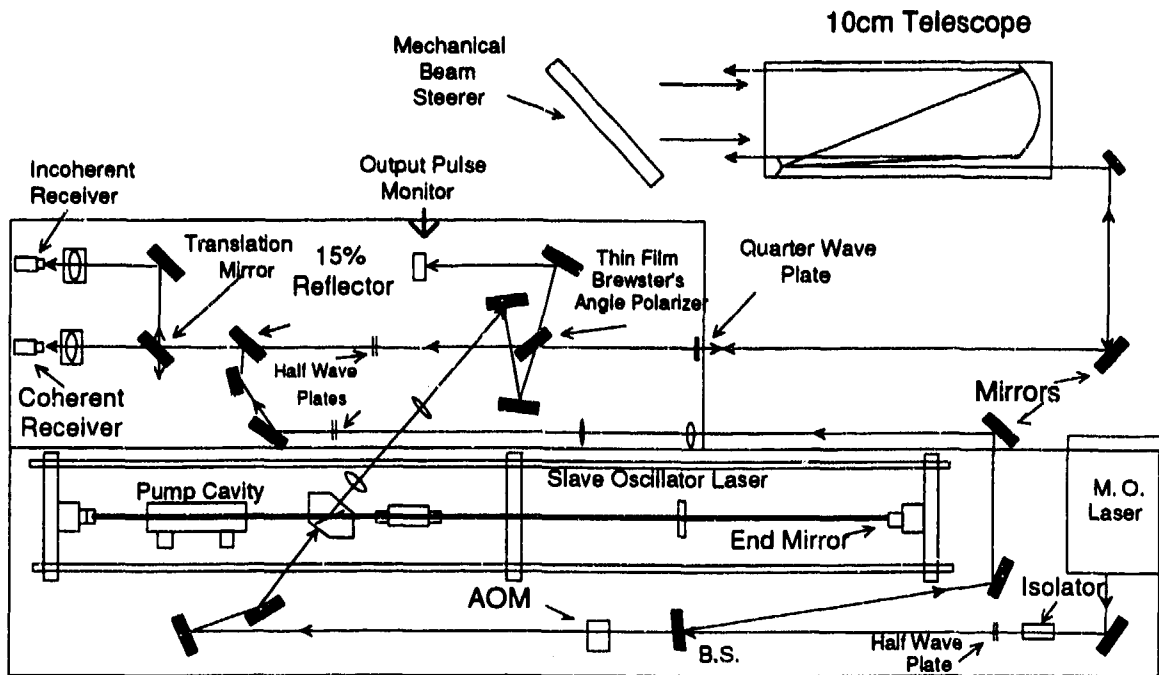


Figure 8: Layout of LADAR system.

turning mirrors in the system are coated to be 99.9% reflective at 45° . The next element in the system is a Faraday optical isolator, which was acquired from Optics for Research, Model #IO-4-HoYAG. This element consists of an input polarizer, a rotator material and an analyzer. The input polarizer insures that the incoming light is linearly polarized horizontally. The rotator material then rotates the polarization of the light by 45° and the beam exits through the analyzer, which is positioned at 45° . Any back-reflections from other components in the system enter through the analyzer and the polarization is rotated by the rotater material and the polarization will be perpendicular to the final polarizer. This gives an extinction of approximately 40dB. The optical transmission efficiency of this device is 50%.

The next element in the system is a half-wave plate which is used to control the polarization of the light that enters the slave oscillator (SO). The following element in the system is a 98% beam splitter. The reflected 98% is used as the LO when the system is

being used in the coherent detection scheme. This beam is reflected around the end of the SO and reflected so the beam is traveling parallel behind the cavity. The beam then encounters a 60mm and 120mm lens pair that expands the beam from 2mm to 4mm. The combination of the next two elements in the system, the half wave plate and the thin film Brewster's angle polarizer, allow control of the amount of light incident on the detector which is used as the LO. The thin film Brewster's angle polarizer was obtained from Rocky Mountain Instruments. The Brewster's angle for $2.09\mu\text{m}$ for this element is 57° . The light that reflects off the thin film Brewster's angle polarizer is then reflected into the detection optics by a 15% beam splitter. The detection optics will be discussed later.

The transmitted 2% from the 98% beam splitter is frequency shifted 27.1 MHz, into the first order, by an acoustic optic modulator (AOM). This AOM was purchased from Newport Electro-Optical Systems, Model #N31027-4D. The diffraction efficiency of this AOM for $2.09\mu\text{m}$ is about 60%. The beam that is frequency shifted into the first order is then reflected into the SO for injection seeding.

4.1.2 Slave Oscillator

The slave oscillator is a Chromium (Cr), Tm, Ho:YAG, flashlamp pumped, Q-switched laser. The end mirrors are greater than 99.5% reflective at 0° incidence, planar, AR coated at $2.09\mu\text{m}$ and have a damage threshold of 100MW/cm^2 . The output coupling is controlled by the combination of a quarter-wave plate, the end mirror and a thin film Brewster's angle polarizer.

The polarization of the light in the cavity is horizontal until it transmits through the quarter wave plate as seen in Fig. 9. Once the light translates through the quarter-wave plate the polarization of the light is generally elliptical. The rotation of this elliptically polarized light reverses direction after the light strikes the end mirror. Once the light passes through the quarter-wave plate, on its return trip, the light will again be linearly

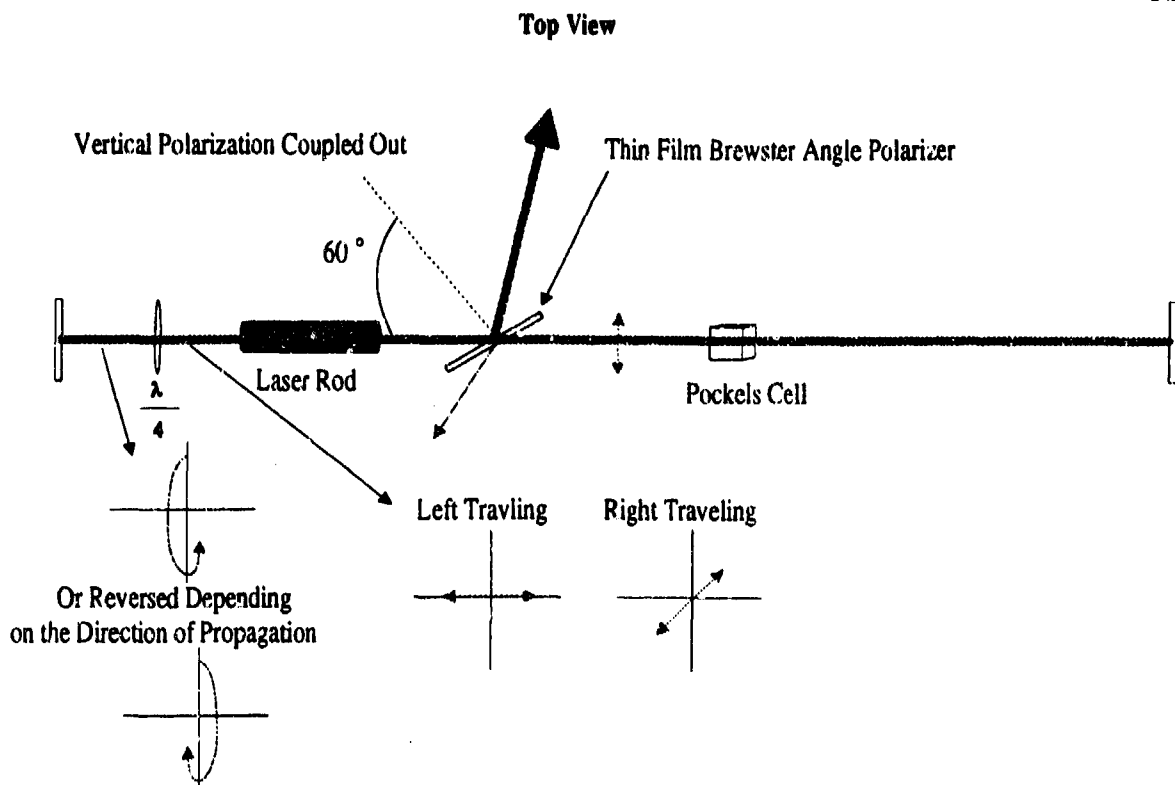


Figure 9: Description of output coupling from slave oscillator.

polarized but, there will be both a horizontal and a vertical component. The vertical component of the polarization is reflected out of the cavity when it strikes the thin film Brewster's angle polarizer. The amount of vertically polarized light depends on the position of the fast axis of the quarter-wave plate. The quarter-wave plate is set so the output coupling of the cavity is 20%. When the output coupling is set lower the intensity of the light in the cavity is such that optical elements can be and have been damaged.

The Kigre Inc. FOM-455C laser pump cavity is dual-lamp with a diffusely-reflecting elliptical cavity. The diffusely-reflecting cavity is less efficient than a reflector cavity, but the pumping is more uniform, giving a more uniform output beam and better quality thermal lensing characteristics. Thermal lensing occurs in the laser rod because of heating from the flashlamps and the cooling from the water. The rod is water cooled but the rate at which the rod is pumped determines how cool the rod is kept. As the repetition

rate increases, the rod begins to cool unevenly causing a temperature gradient between the outside and inside of the rod, where the inside of the rod is at a higher temperature than the outside. This temperature gradient causes a radial change in the index of refraction. This change in the index causes the rod to act like a lens, hence the name of thermal lensing. When thermal lensing occurs the mode volume decreases, decreasing the output power of the laser. If the pump rate is fast enough the rod does not have enough time to cool to give as great a temperature differential and it will only decrease the mode volume slightly [17]. Since the mirrors in this cavity are planar the cavity is critically stable, but with thermal lensing occurring, the stability of the cavity increases due to the focusing power of the rod.

The pump chamber is a barium-sulfate-packed KC331 glass filter/flow tube. The glass filter absorbs energy below 343 nm which are not needed to pump the crystal to population inversion. This glass also absorbs heat preventing unnecessary heating of the rod. The flow tube allows the Kigre Xenon flashlamps and the rod to be cooled with deionized water to 20°C. The cooling of the flashlamps and the laser rod is controlled by a Neslabs HX recirculating chiller.

The YAG laser rod is 55 mm long and 4mm in diameter. The dopant concentrations are 0.86% Chromium (Cr), 5.83% Thulium (Tm), and 0.34% Holmium (Ho). The energy level diagram for Cr, Tm, Ho:YAG is shown in Fig. 10. The flashlamp energy is absorbed by the Cr^{3+} ion. Once the atoms settle in the $^4\text{T}_2$ and ^2E states they transfer to the $^3\text{F}_3$ and the $^3\text{H}_4$ in the Tm^{3+} ion. The excited Tm^{3+} atom then interacts with a ground state Tm^{3+} in a cross-relaxation process. This process produces two Tm^{3+} ions in the $^3\text{F}_4$ state. The energy is then transferred to the $^5\text{I}_7$ state where lasing occurs in the $^5\text{I}_7 - ^5\text{I}_8$ transition [6].

The slave oscillator is Q-switched using Fast Pulse's 3902W-2100 LiNbO₃ Pockels cell. The Q of a cavity is defined as the energy stored in a system at resonance divided by the energy lost in a cycle of oscillation. So the higher the Q the lower the losses. Q-

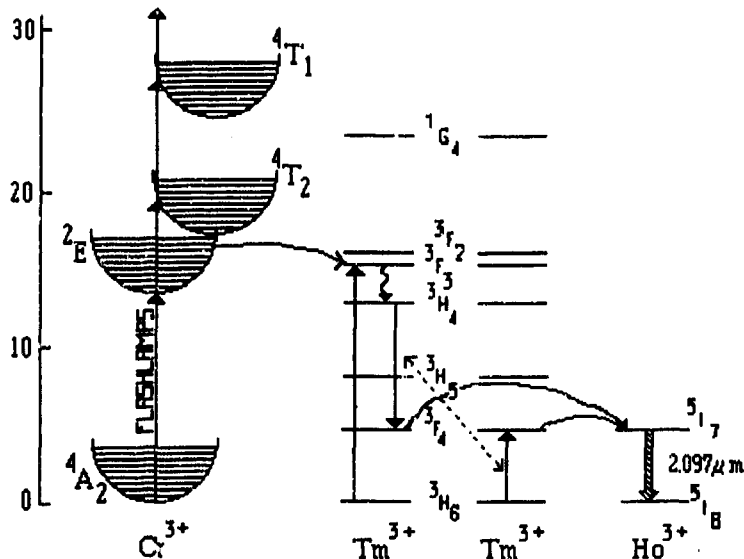


Figure 10: Energy level diagram for Cr,Tm,Ho:YAG, laser rod.

switching is the switching between a cavity of a low Q, which prevents lasing, to a cavity with a high Q, which allows the cavity to lase. The changing of the Q of the transmitter is controlled by the LiNbO₃ Pockels cell using the electro-optic effect. Enough voltage is applied to the Pockels cell to rotate the polarization inside the cavity so that the combination of the quarter-wave plate and the thin film polarizer reflects the light out of the cavity causing it not to lase. The voltage that would normally be applied to the Pockels cell to accomplish this task is the quarter-wave voltage. The quarter-wave voltage for this cell is 2.5 kV, but the cavity of this laser is very lossy so a voltage much lower is sufficient to perform the Q-switching. Experimentally this voltage has been found to be about 960 Volts. It was also found that this voltage is directly dependent on both the repetition rate and the pump energy. An example of an unQ-switched pulse is shown

in Fig. 11 and a Q-switched pulse is shown in Fig. 12. The two main differences of concern are the length of the pulse and the magnitude of the pulse. The unQ-switched pulse is about 2 ms in length whereas the Q-switched pulse is about 1 ms in length with a FWHM of 500ns. The vertical scales in both Figs. 11 and 12 are in volts, which was an observed output from the InGaAs detector. The output of the Q-switched pulse is nearly an order of magnitude greater.

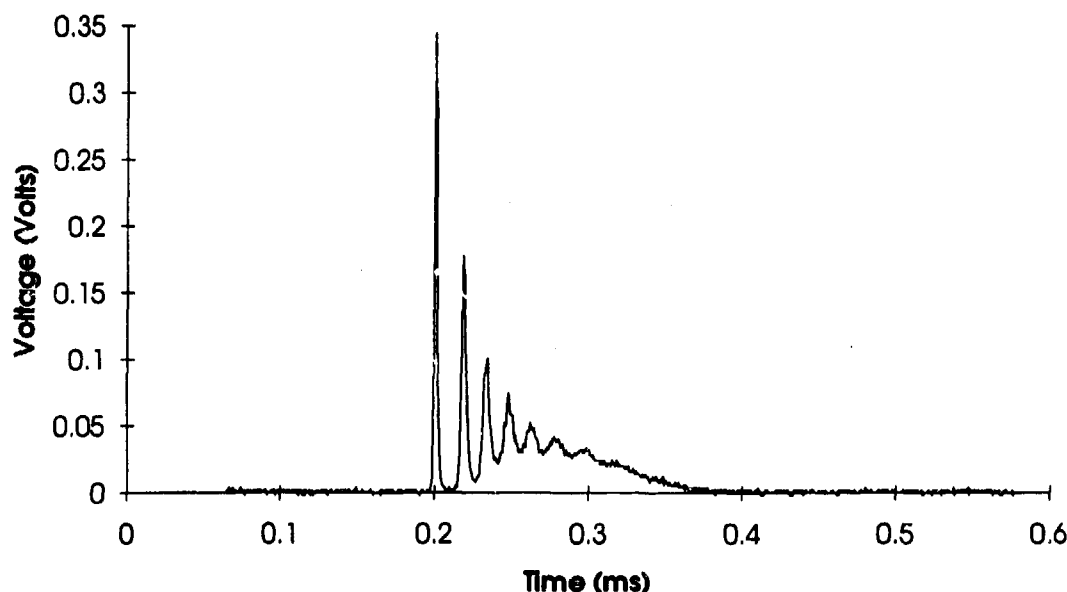


Figure 11: Slave oscillator long pulse output.

Another element in the SO cavity is a $75\mu\text{m}$ etalon. This etalon is used to tune the wavelength of the cavity. By changing the angle of the etalon in the cavity the wavelength can be changed.

In order to do coherent detection the wavelength of the SO is locked to that of the MO except for the 27.1 MHz frequency shift introduced by the AOM. In order to properly injection seed, the length of the SO cavity has to be such that the desired wavelength will oscillate in the cavity. To control this length, one end mirror is mounted

to a piezoelectric transducer allowing it to be dithered to the correct wavelength to lase. A servo-loop was created by CTI in Boulder Colorado to do this job. There is a InGaAs photo-conductor, purchased from Epitaxx, mounted in the end of the laser cavity. This

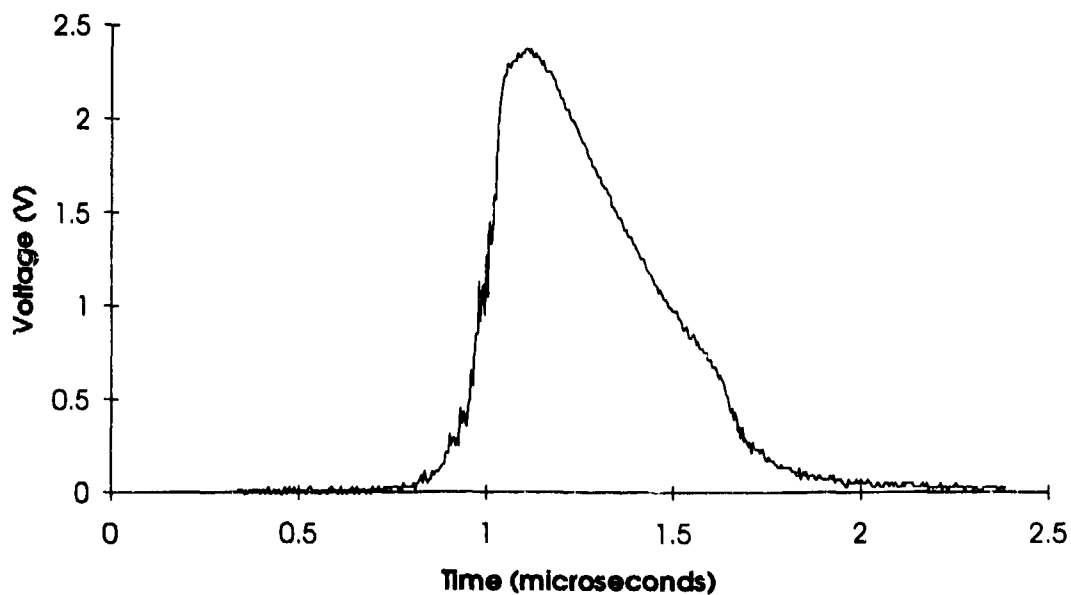


Figure 12: Slave oscillator output when Q-switched.

detector sends its signal to a servo box which monitors the build-up time of the laser pulse. When the laser is properly injection-seeded the laser pulse will occur earlier than normal. What this servo loop does is monitor the build-up time of the pulse and it dithers the cavity to decrease this build-up time. There is a threshold level that can be tuned on the servo system so an alarm will go off when the system is not injection-seeding.

Even though there is a servo-loop to aid in injection-seeding the SO and the MO have to be lasing at nearly the same wavelength and the MO has to be aligned so that it oscillates in the cavity along the same path that the SO lases. The etalon in the slave cavity allows the SO to be wavelength tuned as does the etalons in the MO. The

wavelength that the system is tuned to is $2.09046\mu\text{m}$. Both the MO and the SO have to be close to this wavelength or the system will not injection seed.

The SO laser requires 900V applied to the flashlamps, which results in about 96 J of applied energy. The repetition rate is 2.7 Hz with a long pulse output of 20 mJ. The shape of the long pulse is seen if Fig. 11. When the LiNbO₃ Q-switch is used the output reduces to approximately 17 mJ with a FWHM pulse length of 500 ns. An example of this pulse is seen in Fig. 12.

The output pulse from the transmitter that reflects out of the cavity, is first expanded 2× by a 50mm and a 100mm lens pair. The beam then reflects off of two mirrors that are used to walk the beam during alignment procedures. The beam then strikes another thin film Brewster's angle polarizer. Since this beam is vertically polarized, it reflects off of the polarizer. There is some leakage of the outgoing pulse through the polarizer. This portion is used to monitor the outgoing pulse to the target using a JD1000 Molelectron energy meter. The ratio of the light reflected to that which is transmitted through the polarizer has been measured as 15.3 to 1.

The thin film Brewster's angle polarizer and the quarter-wave plate make up the transmit receive switch for the laser radar system. The beam reflects off the polarizer transmits through the quarter wave plate, which produces circular polarization. The direction of the circular polarization is reversed when the beam strikes a target. So when the return beam travels through the quarter wave plate the light is changed from circular polarization to linear (horizontal) polarization. Being horizontally polarized the light transmits through the polarizer and the polarization is then rotated, using a half wave plate, to match that of the LO beam incident on the detector.

Before the beam is transmitted to the target it is expanded 20× by a Lambda/10's Laser Beam Expander Model LBX. This beam expander is an afocal, decentered, Dall-Kirkhan telescope. The primary mirror is a decentered section of a concave ellipsoid while

the secondary mirror is a convex sphere. The beam leaving the telescope is steered using a mechanical beam steerer. The beam steering device has a 6 inch flat mirror mounted on a two axis, computer controlled, Arotech gimble.

4.2 Detection Scheme

The theoretical analysis has been done assuming optimum detector performance for each detection scheme. For incoherent detection the optimum detector performance occurs with the best filling of the detector with the incoming light. For coherent detection the optimum detection of the light is dependent on the efficiency of the mixing between the local oscillator and the return pulse. Since this analysis has not taken into account turbulence the data taken needs to be taken together or one set directly after the other. This allows the data to be taken with nearly the same atmospheric conditions. To save time transitioning between detection schemes, a mirror on a translation stage has been placed in the return beam path. With the translation of the mirror into or out of the receiver path, the return energy can be sent to either detection scheme .

For incoherent detection the return light that transmits through the 15% beam splitter, a 38 nm optical bandpass filter from Optical Filter Corporation and is focused down onto an InGaAs detector. The return energy from the target is returning as a plane wave. Since it is a plane wave the focused return energy onto the detector is represented as an Airy disk [18]. The intensity pattern of the Airy disk is shown in Fig. 13, which is mathematically represented as

$$I = I_0 \left[\frac{2J_1(x)}{x} \right]^2, \quad (4.2.1)$$

where $J_1(x)$ is a first order Bessel function, and $x = k_w a q_R / R_i$, where a is the limiting optical aperture, q_R is the radius of the airy disk, k_w is the wave number and R_i is the distance from the aperture to the image. For this system it was decided that for incoherent detection both the central lobe and the first ring will be used. The first ring is zero at $x=7.016$. So using this and the equation for x the value for the focal length was found to be 53mm. The 50 mm focal lens was already being used to expand one of the beams in the system so a 40 mm focal length lens was substituted..

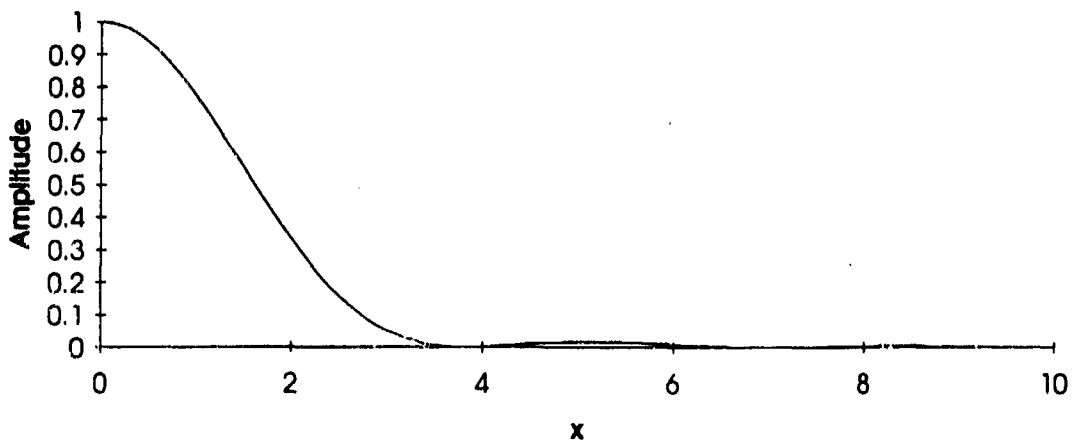


Figure 13: One side of Airy disk pattern.

For coherent detection the optimum detection of the light occurs when only the first lobe of the Airy disk pattern for the combination of the local oscillator and the return signal is incident on the detector. The first ring is 180° out of phase from the central lobe, so mixing the first ring with the central lobe would decrease the heterodyne efficiency.

The heterodyne efficiency is a ratio that expresses how efficient the return signal and the LO mix spatially. When the return signal and the LO are matched Airy functions at the plane of the detector, the heterodyne efficiency, γ , is given by [18,19]

$$\gamma = 1 - J_0^2(y) - J_1^2(y), \quad (4.2.2)$$

where $y = \pi r D_B / f \lambda$, f is the focal length of lens, D_B is the diameter of the laser beam, λ is the wavelength, r is the radius of the detector, and J_0 and J_1 are Bessel functions of the first kind. Equation 4.2.2 is plotted in Fig. 14.

For our system, the radius of the detector r is 50 μm , λ is 2.09 μm , and the diameter of the laser beam, D_B , is 4 mm. Notice now that the smaller the focal length lens

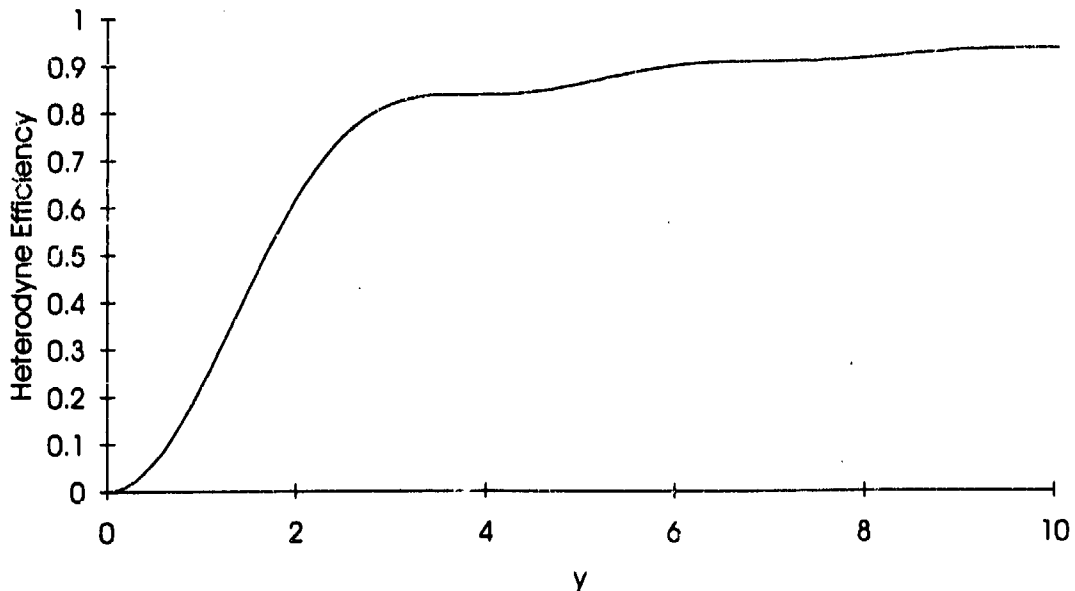


Figure 14: Theoretical heterodyne efficiency.

chosen, the better the heterodyne efficiency. For our work, a reasonable focal length lens of 80 mm was chosen, giving an y of 3.75 and a theoretical heterodyne efficiency of 0.84.

A schematic of the detection packages provided by Coherent Technologies, Inc. (CTI) of Boulder, CO is shown in Fig. 15 [20]. The photodetector is reversed biased, V_R , by a 3 Volt battery and is in series with a 1 $k\Omega$ resistor. The photodetector used is a p-i-n InGaAs photodiode which has a measured dark current of 135 nA and responsivity of 1.1 A/W at 2.09 μm . Since for coherent detection the detected signal will be at high frequencies, 27.1 MHz, and for direct detection the detected signal will be at low

frequencies, 2.7 Hz, the post detection electronics are different for each detection scheme. For incoherent detection the amplifier was purchased from Analog Modules and it has a bandwidth of 35 MHz and a midband gain of 60 dB [21]. There are no filters used for the incoherent detection scheme so the bandwidth is limited by the amplifier. The optimum load resistance, R_L , found by CTI for incoherent detection is $16 \text{ M}\Omega$ [20].

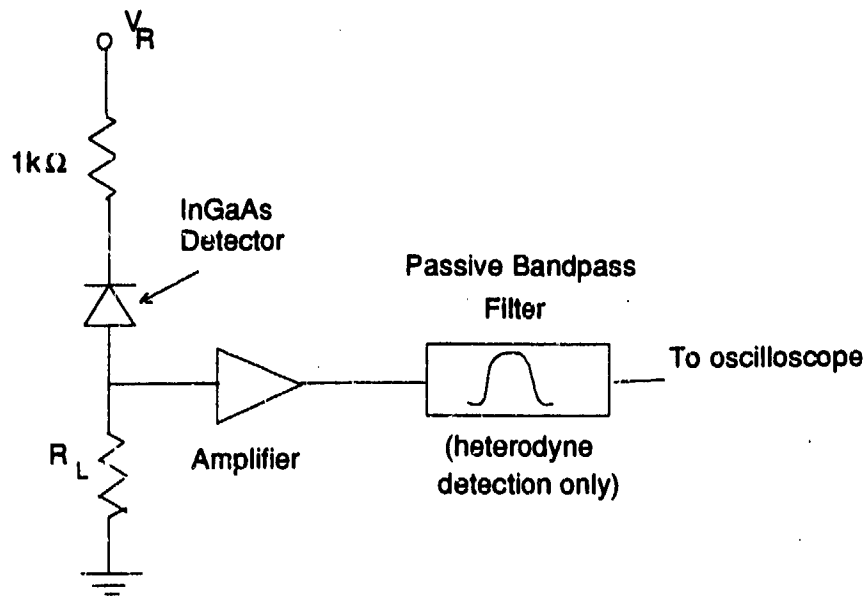


Figure 15: Detection package from CTI.

For the heterodyne detection case, the same reverse bias voltage, series resistance and photodiode are used (see Figure 15). The amplifier is different, being provided by Miteq, it has a bandwidth of 100 MHz and a midband gain of 53 dB [22]. To limit the bandwidth of the detection package and to isolate the return signal, a 41 MHz bandpass filter was used centered at the intermediate frequency, 27.1 MHz [20]. The decrease in the signal due to the bandpass filter is less than 1 dB. The load resistance R_L found by CTI for optimized heterodyne detection for this system at 27.1 MHz is 450Ω [20].

CHAPTER V

5.0 THEORETICAL COMPUTATIONS

This chapter will use the theory discussed in CHAPTER III and the values specified for the components in the detection electronics to calculate theoretical probabilities of detection for each detection scheme. In order to find the probability of detection the limiting mean squared noise current for each detection scheme needs to be identified. The limiting mean squared noise current will consist of a sum of all the noise currents. Some of the these noise currents will be small enough that their contribution is minimal and can be ignored. Once the sum of the dominating noise currents is found it will be used in the noise PDF to find the thresholds needed for the desired probabilities of false alarm. Once the thresholds are found, they can be used along with the limiting mean squared noise current in the probability density function of the current fluctuation to calculate the probability of detection. The probability of detection will then be plotted against signal-to-noise ratio to produce curves for each probability of false alarm.

5.1 Evaluation of Noise in the 2 μ m LADAR System

The noise sources discussed in CHAPTER III are dark current, Johnson, background, shot, and amplifier noise. The average theoretical values for these noise sources will be calculated for each detection scheme using the known characteristics of the system. Once the magnitude of these sources is know, a threshold can be calculated

for given probabilities of false alarm, and this threshold can be used to calculate the probability of detection for each case.

5.1.1 Dark Current Noise

Dark current shot noise is directly proportional to the dark current for a particular detector and each detector is unique even if it comes from the same processing lot. The dark current for one of the purchased p-i-n strained InGaAs photodiodes was measured to be 135 nA for the 3V reverse bias used in the detection bias circuit. For the coherent detection scheme the bandwidth is determined by the bandpass filter to be 41 MHz [22]. This gives a mean-square dark current shot noise for coherent detection of

$$\begin{aligned}\overline{i_{Dark}^2} &= 2qI_{Dark}B \\ &= 2(1.602 \times 10^{-19} C)(135 \times 10^{-9} A)(41 \times 10^6 Hz) \\ &= 1.77 \times 10^{-18} A^2\end{aligned}\quad (5.1.1)$$

The only difference between the two detection schemes is the bandwidth and for the incoherent detection scheme the Analog Modules amplifier determines the bandwidth. The bandwidth of the amplifier is 35 MHz [21]. This gives a mean square dark current shot noise for incoherent detection of $1.51 \times 10^{-18} A^2$.

5.1.2 Johnson Noise

Johnson noise is inversely proportional to the load resistance. According to CTI the optimum load resistance for coherent detection is 450Ω [20]. Therefore, the Johnson noise for the coherent case is

$$\begin{aligned}\langle i_J^2 \rangle &= \frac{4kTB}{R_{Load}} \\ &= \frac{4(1.38 \times 10^{-23} \text{ J/K})(293K)(41 \times 10^6 \text{ Hz})}{450\Omega} \\ &= 1.47 \times 10^{-15} A^2.\end{aligned}\quad (5.1.2)$$

For incoherent detection CTI gave an optimum load resistance of $16M\Omega$. The mean squared Johnson noise current for the incoherent case is then $3.54 \times 10^{-20} A^2$. This is much smaller than that for the coherent case but that was expected with the larger load resistor.

5.1.3 Background Noise

For this analysis the worst case scenario for background noise is assumed, which is, the scenario of the LADAR looking at a sun illuminated cloud. The amount of solar power received at the detector was given in CHAPTER III as

$$P_{SB} = k_1 S_{IRR} \Delta\lambda \Omega_R \rho \eta_{SYS} A_R \quad (5.1.3)$$

where k_1 is the fraction of solar radiation penetrating the Earth's atmosphere, S_{IRR} is the solar irradiance, $\Delta\lambda$ is the wavelength band of the optical band pass filter centered at 2.09 μm (see chapter 4), Ω_R is the solid angle over which the receiver collects energy from the radiating body (easily found by dividing the area of the beam at the target by the range to the target squared), ρ is the target reflectivity, η_{SYS} is the ladar system optical efficiency which includes the reflectivity of the mirrors in the system and all beam splitters, and A_R is the receiver area. The values used for these variables and their source are included in Table 2.

Substituting the values in Table 2 into (5.1.3)

$$\begin{aligned} P_{SB} &= (0.95) \left(0.01 \frac{W}{m^2 \text{Å}} \right) \left(380 \text{ Å} \right) \left(2.125 \times 10^{-9} \text{ sr} \right) (1)(0.65)(0.00785) \\ &= 3.91 \times 10^{-11} W \end{aligned} \quad (5.1.4)$$

Table 2:
Summary of values for background noise calculation.

Variable	Value	Units	Source of Information
k_b	0.95		RCA Electro-Optics Handbook, [23]
SIRR	0.01	W/m ² Å	"
$\Delta\lambda$	380	Å	Optical Filter Corporation(OFC) [24]
Ω_R	2.125x1	steradians	Area of Propagated Gaussian beam/Range ² , range=2000m
ρ	0.9		Worst case scenario.
η_{sys}	1		Actual measurement of the optical system throughput
A_R	0.65 .00785	m ²	Receiver area of 10 cm telescope

The shot noise current produced at the detector by the background power is [4],

$$\langle i_{Bk}^2 \rangle = 2qBR_{Dc}P_{SB} \quad (5.1.5)$$

where R_{Dc} is the detector responsivity in Amperes/Watt, q is the charge on an electron in Coulombs, and B is the electrical bandwidth of the receiver in Hertz. Substituting in the appropriate parameters, we find,

$$\begin{aligned} \langle i_{Bk}^2 \rangle &= 2(1.602 \times 10^{-19} C)(41 \times 10^6 Hz) \left(1.1 \frac{A}{W} \right) (3.915 \times 10^{-11} W) \\ &= 5.66 \times 10^{-22} A^2, \end{aligned} \quad (5.1.6)$$

For incoherent detection the bandwidth is 35 MHz so the background noise is $4.83 \times 10^{-22} A^2$.

5.1.4 Amplifier Noise

Amplifier noise is noise added to the signal when it goes through the amplifier. Amplifier noise is a thermal noise source and typically the noise for a particular amplifier is specified by the manufacturer using an equivalent temperature, T_A . The amplifier obtained

for this system is a 53 dB amplifier from Miteq, model AU-3A-0110 and the typical noise temperature is given by the manufacturer to be 78 Kelvin. The amplifiers, both for the coherent and the incoherent detection, see 50Ω for the load resistance. For coherent detection the amplifier noise is

$$\begin{aligned}\langle i_{Amp}^2 \rangle &= \frac{4kT_{Eq}B}{R_{Load}} \\ &= \frac{4(1.38 \times 10^{-23} \text{ J/K})(78K)(41 \times 10^6 \text{ Hz})}{50\Omega} \\ \langle i_{Amp}^2 \rangle &= 3.53 \times 10^{-15} \text{ A}^2\end{aligned}\quad (5.1.7)$$

For the incoherent case an equivalent noise temperature was not given by the manufacturer but, a measured input spectral noise density was given. The input spectral noise density is a measure of the noise added by the amplifier but it is specified at the input to the amplifier. Since all of our noise sources are being considered at the input of the amplifier this is convenient. The spectral noise density is specified by the manufacturer to be $0.612 \frac{\text{nV}}{\sqrt{\text{Hz}}}$. In order to get the noise voltage squared at the input of the amplifier the spectral noise density is squared and then multiplied by the bandwidth as seen below.

$$\langle v_{Amp}^2 \rangle = \left(0.612 \frac{\text{nV}}{\sqrt{\text{Hz}}}\right)^2 35 \times 10^6 \text{ Hz} = 1.31 \times 10^{-11} \text{ V}^2 \quad (5.1.8)$$

To find the noise current before the amplifier the voltage squared is divided by the input impedance of the amplifier, which is $1 \text{ M}\Omega$.

$$\langle i_{Amp}^2 \rangle = \frac{\langle v_{Amp}^2 \rangle}{R_i^2} = \frac{1.31 \times 10^{-11} \text{ V}^2}{(1 \times 10^6 \Omega)^2} = 1.31 \times 10^{-23} \text{ A}^2 \quad (5.1.9)$$

5.1.5 Shot Noise

Shot noise is the noise produced when light is incident on a detector. This noise is present in both coherent and incoherent detection. For coherent detection the desire is for

the system to be shot noise limited by illuminating the detection with the local oscillator beam. For the incoherent detection scheme shot noise is produced by the signal return from the target. In this section shot noise will be calculated for both cases.

5.1.5.1 Shot Noise in the Coherent Detection Case is produced by illuminating the detector with the local oscillator. To insure that shot noise dominates all other noise sources, the local oscillator power incident on the detector was increased until the shot noise was 10 dB above the dominant noise, which in our case is thermal noise (as seen in Section 5.1.2). The mean squared thermal noise current was calculated to be $1.47 \times 10^{-15} \text{ A}^2$ and if the local oscillator is increased until there is a 10 dB difference in the noise current the shot noise current should be $1.47 \times 10^{-14} \text{ A}^2$. These noise levels can be verified for the system on the spectrum analyzer.

Figure 16 shows the output of the detection electronics displayed on the spectrum analyzer with no local oscillator incident on the detector. The average noise level seen in Fig. 16 is -117.5 dBm. This can be compared to the dominating noise level predicted by finding the mean squared current that corresponds to this noise level. To do this the power that this corresponds to can be calculated as shown below.

$$\begin{aligned} -117.5 \text{ dBm} &= 10 \log\left(\frac{P}{1 \text{ mW}}\right) \\ P &= 1.778 \times 10^{-15} \text{ W} \end{aligned} \quad (5.1.10)$$

where P represents the amount of measured power with a 10 Hz resolution bandwidth. To correct for the resolution bandwidth the power is divided by the 10 Hz and then multiplied by the 41 MHz bandwidth of the detection electronics. This gives a power measured for the 41 MHz bandwidth of $7.29 \times 10^{-9} \text{ W}$. This was measured with the Miteq amplifier in place which has a 53 dB gain. Since all the noise sources have been calculated before the amplifier the effect of the amplifier needs to be taken into account, which gives

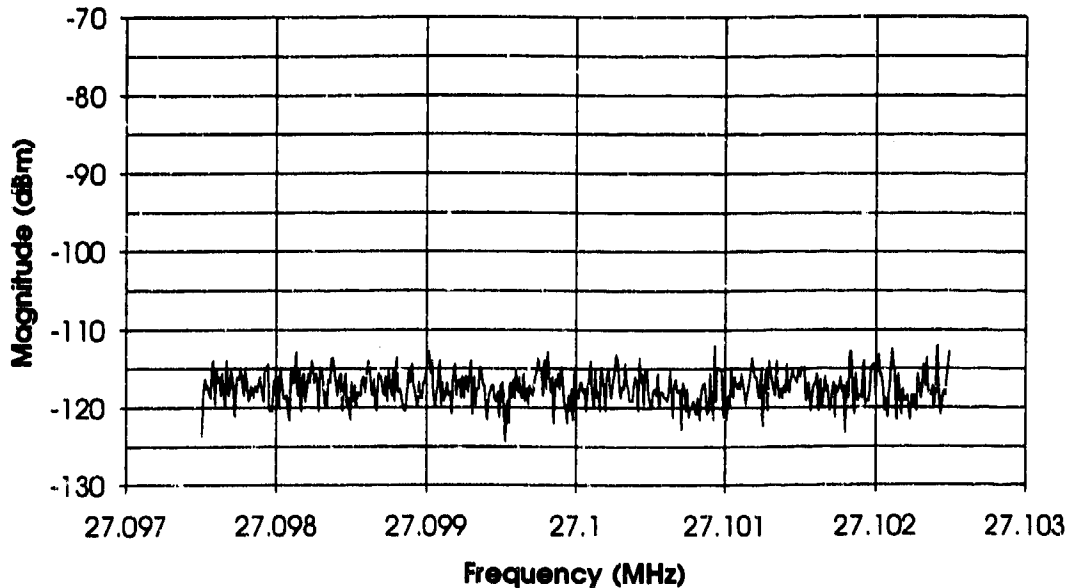


Figure 16: Spectrum analyzer display of output of coherent detection electronics using a 10 Hz resolution bandwidth.

a power of 3.65×10^{-14} W. Finally we want the mean squared current, so the power just calculated needs to be divided by the load resistance to get the mean squared current.

$$\langle i_{\text{Dominating Noise}}^2 \rangle = \frac{P}{50\Omega} = 7.31 \times 10^{-16} A^2 \quad (5.1.11)$$

The dominating noise for the coherent detection case is the sum of the two dominating noise terms thermal and amplifier noise. These were calculated in Eqs. (5.1.2) and (5.1.7) and the sum is $5.0 \times 10^{-15} A^2$ which is a factor of 6.8 more than the noise measured experimentally. A factor of 6.8 on the spectrum analyzer is 8.4 dB and the spectrum analyzer has an uncertainty of 4 to 5 dB.

The master oscillator laser was then used to illuminate the detector. The amount of power incident on the detector was increased until there was a 10 dBm difference in the amplitude, which was 1.25 mW of power. This result can be seen in Fig. 17.

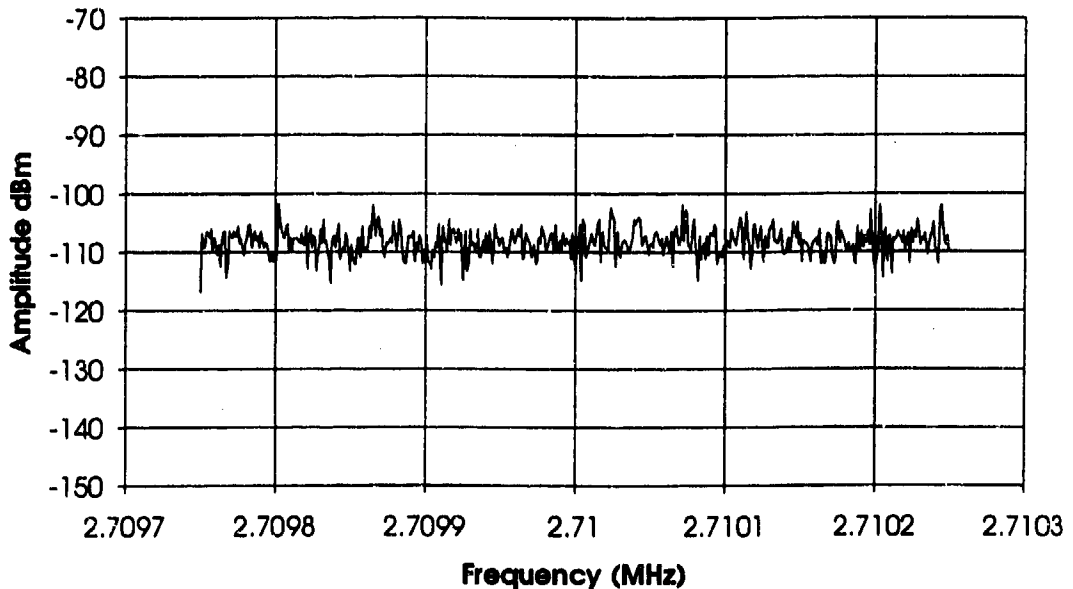


Figure 17: Spectrum analyzer output of coherent detection electronics with 1.25 mW of power incident on the detector.

The average noise level seen in Fig. 17 is -108.3 dBm. Using the same analysis as used for Fig. 16 the mean squared shot noise current is $6.08 \times 10^{-15} \text{ A}^2$ which is 9.2 dB less than the predicted shot noise level of $5.0 \times 10^{-14} \text{ A}^2$. The predicted shot noise level is 10dB above the sum of the thermal and amplifier noise terms. The 10dB level above the noise was chosen to ensure that the local oscillator would dominate the noise.

5.1.5.2 Shot Noise in the Incoherent Case is produced by the return from the target being incident on the detector. To calculate the shot noise produced in the incoherent detection scheme the power of the return (P_R) from the target needs to be determined, once the return power is known the amount of shot noise can be calculated.

To find the return power the radar range equation is used, which has the form [4]

$$P_R = \left(\frac{P_T}{\theta_B^2 R^2} \right) \left(\frac{\sigma}{4\pi R^2} \right) \left(\frac{\pi D^2}{4} \right) (\eta_{ATM}) \quad (5.1.12)$$

where P_T is the transmitted power, R is the range, θ_B is the beam divergence, σ_T is the target cross section, D is the diameter of the receiver, and η_{ATM} is the atmospheric transmission factor. The target cross section for an extended target is

$$\sigma_T = \pi \rho R^2 \theta_B^2 \quad (5.1.13)$$

where ρ is the reflectivity of the target. Equations (5.1.12) and (5.1.13) can be combined and reduced to

$$P_R = \frac{\pi P_T \rho D^2}{16 R^2} \eta_{ATM} \quad (5.1.14)$$

The values used for these variables are shown in Table 3.

Table 3:
Data used to obtain an estimate of the return power from the target.

Variable	Value
P_T	10 mJ/500 ns
R	2000 m
ρ	0.9
D	0.1 m
η_{ATM}	0.7

For the transmitted power it was assumed that the transmitted pulse was 10 mJ and the pulse length was 500 ns, which is typical for this system. The range chosen is typical of those used during the experimental process and target reflectivity was chosen earlier to be 1 but for a typical lambertian target it is 0.9. The atmospheric attenuation coefficient was found in the RCA Handbook[25]. These values can be substituted into Eq. (5.1.14) to

give a return power of $6.185 \mu W$. This can be used in the equation for the shot noise as shown below.

$$\begin{aligned}\langle i_{SN_{IN}}^2 \rangle &= 2qBP_rR_{Det} \\ &= 2(1.602 \times 10^{-19})(35MHz)(6.185\mu W)(1.1A) \\ &= 7.63 \times 10^{-17} A\end{aligned}\quad (5.1.15)$$

This noise happens to be the dominating noise.

Table 4:
Summary of theoretically calculated values for the discussed noise sources.

Noise Source	Detection Scheme	
	Coherent	Incoherent
Dark current	$1.77 \times 10^{-18} A^2$	$1.51 \times 10^{-18} A^2$
Thermal	$1.47 \times 10^{-15} A^2$	$3.54 \times 10^{-20} A^2$
Background	$5.66 \times 10^{-22} A^2$	$4.83 \times 10^{-22} A^2$
Shot	$1.50 \times 10^{-14} A^2$	$7.63 \times 10^{-17} A^2$
Amplifier	$3.53 \times 10^{-15} A^2$	$1.31 \times 10^{-23} A^2$

As can be seen from Table 4, coherent detection is dominated by shot noise which is greater than the otherwise dominating noise (the sum of thermal and amplifier noise) and for the incoherent detection case the dominating noise is the shot noise produced by the return signal from the target. This seems a bit surprising but the target used was only 2 km away, and it is not quite into the far field (far field, 2.4 km). In order to find the range at which the signal shot noise no longer dominates, Eqs. (5.1.13) through (5.1.16) were used in reverse order with the next largest noise source, which is dark current noise, to find the range at which shot noise from the signal is no longer the dominating noise.

This back calculation was done and the range at which signal shot noise no longer dominates is 14.2 km. This is probably further away than actually needed to make the system non-signal shot noise limited because the atmospheric transmission decreases as the range increases.

5.2 Calculation of the Probability of False Alarm

The major noise sources were analyzed in the previous section and the values of each of the noise sources was determined. Using the values of the dominating noise for each detection scheme and the PDF representing the fluctuation of the noise in the detection circuit, the threshold current can be calculated for different values of the probability of false alarm.

5.2.1 The Probability of False Alarm for Incoherent Detection

The equation for the probability of false alarm for incoherent detection was given in Eq. (3.4.4) as

$$Pin_{FA} = 0.5 \operatorname{ERFC} \left(\frac{i_T}{\sqrt{2 \langle i_{Incoh,SN}^2 \rangle}} \right). \quad (5.2.1)$$

The dominant incoherent noise when no signal is present, $\langle i_{Incoh,SN}^2 \rangle$, is dark current thermal noise which is $1.51 \times 10^{-18} \text{ A}^2$. Once Pin_{FA} is chosen i_T can be found. In other publications [1,2,4] probabilities of false alarm have been chosen between 10^{-1} to 10^{-16} . For this work, probabilities of false alarm of 10^{-2} , 10^{-4} , 10^{-6} , 10^{-8} , and 10^{-10} were chosen. The complementary error function can now be evaluated iteratively until a threshold current is found that gives the chosen values for the probability of false alarm.

The values found for the threshold current for the different probabilities of false alarm are tabulated in Table 5.

Table 5:

Threshold currents for different probabilities of false alarm for incoherent detection.

Probability of False Alarm	i_T (nA)
10^{-2}	2.860
10^{-4}	4.573
10^{-6}	5.846
10^{-8}	6.902
10^{-10}	7.824

5.2.2 The Probability of False Alarm for Coherent Detection

The equation for the probability of false alarm for coherent detection was given in Eq. (3.4.6) as

$$P_{CO_{FA}} = \exp\left(-\frac{i_T^2}{2\langle i_{Coh,SN}^2 \rangle}\right). \quad (5.2.2)$$

Using the same procedure as for incoherent detection, the values for the threshold current were found and are listed in Table 6.

Table 6:
Threshold currents for different probabilities of false alarm for coherent detection.

Probability of False Alarm	i_T (nA)
10^{-2}	371.7
10^{-4}	525.7
10^{-6}	643.9
10^{-8}	743.5
10^{-10}	831.3

5.3 Calculation of the Probabilities of Detection

Now that the threshold currents have been calculated, the probabilities of detection can be calculated for each detection technique and for each type of target.

5.3.1 Calculation of the Probability of Incoherent Detection with a Glint Target

The equations for calculation of the probability of detection for incoherent detection with a glint target were given in Eq. (3.5.3) as

$$P_{d_{IG}} = \begin{cases} 0.5ERFC\left(\frac{(i_T - \langle i_{Glint} \rangle)^2}{(2(\langle i_{Incoh,SN}^2 \rangle + 2qB\langle i_{Glint} \rangle))^{\frac{1}{2}}}\right) & \text{where } i_T - \langle i_{Glint} \rangle \geq 0 \\ 0.5\left[1 + ERF\left(\frac{(\langle i_{Glint} \rangle - i_T)^2}{(2(\langle i_{Incoh,SN}^2 \rangle + 2qB\langle i_{Glint} \rangle))^{\frac{1}{2}}}\right)\right] & \text{where } i_T - \langle i_{Glint} \rangle < 0 \end{cases} \quad (5.3.1)$$

where $\langle i_{Glint} \rangle$ is the average current produced by the signal incident on the detector, B is the bandwidth of the detection circuit, q is the charge of an electron, and $\langle i_{Incoh,SN}^2 \rangle$ is the mean squared noise current for incoherent detection, which is signal shot noise. These

equations can be used to plot the probability of detection versus SNR (signal-to-noise ratio) using $SNR = 10 \log[\langle i_{G_{int}} \rangle^2 / \langle i_{Incoh,SN}^2 \rangle]$, the calculated mean squared dominant noise (Table 4), the threshold currents for incoherent detection (Table 5), the bandwidth for the incoherent detection circuit, and by varying $\langle i_{G_{int}} \rangle$. This equation was plotted by using increasing values for $\langle i_{G_{int}} \rangle$ which gave increasing values for SNR and for the probability of detection which is easily seen in Fig. 18. Looking at Fig. 18, as the probability of false alarm decreases a greater average SNR is needed to achieve the same probability of detection as for a greater probability of false alarm. It can be seen that for a particular probability of false alarm, as the average SNR increases, the probability of detection also increases. It can also be seen that for a particular probability of false alarm as the average SNR increases the probability of detection also increases. This makes sense. If the average SNR increases then either the noise has decreased (don't we wish) or the average amount of signal received has increased. If the average amount of signal has increased then there would be less of a chance of missing a return, decreasing the probability of a miss and increasing the probability of detection.

5.3.2 Calculation of the Probability of Incoherent Detection with a Speckle Target

The equation to calculate the probability of detection for this case was given in Eq. (3.5.7) which is

$$Pd_{IS} = \frac{1}{2} \int_0^\infty ERF C \left(\frac{x_T - (\langle n \rangle + bW)}{\sqrt{2(\langle n \rangle + bW)}} \right) \frac{a^M W^{M-1} \exp(-aW)}{\Gamma(M)} dW. \quad (5.3.2)$$

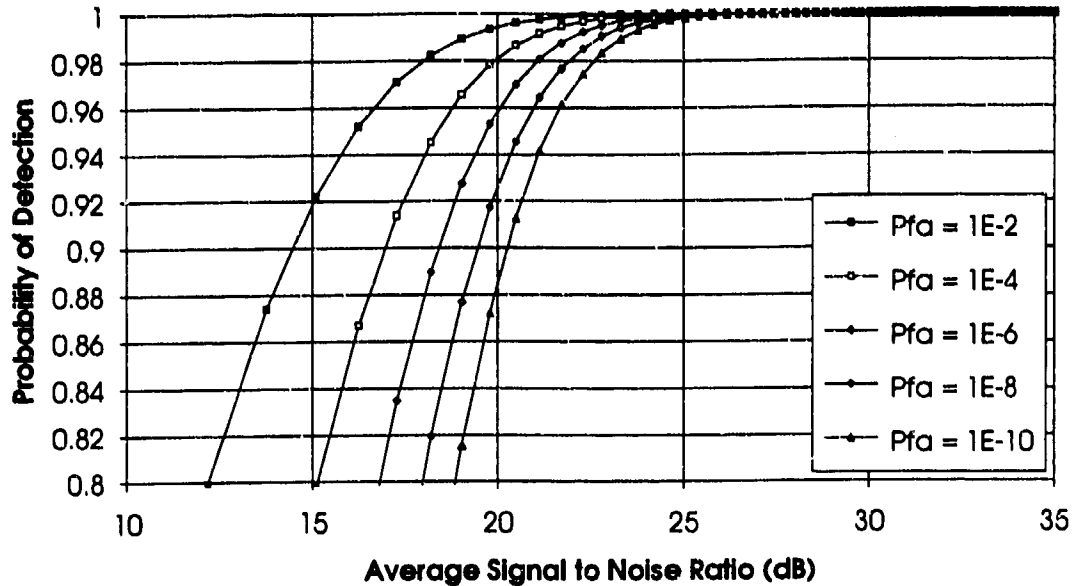


Figure 18: Curves representing the probability of detection for incoherent detection with a glint target for various probabilities of false alarm.

where x_T is the threshold number of electrons found by dividing the threshold current given in Table 5 by $q/\Delta t$, where q is the charge of an electron and Δt is the transmitted pulse length (for this work $\Delta t = 500\text{ns}$), M is the number of speckle lobes received by the receiver which for equal entrance and exit aperture diameters is equal to 4 [15], $\langle n \rangle$ is the mean number of noise electrons; that is, the mean noise current for incoherent detection expressed in terms of electrons, W is return energy incident on the target, $\langle W \rangle$ is the average received energy from the target, and $a = M/\langle W \rangle$. Equation (5.3.2) was integrated numerically over W and was plotted verses average SNR ($\text{SNR} = 10 \log(\langle W \rangle^2 / \langle n \rangle^2)$) by using increasing values for $\langle W \rangle$ and by using different values of the threshold current as shown in Fig. 19. The general trends of both Figs. 18 and 19 are the same, but we can compare the two since incoherent detection is being used in both cases and the only difference is the type of target being used. For a glint target it

would be expected that the probability of detection will be greater for a given average SNR than for a speckle target. This can be seen in these two plots, for a given probability of false alarm, as the average SNR increases the probability of detection increases faster for a glint target than for the speckle target.

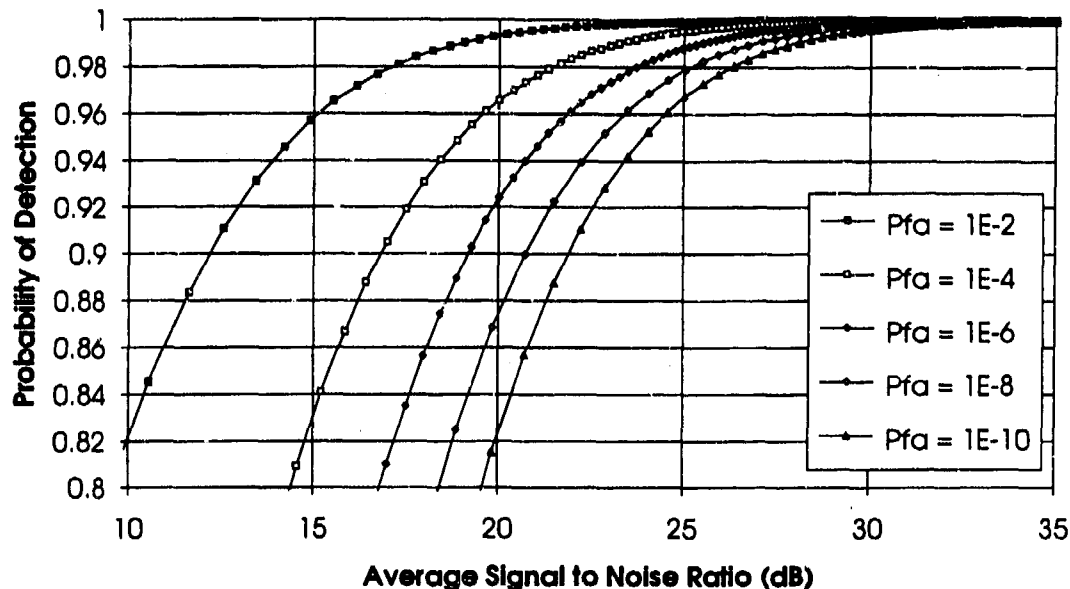


Figure 19: Curves representing the probability of detection for incoherent detection with a speckle target for various probabilities of false alarm.

5.3.3 Calculation of the Probability of Coherent Detection with a Glint Target

An expression for the probability of detection with a glint target when using coherent detection was given in Eq. (3.5.9) as

$$Pd_{CG} = \int_{i_T}^{\infty} \frac{2i}{\langle i_{Coh,SN}^2 \rangle} \exp\left[-\frac{i_{Glint}^2 + i^2}{\langle i_{Coh,SN}^2 \rangle}\right] I_0\left(\frac{2i_{Glint}i}{\langle i_{Coh,SN}^2 \rangle}\right) di. \quad (5.3.3)$$

Using the threshold current, i_T , given for different probabilities of false alarm in Table 6, the dominating mean squared coherent noise, $\langle i_{Coh,SN}^2 \rangle$, given in Table 4 and by varying i_{Glint} this equation can be plotted against the average signal-to-noise ratio (SNR). The

average SNR was calculated by $SNR = 10 \log(i_{Glint}^2 / \langle i_{Coh,SN}^2 \rangle)$. This equation for the probability of detection was plotted as described and it is shown in Fig. 20. The same trends are exhibited in Fig. 20 as seen in the previous plots for incoherent detection.

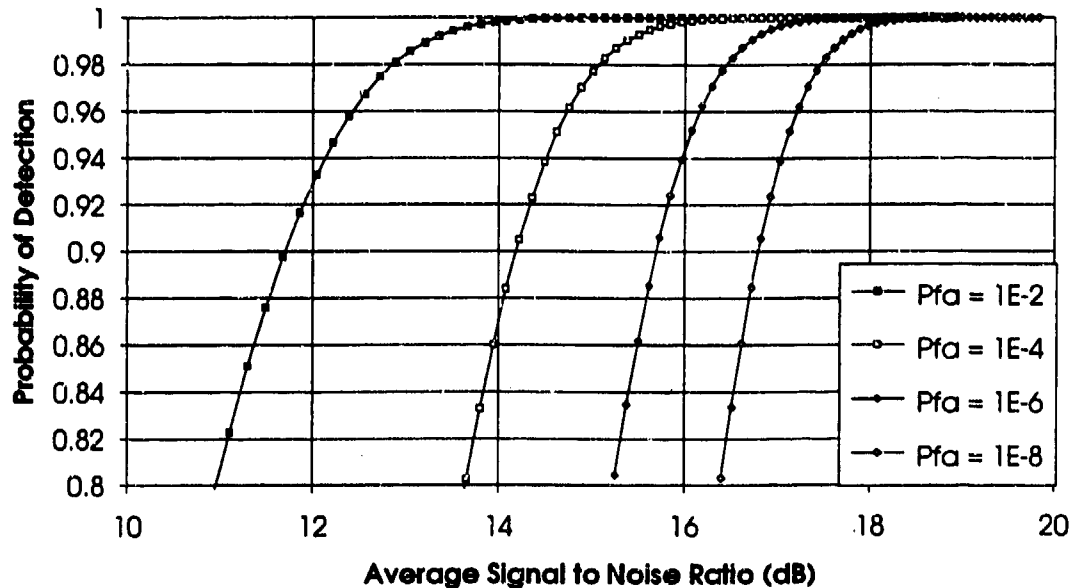


Figure 20: Curves representing the probability of detection for coherent detection with a glint target for various probabilities of false alarm.

5.3.4 Calculation of the Probability of Coherent Detection with a Speckle Target

The equation for the probability of detection for this case was given in Eq. (3.5.11) as

$$Pd_{CS} = \exp \left[-\frac{i_T^2}{\langle i_{Coh,SN}^2 \rangle + \langle i_{Diffuse}^2 \rangle} \right], \quad (5.3.4)$$

where $\langle i_{Coh,SN}^2 \rangle$ is the mean squared noise current for coherent detection which was given in Table 4 as $1.50 \times 10^{-14} \text{ A}^2$, i_T is the threshold current for a particular probability of false alarm and is given in Table 6, and $\langle i_{Diffuse}^2 \rangle$ is the mean squared signal current from the

diffuse target. This equation is easily plotted (see Fig. 21) by varying $\langle i_{Difuse}^2 \rangle$ for different signal to noise ratios ($SNR = 10 \log(\langle i_{Difuse}^2 \rangle / \langle i_{Coh,SN}^2 \rangle)$).

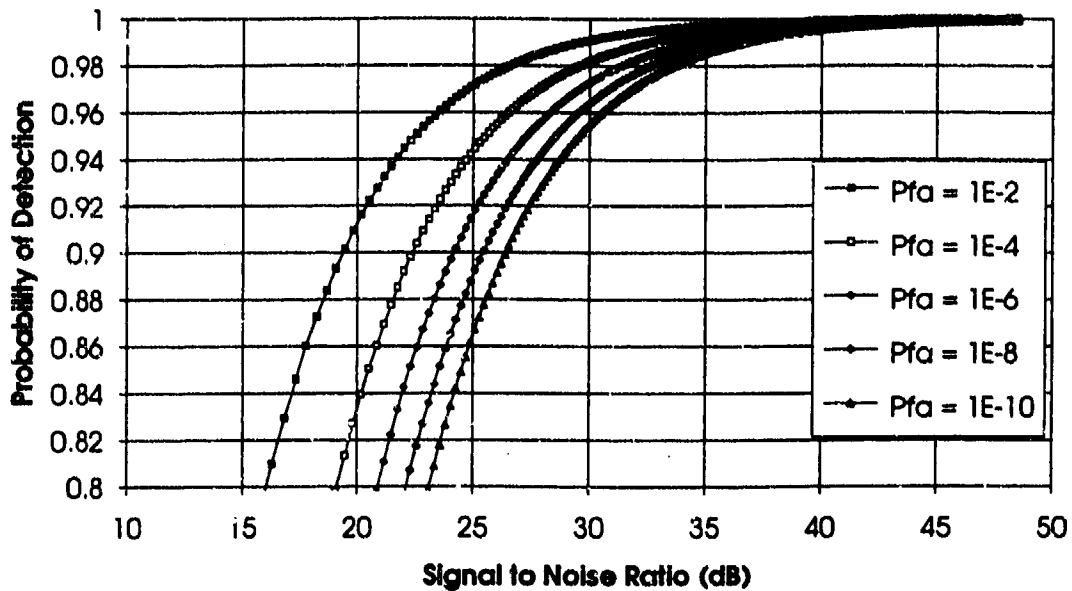


Figure 21: Curves representing the probability of detection for coherent detection with a speckle target for various probabilities of false alarm.

5.3.5 Comparison of Coherent to Incoherent Detection for a Glint Target Using the Probability of Detection

Now that we have curves representing the theoretical probabilities of detection for both coherent and incoherent detection with a glint target, they can be compared to each other by plotting both Figs. 18 and 20 on the same graph as seen in Fig. 22. In Fig. 22, coherent detection performs better than incoherent detection for probabilities of detection greater than 0.82. However the scale on the horizontal axis is only one dB per division and the largest difference between curves for a like probability of false alarm is 0.25 dB which is a factor of 1.06. This result was expected with a glint target where the return signal is a very strong deterministic return. These results suggest that for a situation with

no turbulence the detection techniques should perform similarly. To understand the surprising nature of this result it is important to remember that this is for a signal shot noise limited incoherent detection scheme. For longer ranges this system would no longer be signal shot noise limited but it would be limited by the dark current noise produced by the dark current of the photodiode.

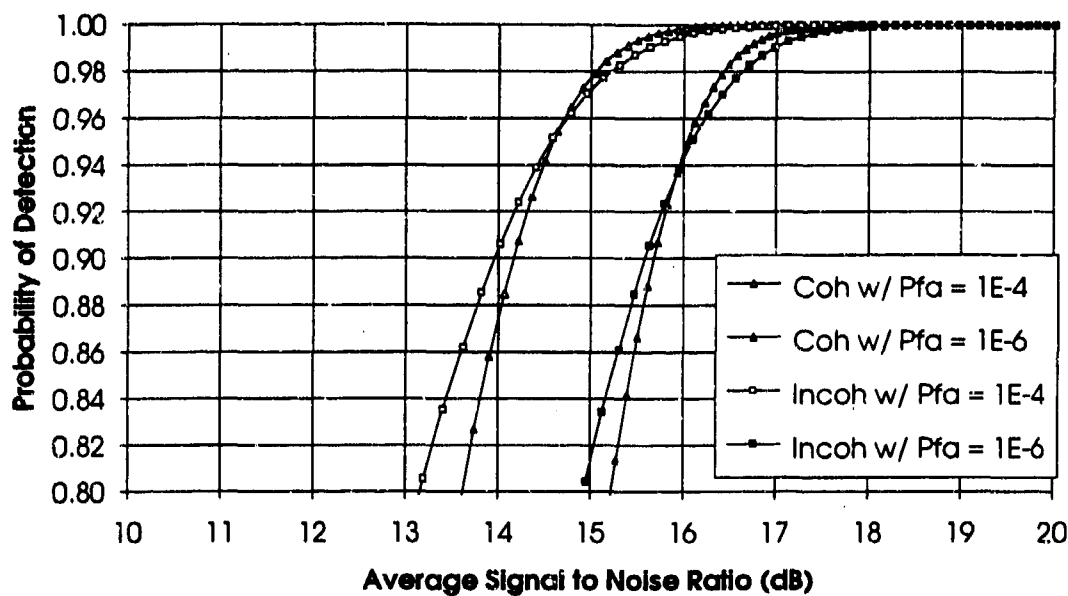


Figure 22: Comparison of the probability of detection for coherent vs. incoherent detection with a glint target.

5.3.6 Comparison of Coherent to Incoherent Detection for a Speckle Target Using the Probability of Detection

To compare coherent and incoherent detection for a speckle target Figs. 19 and 21 were combined and the result is shown in Fig. 23. As can be seen in the figure, the incoherent detection scheme can detect a target with a lower signal-to-noise for a given probability of detection than the coherent detection scheme can. This was an unexpected result. Since both schemes are shot noise limited they should perform identically. The

difference in performance between the two detection schemes is explained by the heterodyne mixing efficiency and speckle averaging over the receiver aperture. In coherent detection the mixing of the LO with the received signal is not perfect because of distortion in the wave front caused by propagation through the atmosphere. This causes only a fraction of the return to mix with the LO. Speckle averaging occurs when the receiver aperture of the system receives more than one speckle lobe. In the incoherent case since the detector does not care about the phase of the return, all the return energy is seen by the detector. Although, this is not the case for coherent detection. The LO will only mix with those speckle lobes that are in phase with the LO. So the incoherent scheme effectively averages the return speckles over the surface of the detector.

If this system were to be used at larger ranges the system would cease to be signal shot noise limited and then the system would be thermally noise limited. The statistics would then be different and the coherent detection scheme would perform better than the incoherent scheme.

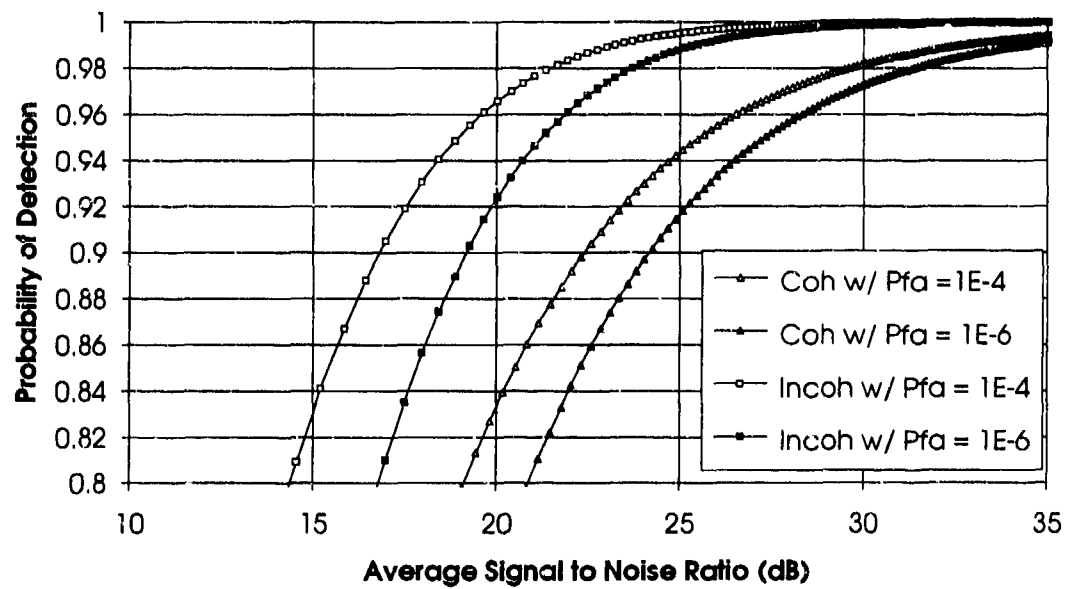


Figure 23: Comparison of the probability of detection for coherent vs. incoherent detection with a speckle target.

CHAPTER VI

6.0 Experimental Plan

This chapter includes a discussion on the data needed to demonstrate the probability density functions used to predict the probabilities of detection, the data needed to verify the probability of detection, the targets used to collect this data, the shape of the return and how this data was collected and stored.

6.1 Required Data

The theoretical predictions for the fluctuation in the detected output were done assuming a peak envelope detected return signal as will be discussed shortly. In order to be consistent with the theory the experimental return data will also be peak envelope detected. Because of the characteristics of the target and the detection process the peak of the return will fluctuate. The distributions of these fluctuations can be seen by plotting a histogram of the number of pulses versus the amplitude of the peak of the return. For a large number of shots, each bin represents the probability of that amount of power occurring as a return. The distribution of the plotted data therefore represents the probability function of the data. By integrating the previously discussed PDF's the experimental data can then be compared to theory.

To verify the probability of detection, data needs to be collected for just the noise in the system while the system is running. Using this collected data a threshold can be set

for a given probability of false alarm. This threshold can then be compared to the data taken to see what probability of detection our system would give.

In order to see the fluctuations just caused by the target and the detection scheme alone, the transmitted pulse has to be a constant amplitude. For this system, the output energy fluctuates a good deal. An example of the fluctuation in the output pulse can be seen in a histogram of the transmitted energy shown in Fig. 24. To eliminate this

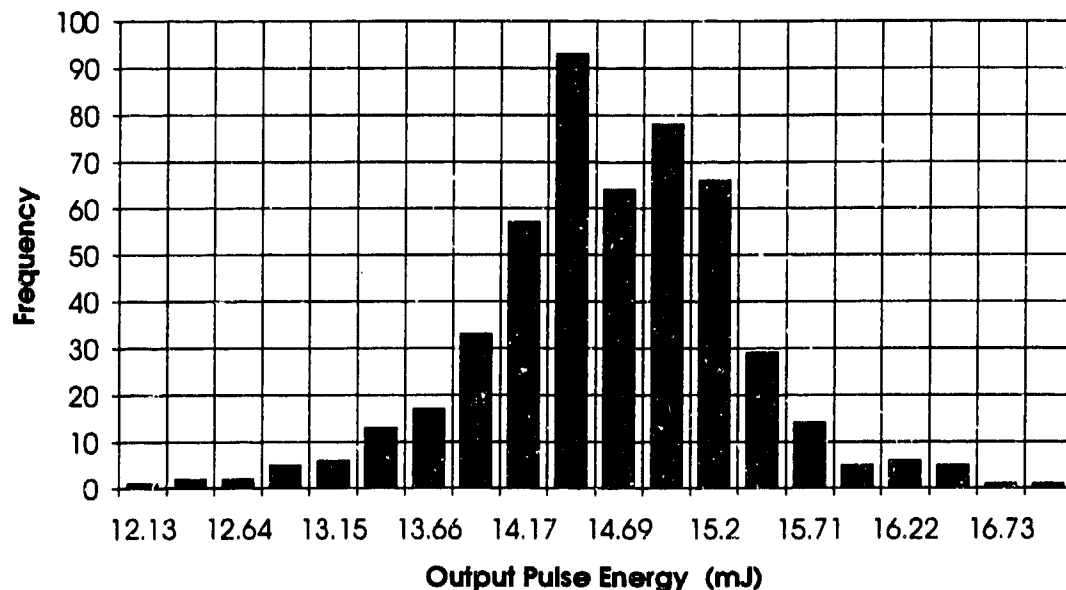


Figure 24: Fluctuation in output energy of slave oscillator.

fluctuation in the transmitted pulse the amount of energy transmitted by the laser will have to be recorded along with the magnitude of the return pulse. This will allow for a normalization of the transmitted pulse energy which will eliminate fluctuation caused by the fluctuation in the energy in the transmitted pulse.

6.2 Data Acquisition

The data to be acquired, as just discussed, is the magnitude of the peak of the return and the magnitude of the transmitted pulse for both a glint and a speckle target, as detected by incoherent and coherent means. This section includes a discussion of the targets used to collect the data, the format of this data, and the method used for acquiring this data.

6.2.1 Targets Used

Several different targets were used throughout testing. For a speckle/diffuse target a 2' x 2', 99% lambertian target at $2.09\mu\text{m}$ was purchased from Labsphere Inc. Since this target is lambertian it should have nearly perfect speckle target characteristics. Along with this lambertian target a 2.5' x 3.5' flame sprayed Aluminum target was also used as a speckle target. For a glint target a cornercube reflector was first used. Then it was realized that the refractive turbulence caused by temperature differences in the path of the beam were causing the beam to wonder on and off the cornercube. To resolve this problem a large retro-reflector was needed. As a solution, 65 red bicycle reflectors were purchased and they were mounted to a piece of plywood to give a large 2' x 2' glint target.

6.2.2 Data Format

To compare the data to the theoretical predictions the required information is the peak of the return and the peak of the transmitted energy. For coherent detection the return waveform, as displayed on the Tektronix's DSA 602A oscilloscope, output from the detection circuit electronics is shown in Fig. 25. The oscillation seen in the waveform is near the intermediate frequency of 27.1 MHz which can be seen by taking the Fourier Transform of the waveform, which is shown in Fig. 26. The waveform used when doing the peak envelope detection was the waveform seen in Fig. 25. Normally an envelope

detector is used to extract the pulse but, since the system was only operating at 3 Hz the waveforms themselves were stored for later analysis.

For incoherent detection the output of the electronics is shown in Fig 27. The shape of the return pulse is caused by a differentiation that occurs in the detection circuit electronics. For this analysis the maximum of the absolute value of the pulse was used in the data collection as the peak of this waveform. Due to this, the square of the return was taken and in the data analysis, once the peak was found, the square root of that peak was taken.

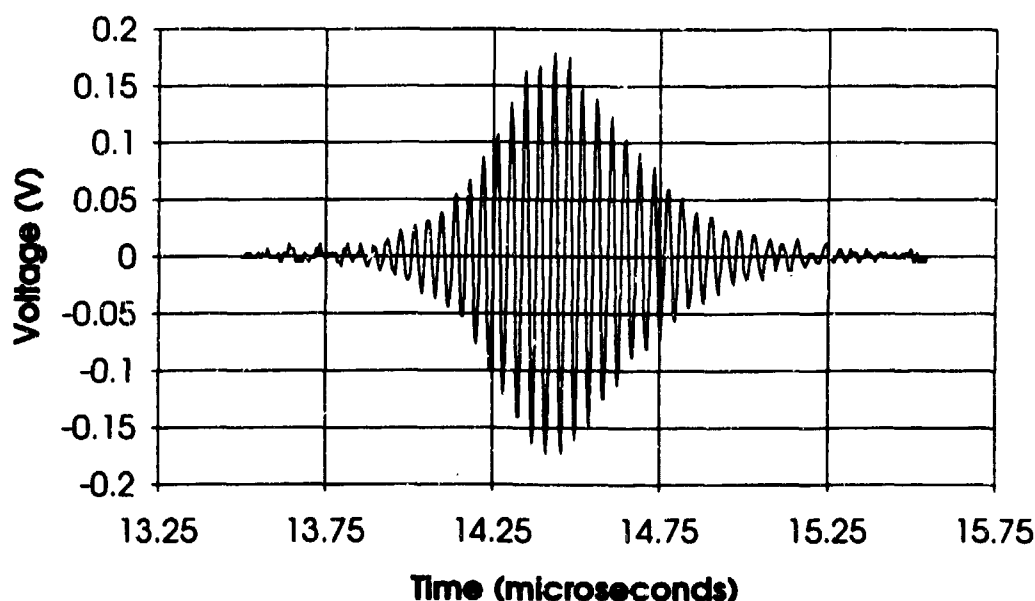


Figure 25: Example of a coherent return as seen on the Tektronix DSA 602A oscilloscope.

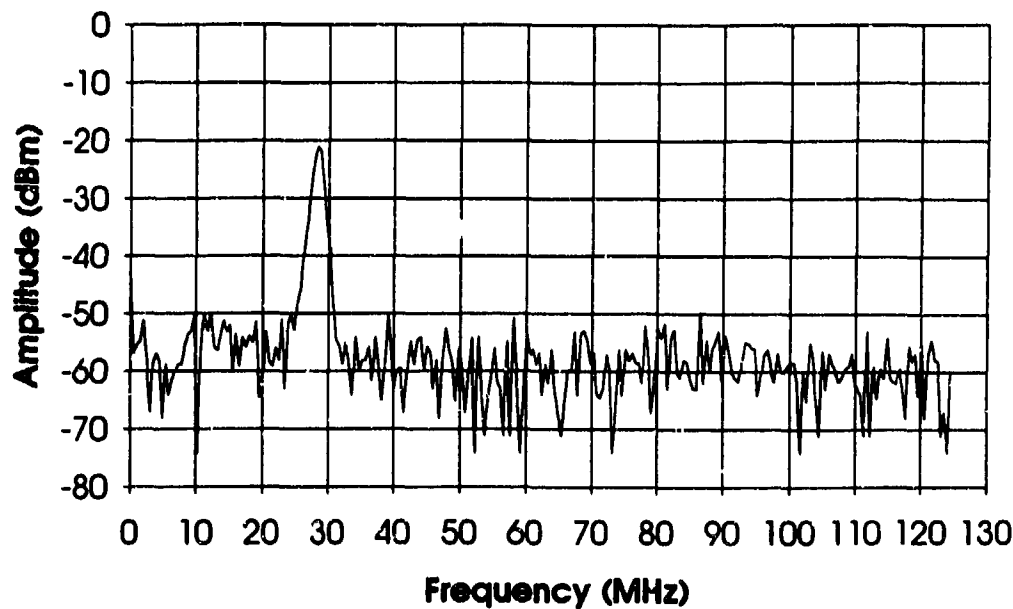


Figure 26: Example of the Fourier Transform of coherent detection return waveform.

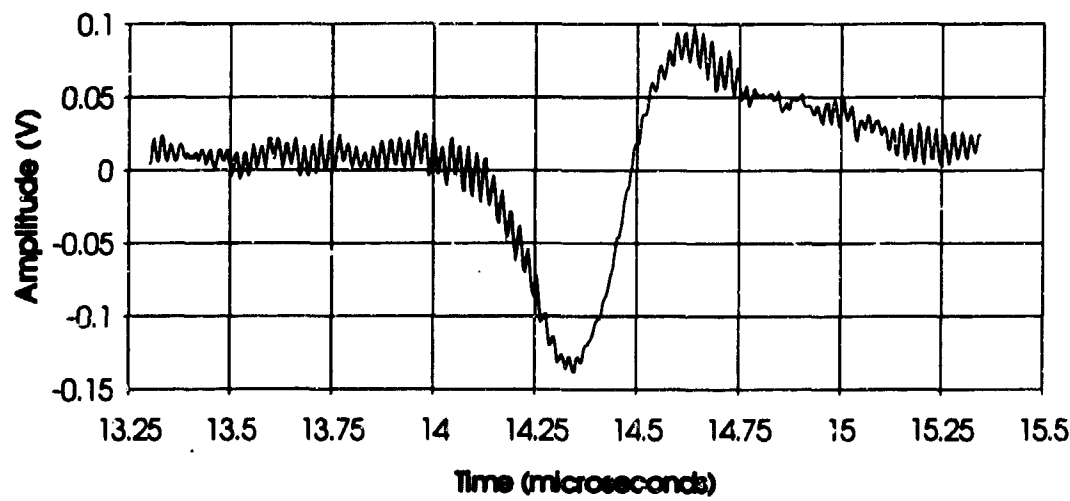


Figure 27: Example output of incoherent detection electronics.

The final waveform that is of interest is the amount of transmitted energy for each pulse. This was easily measured using the leakage from the thin film Brewster's angle polarizer shown in Fig. 8 using the Molelectron JD1000 Joule meter. This meter has a BNC

connection on the back that is called "pulse output". This output gives a voltage that is proportional to the amount of energy incident on the detector. The proportionality constant is 8 V/J [27]. So by dividing the peak of the transmitted pulse by 8 V/J the average energy in the transmitted pulse will be displayed. An example of the waveform stored from the Molelectron is shown below in Fig. 28. The peak of Fig. 28 shows the peak of the average transmitted energy for a single pulse measured from the leakage through the Brewster's angle polarizer. The ratio of the transmitted energy to the leakage was measured to be 15.3:1. So multiplying the peak of the pulse in Fig. 28 by 15.3, gives about 9 mJ transmitted energy.

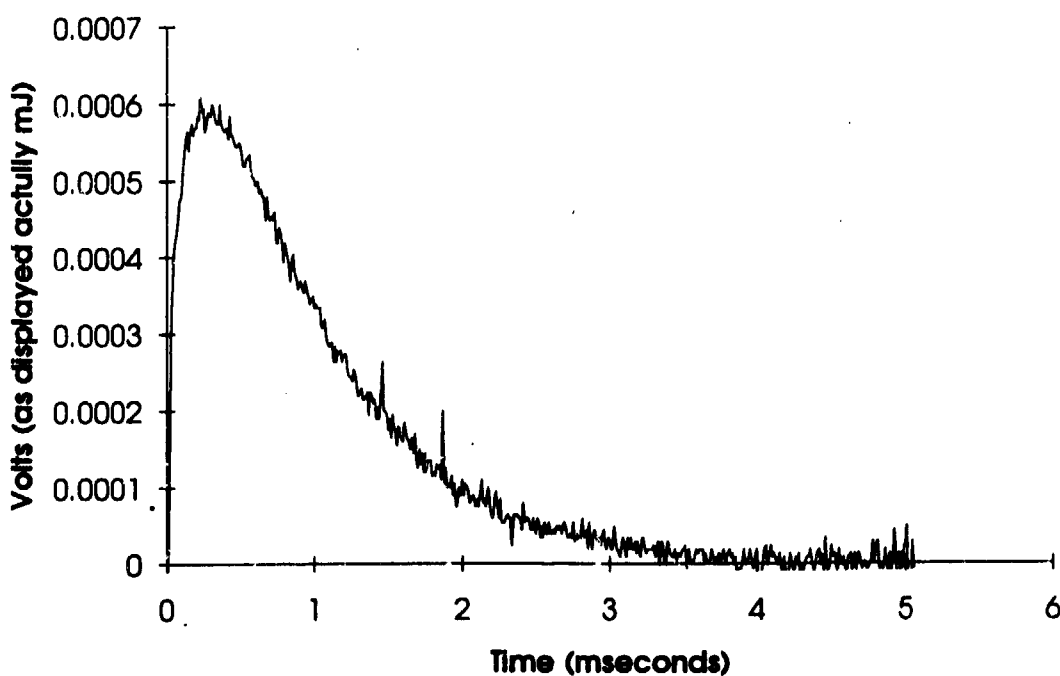


Figure 28: Average Transmitted pulse energy as displayed on the DSA 602A oscilloscope.

6.2.3 Data Collection

The best method of data collection found with the available equipment was to store each waveform, the transmitted pulse energy and the return signal, in the available RAM of Tektronix's DSA 602A oscilloscope. The RAM of the oscilloscope can hold up to 900 waveforms. Since both the transmitted energy and the return signal are being stored the number of actual data points per data set is only about 450. Once the memory is full the data can be copied to a 3.5" floppy disk in binary format for later analysis.

6.3 Experimental Procedure

To take data using the $2.09 \mu\text{m}$ LADAR system, the system needs to be up and running. The slave laser is the first device to be turned on. It is usually operated at a repetition rate of 2.8 Hz with 900 V applied to the flash lamps. It is a good practice to check the alignment of this laser by optimizing the output using the Molelectron JD1000 energy meter. Once the output is optimized to around 15-20 mJ, Q-switched, then it is time to turn on the MO, AOM and the servo system. Once on, the servo system will begin dithering the cavity trying to lock onto the wavelength of the MO. The servo system may also need to be adjusted in order to lock onto the correct mode.

Once the system is up and running the output beam can be directed toward the test field. The test field used was Wright Field at Wright-Patterson Air Force Base. This testing took place from the 11th floor of the tower in building 620, which was built to do radar testing on Wright Field. Using the Aerotech beam steerer the beam can be pointed at the target of interest. The targets of interest were placed on the test range, while other targets are available if desired; e.g. tanks, air planes, and trucks. Once the beam is consistently striking the target it is left staring at the target until both methods of detection are used and recorded.

All that is left at this point is to get the Tektronix, DSA 602A oscilloscope to record the needed data. To do this, the scope was setup to trigger off of the back scatter from the secondary mirror of the telescope shown in Fig. 8, produced by the transmitted pulse. With this oscilloscope there is the ability to display two different wave forms on two different windows. Therefore the return pulse is displayed in one window and the transmitted pulse measured by the Molelectron detector was displayed in the other window. Now that both wave forms are displayed, the oscilloscope was set to store both wave forms in RAM. Once the data was stored in RAM it could be transferred to floppy disk were analysis could be easily done on the data at a later time.

CHAPTER VII

7.0 ANALYSIS OF DATA

This chapter consists of a discussion of peak detection of the stored experimental data, manipulation and plotting of that experimental data, comparison of experimental data to theory and determining the theoretical goodness fit, explanation for the deviations from theory and finally a discussion on the probability of detection.

7.1 Peak Detection

The theory done to describe the fluctuations in the output current from the electronics assumes peak envelope detection. As described in the previous chapter the entire wave form of both the transmitted pulse and the return signal were stored. This section describes how the peak of each return was extracted from the stored data.

Each data set was stored by the Tektronix 602A oscilloscope on a 3.5" disk. On each disk are approximately 900 files stored in sequential order using the file names: sto1.wfb, sto2.wfb, sto3.wfb, ... etc. Since the transmitted pulse energy corresponding to each return was stored, there should be an even number of files. The file extension ".wfb" indicates that the file was stored in binary format. Since both the peak of the return and the peak of the transmitted energy are of interest a program was written in C by Joe Gillette, of Technology/Scientific Services, called "maxparse," that opened each file,

searched for the maximum in that file and stores that value in a user named comma separated value (csv) file. Since the return and the transmitted energy were stored sequentially alternating between the two, the maximums were stored in two columns in the user named file.

7.2 Comparison of Data with Theoretical Expectations

In this section the methods used to compare the experimental measurements to the theoretical expectations is discussed. The first section discusses how the transmitted pulse energy was normalized to eliminate the effects of the fluctuation in the transmitted energy. The second section presents the χ^2 goodness of fit test that will be used to determine whether the theory fits the experimental data. The next four sections discuss the probability distributions measured for each detection scheme for both types of targets and how the theoretical predictions fit those experimentally measured distributions. Finally, the probability of detection is discussed.

7.2.1 Normalization of Transmitted Pulse

Once the data set has been reduced to a file that is in the comma separated value format it can be loaded into Microsoft's Excel. The rest of the analysis on this data has been done in Excel. In order to see the fluctuation in the detector current caused by target and detection characteristics, the effects of the fluctuation in the output pulse need to be normalized. To do that the measured voltage corresponding to the return is divided by the value recorded as the transmitted energy. The value recorded is not the transmitted energy sent to the target but it is the leakage out of the Brewster's angle polarizer which is about 1/15.3 of the transmitted pulse. So the actual transmitted pulse is 15.3 times the value recorded. This will give some unusual units to the x-axis but that is not of concern since the shape of the probability distribution is the main concern.

Now that the pulse to pulse fluctuation of the SO has been accounted for the data can be plotted in a histogram. The x-axis of the histogram is the ratio of the received signal voltage divided by the average transmitted energy and the y-axis is the number of times that this values occurs during the data set, which is referred to as the frequency.

7.2.2 *Chi² Goodness of Fit Test*

When testing experimental data against a hypothesized probability density function, the theoretical curves can be compared to the experimental data and then the quality of the theoretical fit determined. One method of determining the goodness of fit is a chi-squared (χ^2) test. The χ^2 statistic is defined as (see Appendix B) [28]

$$\chi^2 = \sum_{j=1}^c \frac{(O_j - E_j)^2}{E_j} \quad (7.2.1)$$

where O_j is the observed frequency (experimentally measured), E_j is the expected (theoretical) frequency and c is the number of classes. Equation (7.2.1) represent a random variable that has an approximate χ^2 -distribution with $c-1$ degrees of freedom. The number of degrees of freedom distinguishes between the members of the χ^2 -distribution family. When determining the number of degrees of freedom for the theoretical distribution the equation is

$$\text{Degrees of Freedom} = c - 1 - e \quad (7.2.2)$$

where e is the number of estimated or calculated parameters in the theoretical distribution and c in my case, as will be seen later, is the number of bins in a histogram. Examples of estimated parameters would be the mean and/or the variance used in the theoretical distribution when they were measured from the data.

The χ^2 distribution is a tabulated function that can be found in any statistics book, an example of which is shown in Appendix B. Knowing the number of degrees of freedom and the level of significance, the tabulated χ^2 value can be compared to that calculated for the data. The level of significance is the probability of rejecting the hypothesis even though the hypothesis is true. To better explain the level of significance an example is given as follows: If the measured data are samples of a Gaussian random variable, and a decision threshold (or level of significance) of 0.1 was selected, there is still a 10% chance the data will fail the test and the hypothesis will be "rejected" - that is, we incorrectly decide the density is not a Gaussian. The standard level of significance used when comparing theoretical curves to experimental curves is 10%, which has been used before in the laser radar community and will be used for this work.

In order to demonstrate how the χ^2 test is carried out an example follows. Assume that a distribution has 10 degrees of freedom and a calculated χ^2 value of 14.6. Looking at the tabulated cumulative χ^2 -distribution (Appendix B) for 10 degrees of freedom at the 0.1 level of significance (0.90 in the table) the χ^2 value needs to be less than 16.0 to accept the theoretical distribution. The calculated value was 14.6 which is less than 16.0 so this would be accepted as a good fit.

7.2.3 Analysis of Incoherent Detection with a Speckle Target

In this section the data measured for incoherent detection with a speckle target will be presented and the process used to fit the theoretical probability density function to the theory will be discussed.

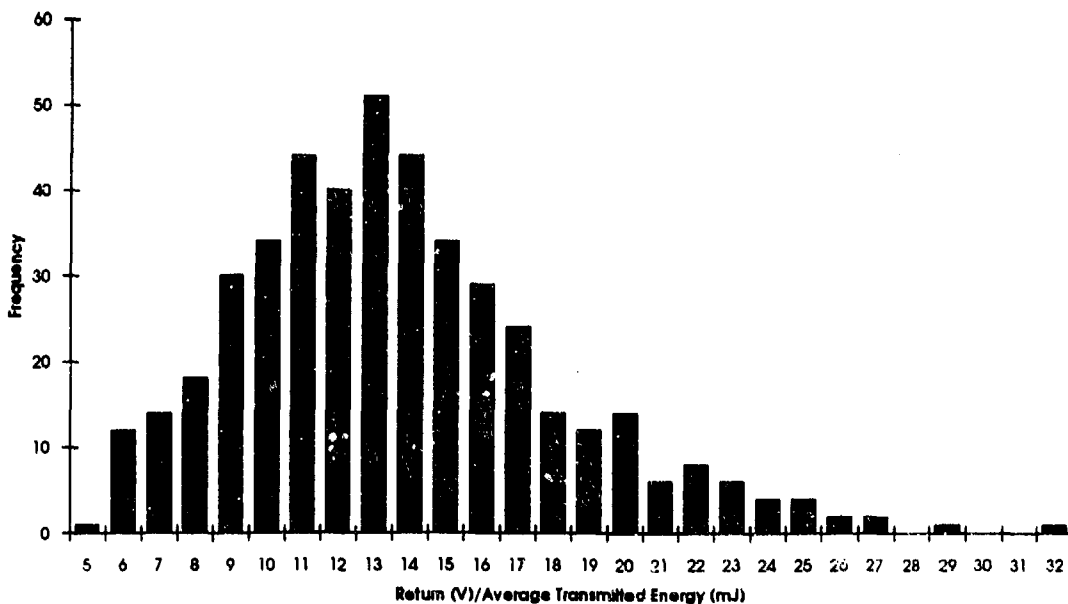


Figure 29: Incoherent detection with the Lambertian (speckle) target. This data was taken on April 12, 1993.

The targets used in this case were the Lambertian target and the flame sprayed aluminum target. Figure 29 is a histogram of the returns from the Lambertian target. Before a probability density function is plotted on top of this histogram the physical meaning of the histogram needs to be understood. The height of each bin, once normalized to the total number of returns measured, represents the probability of the return falling in that bin. The theoretical distributions discussed earlier were probability density functions. In order to get a theoretical value for the probability, the probability density function has to be integrated over the range that represents the bin. Once integrated the value remaining for each bin is the probability of that return occurring.

The general procedure used to fit the theory to the data for all four cases is as follows:

1. The mean and the variance of the experimental data is calculated.
2. A general form of the theoretical distribution is found that is a function of the mean and/or the variance.

3. The equations for the mean and variance are found in terms of the variable in the general theoretical distributions.
4. The mean and variance of the data is used in the equations for the mean and variance to solve simultaneously for the variables in the theoretical distributions.
5. Using the solutions found in step 4 the general theoretical distributions are integrated over each bin of the histogram and plotted versus the return.

The above steps were used for each detection scheme for each type of target and are shown in the following pages.

The probability density function which represents the fluctuation in the detector current for incoherent detection with a speckle target is given in Eq. (3.3.10) as [15]

$$p_{IS}(k) = \int_0^{\infty} \frac{1}{\sqrt{2\pi(\langle n \rangle + bW)}} \exp\left[-\frac{(k - (\langle n \rangle + bW))^2}{2(\langle n \rangle + bW)}\right] \frac{a^M W^{M-1} \exp(-aW)}{\Gamma(M)} dW. \quad (7.2.2)$$

This equation is known as a negative binomial distribution. Fortunately the integral has been simplified to a discrete form as shown below [15]

$$p_{IS}(k) = \frac{\Gamma(k+M)}{\Gamma(k+1)\Gamma(M)} \left[1 + \frac{\langle N_s \rangle}{M}\right]^{-M} \left[1 + \frac{M}{\langle N_s \rangle}\right]^{-k} \quad (7.2.3)$$

where $\langle N_s \rangle$ is the average signal, M is the number of speckle lobes seen by the receiver and Γ represents the gamma function. Before this equation can be used to curve fit, expressions are needed for the mean and the variance of the equation. These were not given by Goodman [15] so they must be derived as follows.

A general form of a negative binomial distribution is [29]

$$b_{neg}(w-1; x-1, \theta) = \binom{x-1}{w-1} \theta^{w-1} (1-\theta)^{x-w} \quad (7.2.4)$$

where the first expression is the binomial coefficient which is defined as

$$\binom{x}{w} = \frac{x!}{w!(x-w)!}. \quad (7.2.5)$$

The mean is

$$\mu = \frac{w}{\theta} \quad (7.2.6)$$

and the variance is

$$\sigma^2 = \frac{w}{\theta} \left(\frac{1}{\theta} - 1 \right). \quad (7.2.7)$$

Starting with the binomial coefficient in Eq. (7.2.3), Eq. (7.2.3) was put in to the general form expressed in Eq. (7.2.4). Through simple mathematical manipulations, θ was found to be $(N_s)/(M + (N_s))$.

Knowing the mean, m , and the variance, σ_β^2 , of the data, Eq. (7.2.6) and (7.2.7) can be solved for w and θ . The variance was calculated using

$$\sigma_\beta^2 = \frac{\sum_{j=1}^n (i_j - m)^2}{n-1} \quad (7.2.8)$$

where m is the mean and i_n is the n^{th} peak in a data set. Once w and θ are known Eq. (7.2.4) can be summed over each bin of Fig. 29 to find the theoretical probability. A quick way to find the area under a function $f(x)$ between x_1 and x_2 is to perform calculation $\text{Area} = 0.5(x_2-x_1)[f(x_2)+f(x_1)]$. The theoretical probabilities are plotted in Fig. 30 as dots and the curve plotted helps to visualize how a continuous probability function would fit the data. The chi² test was 16.25 for 24 degrees of freedom. This is less than the required 33.2 needed for 90% agreement. This would then be considered a good fit to theory. There are only 449 data points in this data set which may not be a very good statistical sample. To increase the number of data points two sets of data were taken consecutively. The combined set of data is shown in Fig. 31 along with the theoretical probability

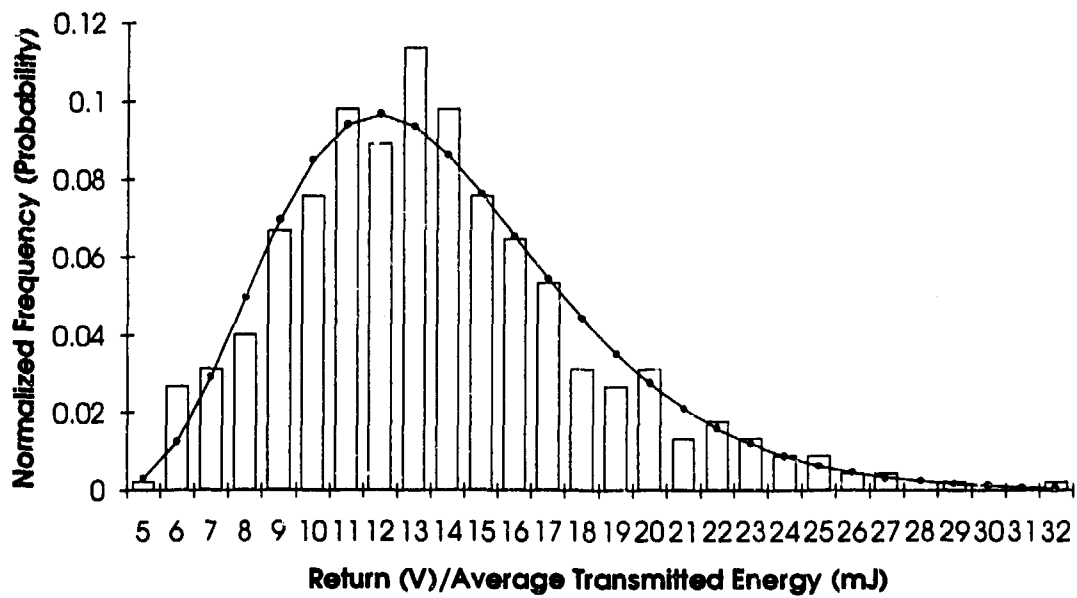


Figure 30: Theoretical fit to data taken using incoherent detection with the lambertian (speckle) target on April 12, 1993. There are 449 data points in this figure.

function. This fit has a χ^2 of 13.6 with 24 degrees of freedom. This is in excellent agreement with theory. By comparison, Fig. 32 shows similar data taken from the flame sprayed aluminum target. The χ^2 value for this case was 32.6 with 30 degrees of freedom which is a marginally good fit to theory. Another example of data collected from the lambertian target is shown in Fig. 33. The χ^2 statistic was 25.7 with 25 degrees of freedom, which gives a reasonably good fit to theory.

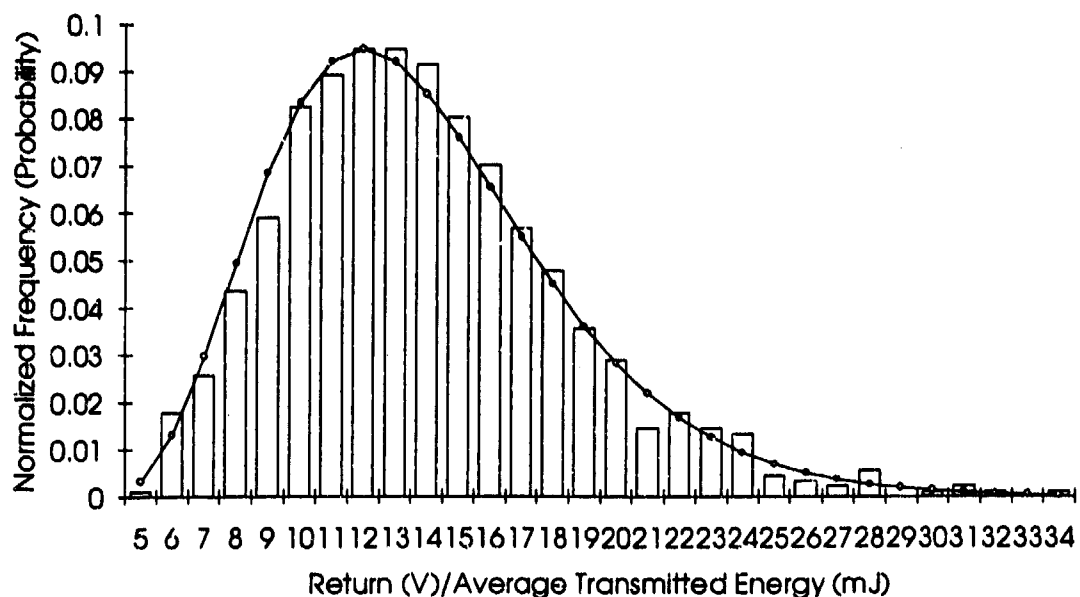


Figure 31: Theoretical fit to data taken using incoherent detection with the lambertian (speckle) target on April 12, 1993. There are 898 data points in this figure.

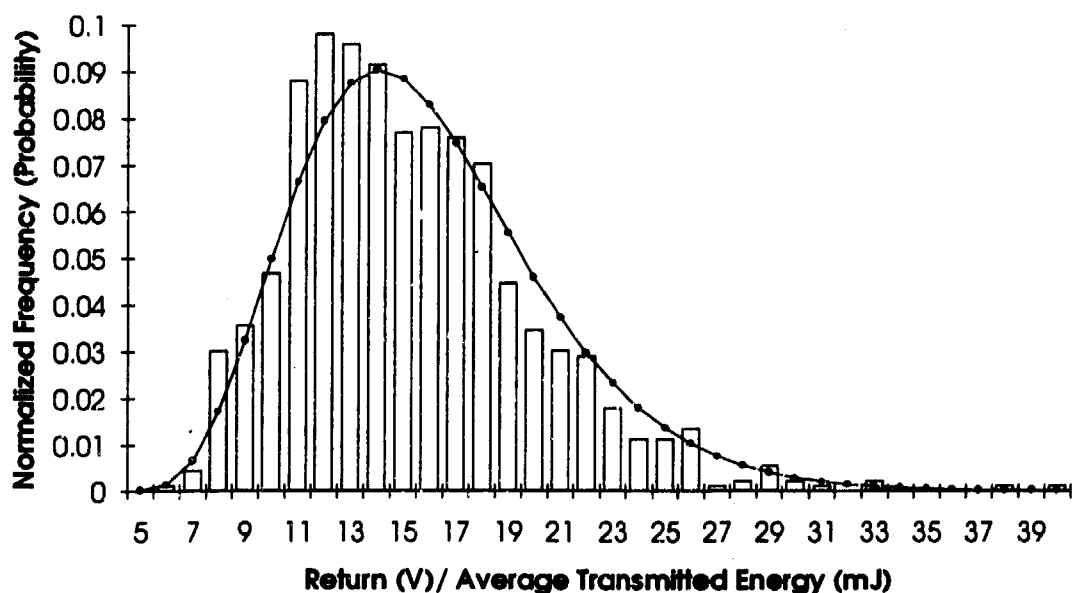


Figure 32: Theoretical fit to data taken using incoherent detection with flame sprayed aluminum target on April 8, 1993. There are 898 data points in this figure.

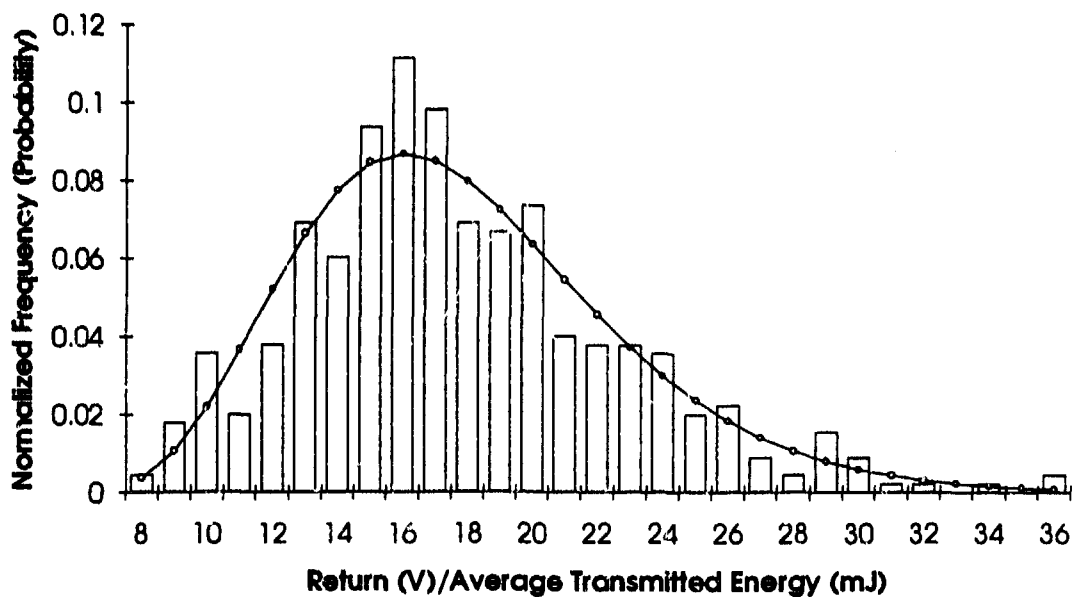


Figure 33: Theoretical fit to data taken using incoherent detection with the lambertian target on April 15, 1993. There are 449 data points in this figure.

7.2.4 Analysis of Incoherent Detection with a Glint Target

For a glint target a 2" corner cube reflector was first used. The data taken using the corner cube reflector seem to be weighted to the side of a smaller return as can be seen in Fig. 34. This behavior was noticed for a glint target for both detection techniques. The explanation for these results is relatively simple when considering the circumstances. The temperature difference between room temperature and the outside temperature was at least 20°F and the porthole to the outside was open allowing the air in the building to rush out and mix with the cold air right outside the porthole. This would give a large amount of refractive turbulence at the aperture of the transmitted beam. The effect of the refractive turbulence at the transmitting aperture would cause the beam to wander on and off the 2" corner cube reflector causing there to be a smaller return most of the time

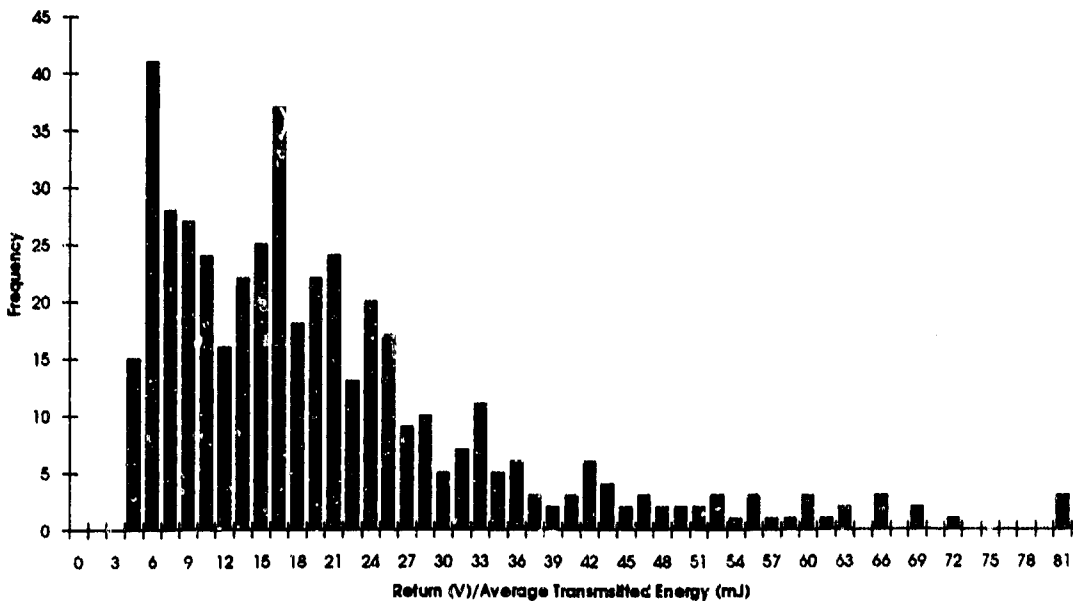


Figure 34: Data taken using incoherent detection with the corner cube reflector.

because only part of the beam was striking the target. This would give a large number of small returns as seen in Fig. 34.

To correct this problem 65 bicycle reflectors were purchased and tiled in a 2' by 2' square on a piece of plywood and this was used to produce a glint return. An example of the distribution of the fluctuation in the return with this new target is shown in Fig. 35. This set of data was taken on April 7, 1993.

The theoretical probability density function for incoherent detection with a glint target was given in general form in Eq. (3.3.2) as [2,12,15]

$$p_{IG}(x) = \frac{1}{\sqrt{2\pi}\sigma^2} \exp\left(-\frac{(x-m)^2}{2\sigma^2}\right) \quad (7.2.9)$$

where m is the mean of the data and σ^2 is the variance of the data. This Gaussian PDF can now be integrated over each individual bin, which is reasonably easy because the integral can be reduced to an expression involving the error function as shown below.

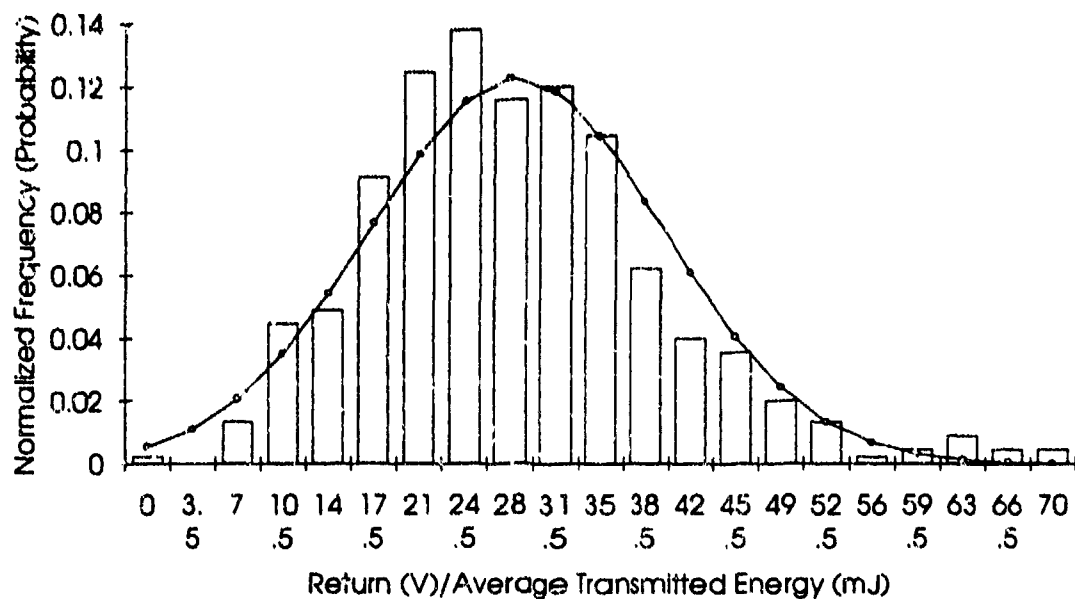


Figure 35: Incoherent detection with the bicycle reflector (glint) target. This data was taken on April 7, 1993 at 9:20am. There are 449 data points.

$$P_{IG\ Bin} = 0.5 ERF\left(\frac{x_2 - m}{\sqrt{2}\sigma^2}\right) - 0.5 ERF\left(\frac{x_1 - m}{\sqrt{2}\sigma^2}\right) \quad (7.2.10)$$

This was graphed for the mean and variance of the experimental data and the resulting curve can be seen in Fig. 35.

This is the only set of data for this case that the theory actually fit. One problem that was unresolvable was that none of the data sets include more than 449 data points. There were several attempts at combining consecutive data sets but the means of each data set were different enough that the data sets could not be combined. Even though a larger "glint" target was being used the same trend of having an uneven distribution weighted to the smaller returns end of the graph is seen throughout the data sets. Some examples are seen in Fig. 36 and 37.

One observation about the data is that the distribution of the actual data is narrower than the plotted theoretical distribution. This is understandable since the data

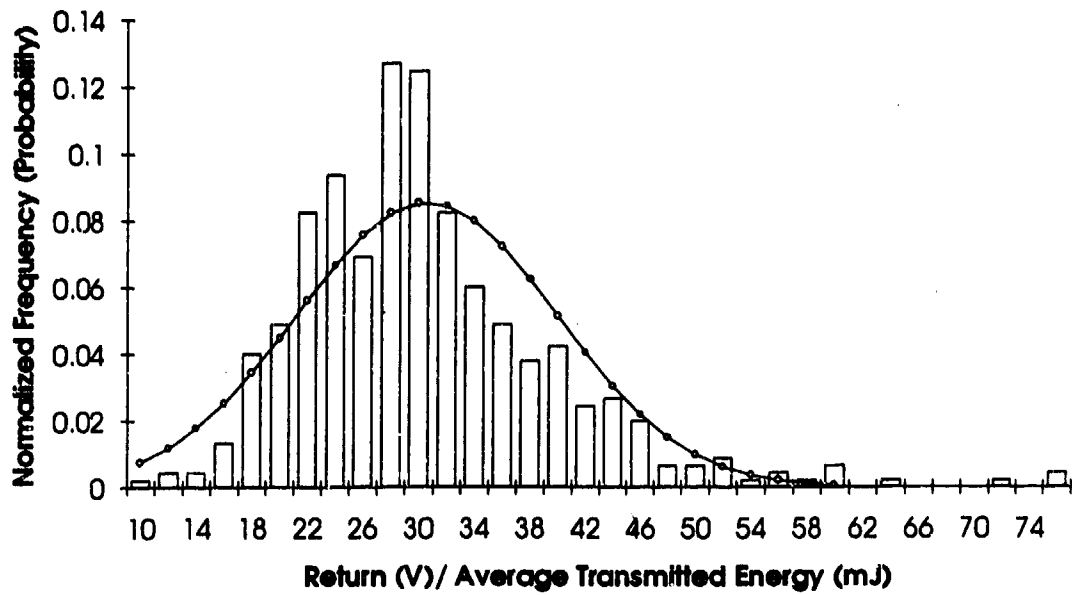


Figure 36: Incoherent detection with the bicycle reflector (glint) target. This data was taken on April 7, 1993.

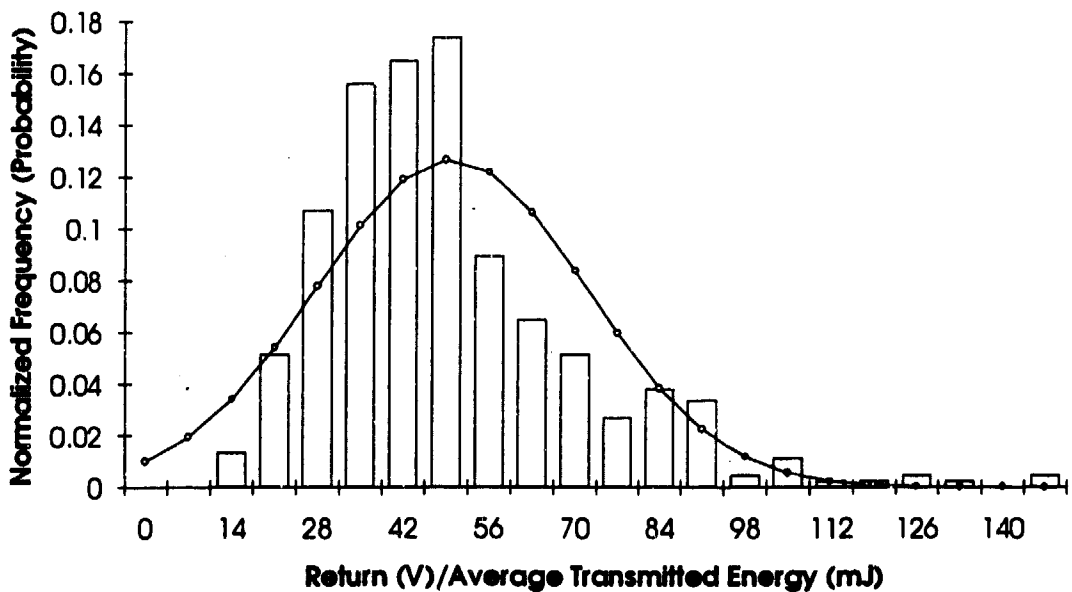


Figure 37: Incoherent detection with the bicycle reflector (glint) target. This data was taken on April 22, 1993.

was taken in a staring mode, and had everything been perfect there would be a constant return from the glint target. But due to turbulence the beam will wander some on the target giving some variance from the mean return signal. If the data was taken in a scanning mode spatial averaging caused by the scanning would broaden the distribution [30]. One other possible explanation for the theory not fitting the data is the target used. It is possible that bicycle reflectors do not give the same statistics as does a cornercube reflector for glint target returns.

7.2.5 Analysis of Coherent Detection with a Speckle Target

Data was collected for coherent detection with both the lambertian and the flame sprayed aluminum targets. Both should exhibit diffuse characteristics. Shown in Figs. 38 and 39 are data sets taken from the lambertian target. Figure 38 shows a histogram of data taken on April 1, 1993. This is a combination of two data sets that had the same mean and similar variances giving 910 data points.

The probability density function representing the fluctuation in the current in the detection circuit electronics is a Rayleigh PDF (Eq. (3.3.12)) as

$$p_{cs}(i) = \frac{2i}{\langle i_{Coh,SN}^2 \rangle + \langle i_{Diffuse}^2 \rangle} \exp\left(-\frac{i^2}{\langle i_{Coh,SN}^2 \rangle + \langle i_{Diffuse}^2 \rangle}\right) \quad (7.2.11)$$

This equation has the general form of [28]

$$p_{cs}(\beta) = \frac{\beta}{\alpha^2} e^{-\beta^2/2\alpha^2} \quad (7.2.12)$$

where $\alpha^2 = \sigma_\beta^2 / (2 - \frac{1}{2})$ and σ_β^2 is the variance of the data. Once the variance of the data is known, Eq. (7.2.12) can be integrated from bin to bin (x_1 to x_2) to find the probability function representing the fluctuation in the return. The result of this integration is

$$P_{CS\,Bin} = e^{-\left(\frac{x^2}{2\sigma^2}\right)} - e^{-\left(\frac{(x')^2}{2\sigma^2}\right)} \quad (7.2.13)$$

The chi² statistic for this fit is 48.7 with 27 degrees of freedom. This is not an acceptable fit even though it, at first glance, would seem to be a good fit. Shown in Fig. 39 is another set of data taken on April 12, 1993 with the lambertian target. The chi² statistic for this fit is 450 which shows that this is not a good fit. These two figures are a good representation of all the speckle data taken.

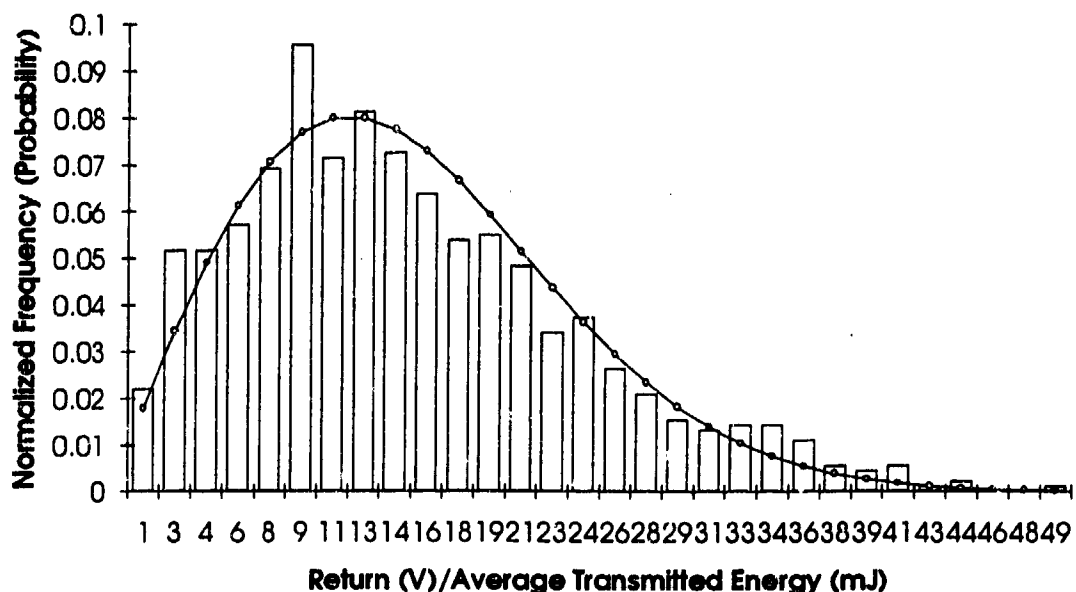


Figure 38: Coherent detection with the lambertian target taken on April 1, 1993. Shown is the best fit Rayleigh distribution with a chi² of 48.7 with 27 degrees of freedom. (Needs to be less than 36.7).

One explanation for the deviation from theory that has already been mentioned in the previous section is the effects of turbulence. With the temperature difference between outside and inside the tower the turbulence right outside the porthole has a large effect. Some work has been done by Jeffrey Shapiro, Sun T. Lau and David M. Papurt [30,31] to describe the effects of turbulence on target returns and on target statistics. In their work

[31] they give the probability density functions for both a glint and a speckle target including the effects of turbulence using log-normal distributions which are functions of σ

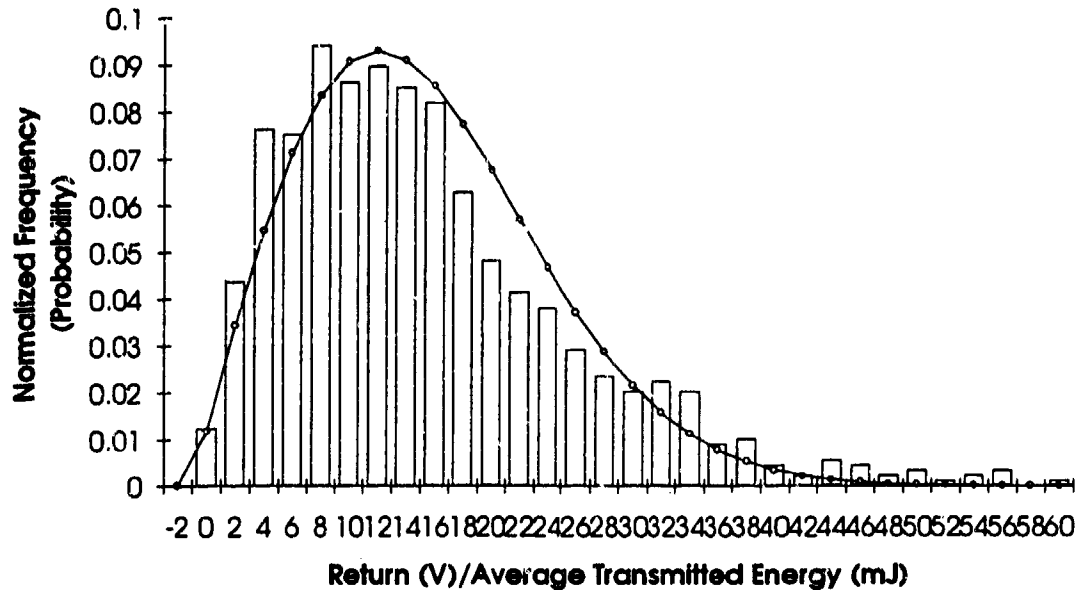


Figure 39: Coherent detection with the lambertian target taken on April 12, 1993. There are 898 data points. This is the best fit Rayleigh probability distribution which gives a $\chi^2=450$.

which is used as a turbulence factor that ranges from 0 (no turbulence) to 0.5 (saturated scintillation). In this work they also give the cumulative probability distribution function for each case. The cumulative probability distribution for a speckle target is given as

$$P_x(X) = 1 - Fr[X \exp(4\sigma^2), 0; \sigma]; X \geq 0 \quad (7.2.14)$$

where the log-normal-density frustration function, $Fr//$, is given as

$$Fr(a, 0; c) = \int_{-\infty}^{\infty} dt (2\pi c^2)^{-\frac{1}{2}} \exp\left[-\frac{(t+c^2)^2}{2c^2}\right] \exp(-ae^{2t}) \quad (7.2.15)$$

and

$$x = \frac{i^2}{\langle i^2 \rangle} \quad (7.2.16)$$

where i is the return signal current and $\langle i^2 \rangle$ is the mean of the square of the return signal.

Since the cumulative probability distribution is the integration from negative infinity to x the equation can be used to find the probability of that return occurring for each bin. The calculation of the frustration function was performed using a macro in Microsoft Excel. This analysis was done for the collected data and the difference this makes can be seen in Figs. 40 and 41 which are the same data sets as seen in Figs. 38 and 39 but with different theoretical fits. In Fig. 40 the χ^2 statistic was 22.5 with 27 degrees of freedom which gives very good agreement with theory.

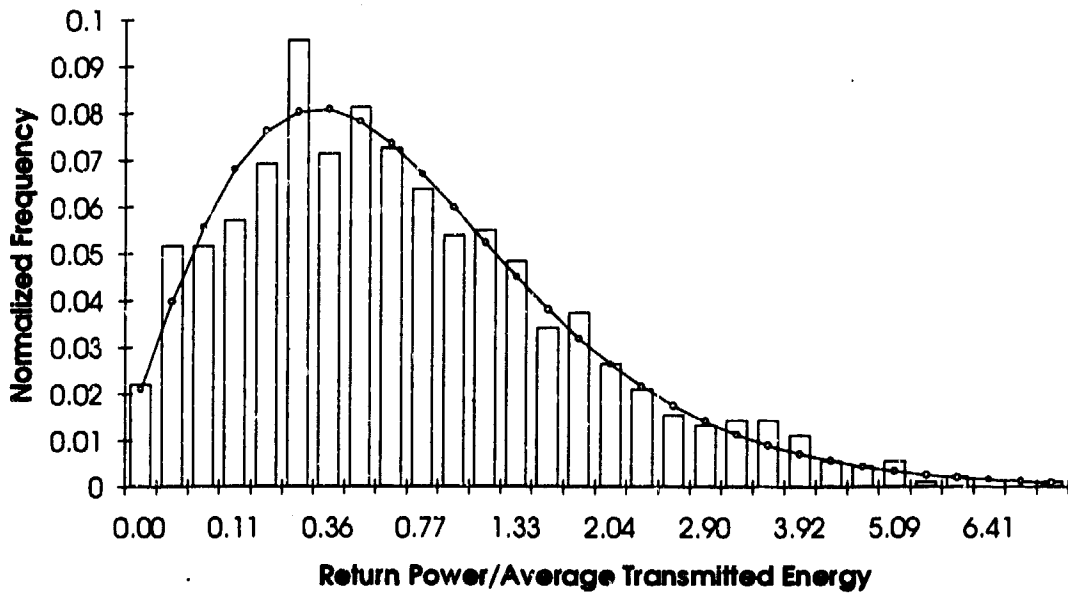


Figure 40: Data taken April 1, 1993 with log-normal distribution used as best fit curve, $\sigma = 0.05$, $\chi^2=22.5$ with 27 degrees of freedom.

Figure 41 shows the data taken on April 12 with the best fit log-normal distribution. The χ^2 statistic was 19.2 with 29 degrees of freedom which is excellent agreement with theory.

7.2.6 Analysis of Coherent Detection with a Glint Target

For this case the data was collected from the target composed of the bicycle reflectors. The probability density function representing the fluctuation in the output current of the detector electronics is represented by a Rician PDF. A general form of the Rician density is given as [2]

$$p_{CG}(i) = \frac{i}{\sigma^2} \exp\left(-\frac{i^2 + i_{Glint}^2}{2\sigma^2}\right) I_0\left(\frac{ii_{Glint}}{\sigma^2}\right) \quad (7.2.17)$$

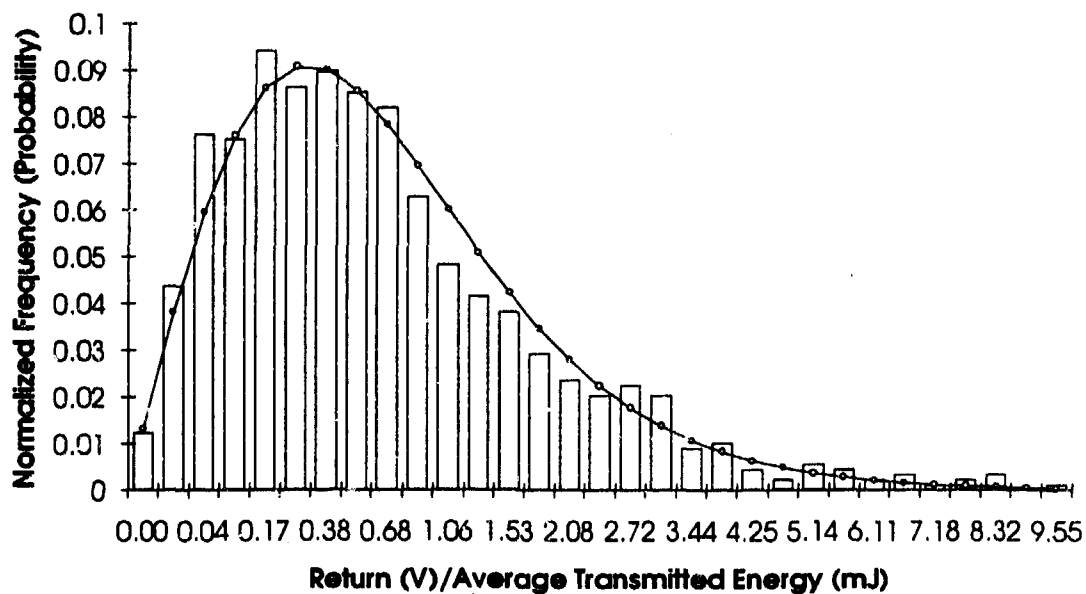


Figure 41: Data taken April 12, 1993, with best fit log-normal, $\sigma=0.055$, $\chi^2=19.2$ with 29 degrees of freedom.

where σ^2 is the variance, which is related to the variance of the data (σ_{Exp}^2), represented by [32]

$$\sigma_{Exp}^2 = 2\sigma^2 + i_{Glint}^2 \quad (7.2.16)$$

and the mean is

$$m = \sqrt{\frac{\pi}{2}} \sigma e^{-\frac{i^2}{4}} \left[\left(1 + \frac{g^2}{2} \right) I_0 \left(\frac{g^2}{4} \right) + \frac{g^2}{2} I_1 \left(\frac{g^2}{4} \right) \right] \quad (7.2.17)$$

where g is $i_{G\text{lint}}/\sigma$.

To plot the theoretical curves with the collected data the mean and the variance of the data will be used in conjunction with Eqs. (7.2.16) and (7.2.17) to give two equations with two unknowns (i.e., $i_{G\text{lint}}$ and σ). Once the values for these variables are found they can be substituted into Eq. (7.2.15) and this equation can be integrated over each bin to give the probability of that return occurring. For the data collected, complex numbers were calculated in the process of trying to solve Eqs. (7.2.16) and Eq. (7.2.17), which suggests that the Rician distribution will not fit the data. Some examples of the data collected are shown in Figs. 42-44. The histograms of the data look similar which suggests that the same problem exists for all the data sets. An explanation for the deviation from the theory is refractive turbulence.

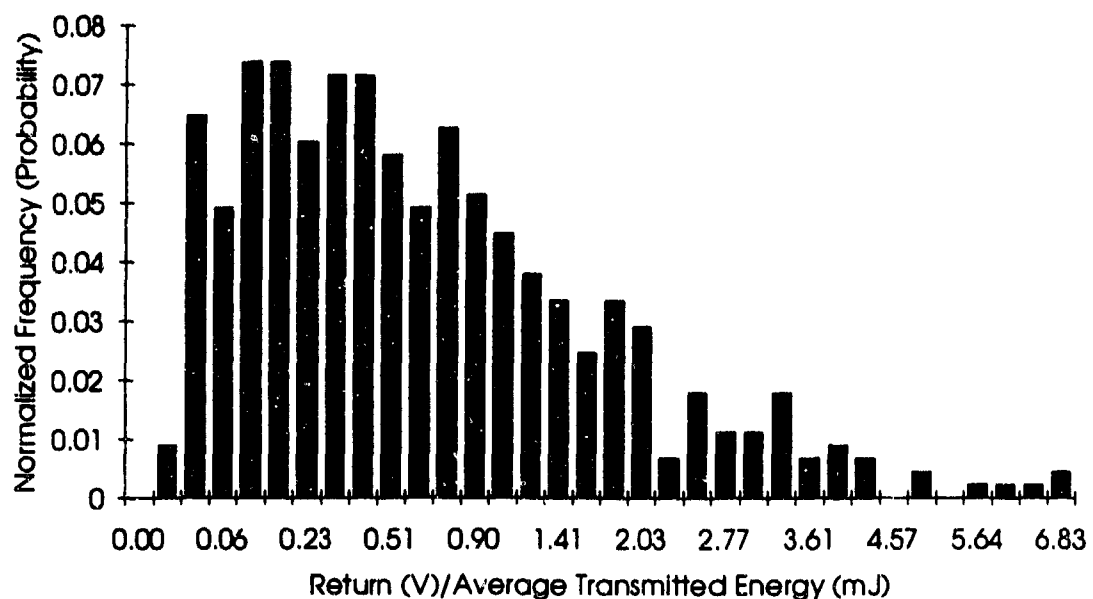
In the previous section refractive turbulence was shown to have an effect on the probability distribution of the return data. In Shapiro and Lau's paper [29] they give an equation that represents the cumulative probability function for the fluctuation of the return signal for coherent glint target detection with atmospheric turbulence which is expressed as

$$P_{CG}(X) = 1 - Q \left[\left(\frac{\ln X}{4} + 2\sigma^2 \right) / \sigma \right] \quad (7.2.18)$$

where

$$Q(t) = \int_t^\infty \frac{1}{\sqrt{2\pi}} \exp \left(-\frac{\tau^2}{2} \right) d\tau, \quad (7.2.19)$$

$$x = \frac{i^2}{\langle i^2 \rangle}, \quad (7.2.20)$$



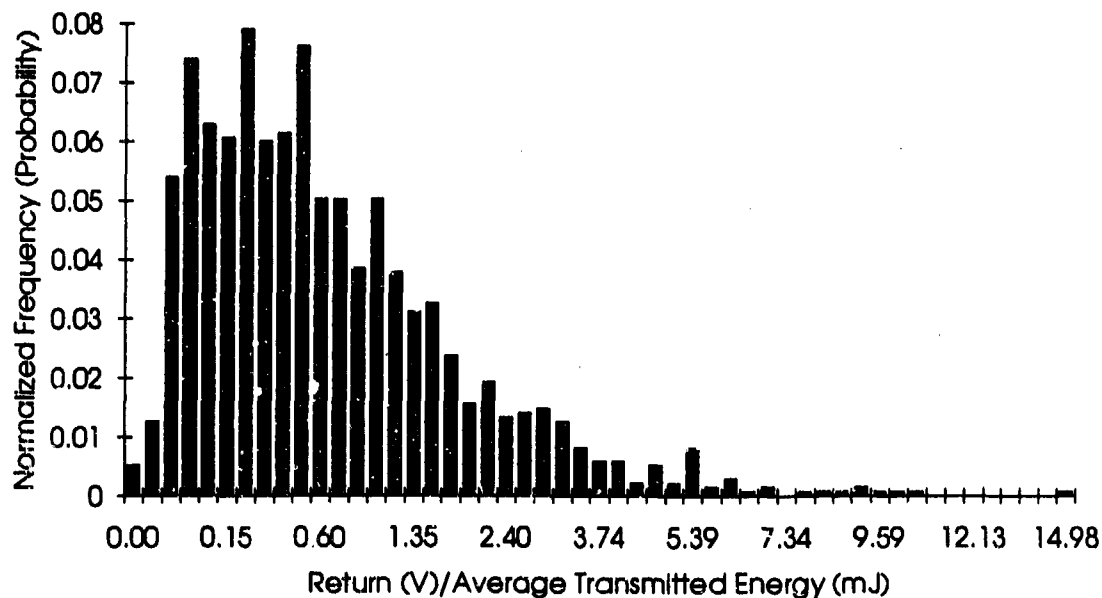


Figure 44: Data taken with a glint target on April 8, 1993. There are 1353 data points in this histogram.

i is the return signal current, $\langle i^2 \rangle$ is the mean square return signal and σ is the turbulence factor. Since Eq. (7.2.18) is a cumulative distribution it can be used to find the theoretical value of the probability over each bin. This looks and sounds complicated but it is relatively easy since the $Q(t)$ function is in the form of the error function (ERF). The expression used to find the probability over each bin (with boundaries x_1 and x_2) is shown below.

$$P_{CG\text{Bin}}(X) = 0.5 \left[ERF\left(\frac{\ln(x_2)}{\sqrt{2\sigma^2}} + 2\sigma^2\right) - ERF\left(\frac{\ln(x_1)}{\sqrt{2\sigma^2}} + 2\sigma^2\right) \right] \quad (7.2.21)$$

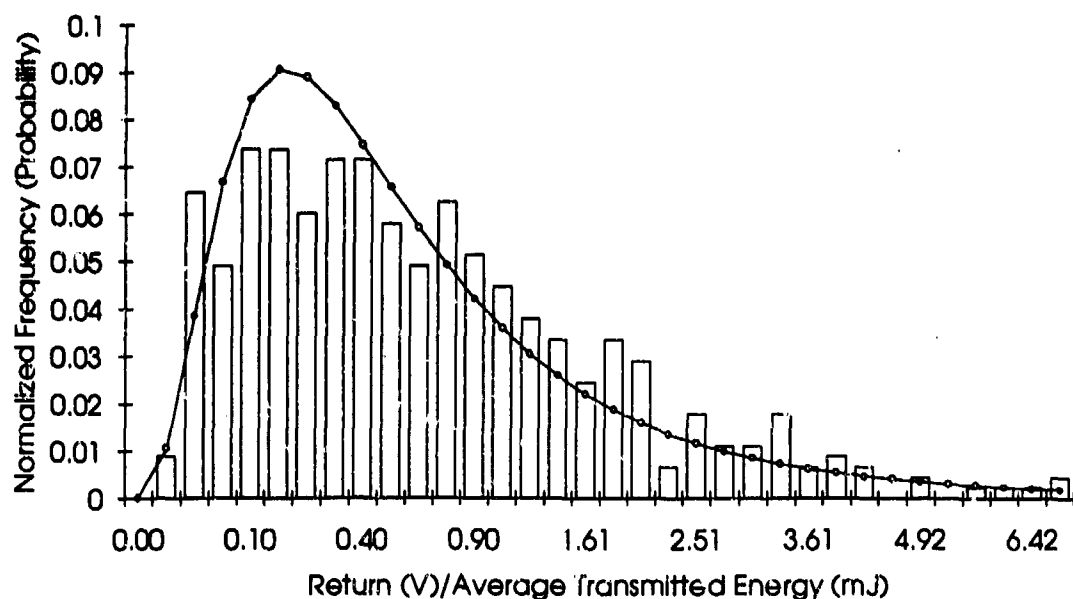


Figure 45: Theoretical probability distribution for coherent detection with a glint target for data taken on April 5. $\text{Chi}^2=37.0$ with 30 degrees of freedom; good fit to data.

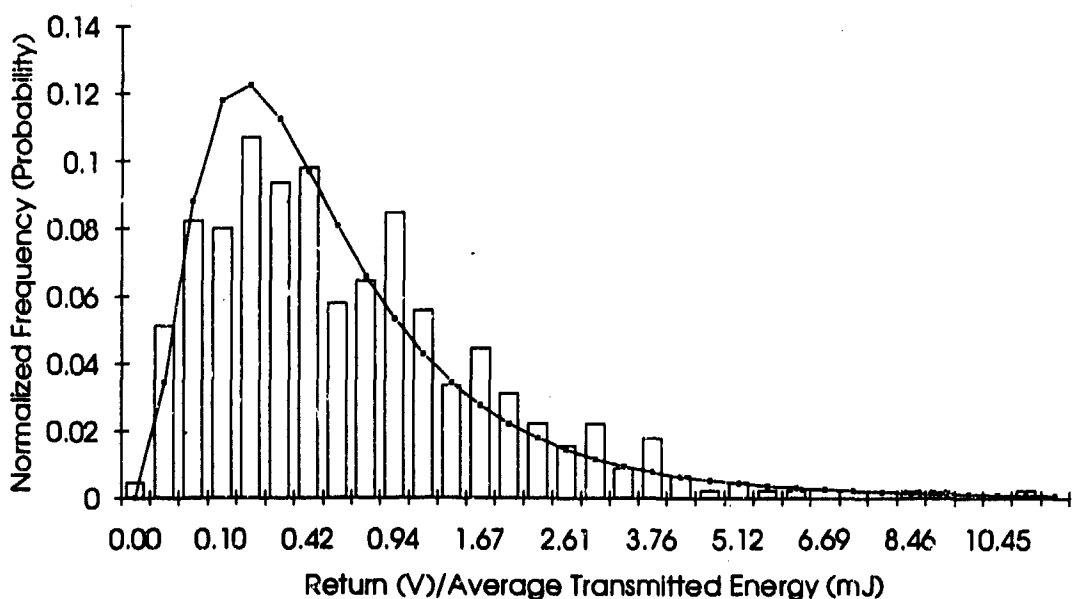


Figure 46: Theoretical probability distribution for coherent detection with a glint target for data taken on April 7. $\text{Chi}^2=41.8$ with 29 degrees of freedom; this is a poor fit to theory.

Equation (7.2.21) was plotted for the data sets shown in Figs. 42-44. Shown in Fig. 45 is the data taken on April 5th with equation (7.2.21) plotted with a $\sigma=0.0992$ which gives a χ^2 of 37.0 with 30 degrees of freedom. This is a good fit to the theory. In Fig. 46, the best fit curve gave a $\sigma=0.1$, $\chi^2 = 41.8$ with 29 degrees of freedom. This is a poor fit to the theory. Figure 47 is a combination of three data sets (1353 data points) taken on April 8th. The turbulence factor for the best fit was found to be 0.104, which gave a $\chi^2 = 76$ with 49 degrees of freedom. This is also a poor fit to theory.

These graphs demonstrate that turbulence is a factor that is contributing to the shape of the probability curves. The theory that Shapiro and Lau demonstrated was demonstrated for a 10.6 μm lidar system. Since we are working at 2.09 μm the turbulence effects are 5 times greater. Another factor that may effect the shape of the distribution is if the bicycle reflectors do not make a good glint target.

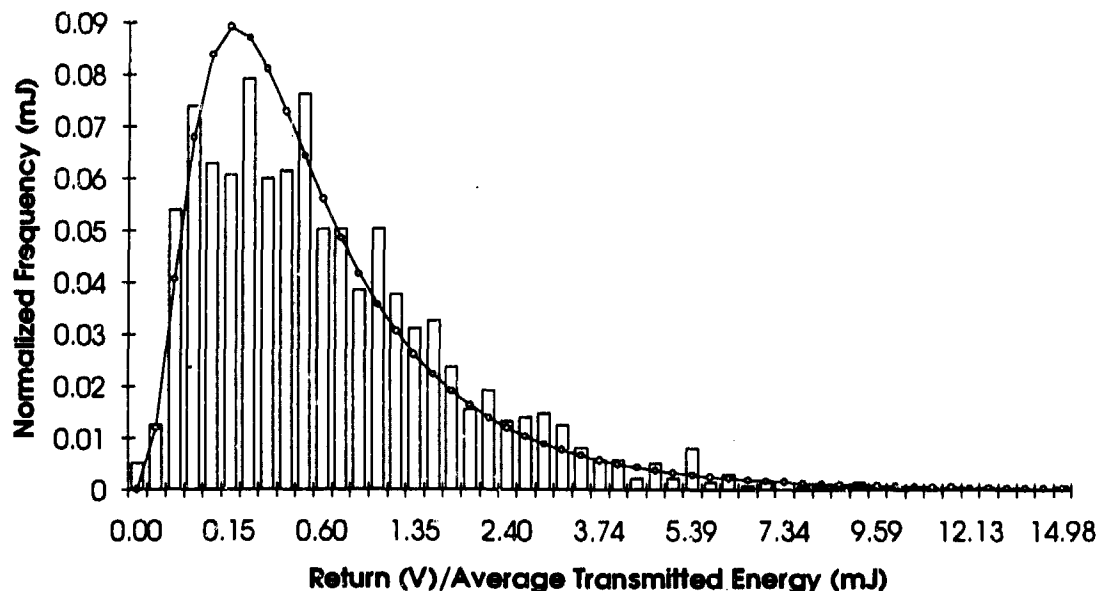


Figure 47: Coherent detection data taken from a glint target on April 8th. The theoretical fit gives a $\chi^2=76$ with 49 degrees of freedom. This is a poor fit to the experimental data.

7.2.7 Analysis of the Probability of Detection

To verify the probability of detection, data was taken of just the noise present in the system. The data sets contained 898 data points each and there were 6 different sets of data taken. With each noise data set a threshold was chosen to give a particular probability of false alarm. For example, one sample of noise may have values of 2, 5, 7, 4, and 9. If a threshold of 8 is chosen the probability of false alarm would be 0.2 (1/5) since there is one value of noise greater than the threshold for the 5 pieces of data.

Now that a threshold is set the data taken is compared to that threshold. The number of data points greater than the threshold are counted and that number is divided by the number of data points taken. This will give the probability of detection. Since the probability of false alarm is known the amount of noise and signal is also known so the average signal-to-noise ratio can be calculated and then the calculated probability of detection can be compared to the theory for that false alarm rate and that SNR. Because of time constraints on use of the experimental equipment and ranges, not enough data was taken to verify the probability of detection for the glint targets, but sufficient data was taken to verify the probabilities of detection for a speckle target.

For coherent detection with a speckle target the results of the measurements taken are shown in Table 7 for a probability of false alarm of 10^{-2} .

Table 7:
Comparison of calculated and measured probabilities of detection for coherent detection with a speckle target.

SNR (dB)	Probability of Detection Measured	Probability of Detection Predicted
30.33	0.9978	0.9958
30.63	0.9955	0.996
29.68	0.9978	0.995

For incoherent detection with a speckle target the results of the measurements taken are shown in Table 8 also for a probability of false alarm of 10^{-2} .

Table 8:
Comparison of calculated and measured probabilities of detection for incoherent detection with a speckle target.

SNR (dB)	Probability of Detection Measured	Probability of Detection Predicted
18.81	0.9978	0.970
21.41	0.9911	0.989
20.53	0.9978	0.985
22.23	0.9978	0.992
21.75	0.9978	0.991

The limited amount of data available for both coherent and incoherent detection schemes seem to demonstrate a rather close comparison between the theory and the data.

CHAPTER VIII

8.0 CONCLUSIONS AND RECOMMENDATIONS

The basis used to compare coherent to incoherent detection for a solid state 2.09 μm LADAR system was the probability of detection. In order to find the probability of detection the dominating noises in the LADAR system had to be determined. It was determined that signal shot noise was the primary noise source for incoherent detection and for coherent detection the dominating noise was found to be thermal noise. Since the desire for an optimized coherent detection scheme is to have the system shot noise limited, the amount of LO power incident on the detector was increased until the shot noise dominated the thermal noise in the system. Knowing the dominating noise source for each detection scheme the threshold currents for selected probabilities of false alarm were determined. Using the threshold currents calculated, the probabilities of detection for each detection scheme were plotted for different probabilities of false alarm.

To calculate the probabilities of detection for both detection schemes for both glint and speckle targets the corresponding probability density functions (PDF's) representing the fluctuation in the current from the detector were identified. To verify that these PDF's were accurate, data was collected of the fluctuation in the detection circuit electronics from pulse to pulse. An attempt was then made to fit the predicted theory to the experimental results.

For incoherent detection with a speckle target the theoretical probability distribution used to find the probability of detection fit well with the experimental data.

This confirmed that the negative binomial distribution was the correct distribution to represent the statistics of the return for a speckle target for incoherent detection.

When using a glint target with incoherent detection the results were not as good. There was one data set that fit the theory according to the χ^2 statistic. The rest of the data gave distributions that were narrower than the theoretical distributions that were supposed to fit that data. An explanation for this discrepancy involves the method used to collect the data. The data was collected in a staring mode so if there were no other effects to degrade the return (turbulence, vibrations, etc.) the return would be a constant value from pulse to pulse. Since the world is not perfect those effects are present so there is variation in the return, but the return is not entirely random because the beam is still striking the same general location on the target. This is seen by looking at the data collected and noticing that the distribution of the experimental data is narrower than the theoretical distribution. One recommendation to solve this problem is to scan the beam over an area that includes the target and then take the value that represents the largest return from that frame. This would give a more random sample.

For coherent detection with a speckle target the data did not fit the Rayleigh distribution as predicted by the theory. Under the conditions which data was taken the suspected problem is turbulence. The temperature difference between outside and inside the test tower was at least 20°F. The porthole used to direct the beam outside was not covered so the air in the building was rushing out of the room and mixing with the outside air immediately outside. This would give a good deal of refractive turbulence right outside the porthole. Turbulence at the transmit aperture is the worst place to have turbulence in a radar situation. Work done by J.H. Shapiro, and S.T. Lau. [31] involved describing the effects of turbulence on the statistics of target returns. They gave two probability density functions that represent the fluctuation in the return for a glint and a speckle target which included a term representing the turbulence in the system. The

equation for a speckle target was plotted using the data collected and there was a very good fit to the theory.

For a glint target when using coherent detection the fluctuation in the return should be a Rician distribution. In order to plot the theoretical curve to the experimental data two equations with two unknowns have to be solved to find the parameters to graph the equation. With the collected data the result was always complex which showed that the theory did not fit to the data. Again it was assumed that the reason was turbulence. Using the probability density function given by J.H. Shapiro, and S.T. Lau. [31] which included terms representing the turbulence, a couple sets of data were found to fit to that theory, but not very well. Shapiro and Lau demonstrated for a staring system that the statistics would not fit the theoretical distribution and to get the theoretical statistics a scanning system is required.

Using the LADAR system a couple points on the probability of detection curves for speckle targets for coherent and incoherent detection were verified. Because of the lack of time data for the glint target case is not available.

A few suggestions for future work are: first of all, data needs to be taken in a scanning mode which would allow a more random sample of target returns and this would give a better representation of the statistics of interest. A second suggestion is to take the data with something, a piece of glass or plastic, over the porthole decreasing the effects of turbulence at the transmitting aperture or even opening the entire room to the outside. The third suggestion is to work with the statistics involved for incoherent detection when the system is not signal shot noise limited and see how the detection techniques compare. The fourth suggestion is to have a better method of collecting the data. The method used was the best available with the time and equipment available. Before the current system can be used for further work, some experimental work needs to be done to determine why

the system is losing efficiency and not transmitting as much energy as before. There also
seems to be improvements in the consistency of the injection seeding of the slave cavity.

8.1 LIST OF ORIGINAL CONTRIBUTIONS

- First to investigate detection statistics with a coherent solid state laser radar system.
- First to investigate detection statistics at 2 μm .
- First to compare coherent detection to incoherent detection at 2 μm .

APPENDIX A

An Understanding of Shot Noise Using Poisson Statistics

Shot noise is caused by fluctuation in the current due to the discrete nature in which charge carriers are produced. To discuss this fluctuation there are a few assumptions that have to be made. With those assumptions a brief description of the process that occurs during detection is given and it is described using a Poisson probability distribution. It is then shown that the mean squared fluctuation of a Poisson probability distribution is equal to the mean. This result is related to current from our ideal detector and the result is an expression for the mean squared fluctuation in the current due to the detection process alone.

An ideal photon detector is assumed. This ideal photon detector has no leakage current when there is no light incident upon it. The beam incident on the detector is assumed noiseless, single frequency, and of a constant power. This would lead to the thought that the output current would also be constant, though, this is not the case. The depth at which the photons travel into the detector before they are absorbed and produce the emission of an electron is discrete and random which means that the emission of the electrons is also a random discrete process. A random discrete process can be described by a Poisson probability distribution as [32]

$$P(n) = \frac{\langle n \rangle^n}{n!} e^{-\langle n \rangle}, \quad (\text{A.1})$$

where $P(n)$ is the probability that n photons will be detected in a sample time τ , and $\langle n \rangle$ is the average number of photon events occurring in time τ .

The definition of noise is the mean squared fluctuation, or the variance. The variance can be calculated by [12]

$$\sigma^2 = \langle (n - \langle n \rangle)^2 \rangle, \quad (\text{A.2})$$

which can be simplified to [32]

$$\begin{aligned} \sigma^2 &= \langle (n - \langle n \rangle)^2 \rangle = \langle n^2 - 2n\langle n \rangle + \langle n \rangle^2 \rangle \\ &= \langle n^2 \rangle - \langle 2n\langle n \rangle \rangle + \langle \langle n \rangle^2 \rangle \\ &= \langle n^2 \rangle - \langle 2\langle n \rangle^2 \rangle + \langle \langle n \rangle^2 \rangle \\ &= \langle n^2 \rangle - \langle n \rangle^2 \end{aligned} \quad (\text{A.3})$$

This result can now be used to show that the variance of a Poisson distribution is equal to the mean. To begin, a simple mathematical identity is used.

$$n^2 = n + n(n-1) \quad (\text{A.4})$$

The mean of Eq (A.4) is

$$\begin{aligned} \langle n^2 \rangle &= \langle n + n(n-1) \rangle \\ &= \langle n \rangle + \langle n(n-1) \rangle. \end{aligned} \quad (\text{A.5})$$

For the second term of that result, the following statistical definition can be substituted [32]

$$\langle n(n-1) \rangle = \sum_{n=0}^{\infty} n(n-1)P(n). \quad (\text{A.6})$$

Substituting Eq. (A.6) into Eq. (A.5) we obtain

$$\langle n^2 \rangle = \langle n \rangle + \sum_{n=0}^{\infty} n(n-1) \frac{\langle n \rangle^n}{n!} e^{-\langle n \rangle}. \quad (\text{A.7})$$

Eq. (A.7) can now be simplified by noticing that $n(n-1)$ is the product of the last two terms in the $n!$ series, and that the summation can begin with $n=2$ since the $n=1$ and $n=0$ terms are both zero. In addition the constant factor $\langle n \rangle^2$ can also be pulled out of the summation to give

$$\langle n^2 \rangle = \langle n \rangle + \langle n \rangle^2 \sum_{n=2}^{\infty} \frac{\langle n \rangle^{n-2}}{(n-2)!} e^{-\langle n \rangle}. \quad (\text{A.8})$$

We now make a change of variable to $m=n-2$ and reduce Eq. (A.8) as follows [32]

$$\begin{aligned} \langle n^2 \rangle &= \langle n \rangle + \langle n \rangle^2 \sum_{m=0}^{\infty} \frac{\langle n \rangle^m}{m!} e^{-\langle n \rangle} \\ &= \langle n \rangle + \langle n \rangle^2 \sum_{m=0}^{\infty} P(m) \\ &= \langle n \rangle + \langle n \rangle^2. \end{aligned} \quad (\text{A.9})$$

Where we recall that the summation, over all m , of the Poisson distribution is exactly one.

This result can then be substituted into Eq. (A.3), which gives

$$\begin{aligned} \sigma^2 &= (\langle n \rangle + \langle n \rangle^2) - \langle n \rangle^2 \\ \sigma^2 &= \langle n \rangle. \end{aligned} \quad (\text{A.10})$$

Thus the variance of a Poisson distribution is equal to the mean. This result will now be used to find the mean squared fluctuation in the detector current.

If the current is monitored at the output of the detector for a period of time, τ the current measured would be

$$i = \frac{nq}{\tau}, \quad (\text{A.11})$$

where n is the number of electrons generated by the detector in time τ and q is the charge on an electron. The average current is

$$\langle i \rangle = \frac{\langle n \rangle q}{\tau}. \quad (\text{A.12})$$

The mean squared fluctuation in the current, which can also be called the mean squared noise current, is

$$\begin{aligned} \langle i^2 \rangle &= \langle (i - \langle i \rangle)^2 \rangle \\ &= \left\langle \left(\frac{nq}{\tau} - \frac{\langle n \rangle q}{\tau} \right)^2 \right\rangle \\ &= \frac{q^2}{\tau^2} \langle (n - \langle n \rangle)^2 \rangle. \end{aligned} \quad (\text{A.13})$$

The second term in Eq. (A.13) is just the variance, which has been shown above is the mean. Using Eq. (A.12) the mean can be substituted and the mean squared noise current becomes

$$\langle i^2 \rangle = \frac{q}{\tau} I \quad (\text{A.14})$$

where I is used as the average current. Finally the sample time τ is equal to one over two times the bandwidth. This can be substituted into Eq. (A.14) to give the final form of the mean squared noise current, commonly known as shot noise [12]; that is

$$\langle i_{SN}^2 \rangle = 2qIB \quad (\text{A.15})$$

APPENDIX B

Chi² Goodness of Fit

A goodness of fit test determines whether a set of data can be viewed as a random variable with a given distribution. To test whether measured distribution actually fits the proposed theoretical distribution a level of significance (α) is chosen. For this work the level of significance used is 0.1, which means there is a $(1-\alpha)100 = 90$ percent confidence that the measured distribution fits the proposed theoretical distribution. One method of determining the goodness of fit is a chi-squared (χ^2) test. The χ^2 statistic is defined as [28]

$$\chi^2 = \sum_{j=1}^c \frac{(O_j - E_j)^2}{E_j} \quad (\text{B.1})$$

where O_j is the observed frequency (experimentally measured), E_j is the expected (theoretical) frequency and c is the number of classes. Equation (B.1) represents a random variable that has an approximate χ^2 -distribution with $c-1$ degrees of freedom. The number of degrees of freedom distinguishes between the members of the χ^2 -distribution family. When determining the number of degrees of freedom for the theoretical distribution the equation is

$$\text{Degrees of Freedom} = c - 1 - e \quad (\text{B.2})$$

where e is the number of estimated or calculated parameters in the theoretical distribution and c in my case, as will be seen later, is the number of bins in a histogram. Examples of

estimated parameters would be the mean and/or the variance used in the theoretical distribution when they were measured from the data.

The χ^2 distribution is a tabulated function that can be seen listed below dependent on the number of degrees of freedom and the level of significance. To demonstrate how to use this table we will use a 0.1 level of significance and 24 degrees of freedom. Looking at Table B1 the number of degrees of freedom (D of F) is shown in the left most column and 1-(level of significance) is shown in the top row. To use this table follow down the D of F

Table B1: Tabulated values of Chi²

D of F	1 - Level of Significance														
	0.995	0.99	0.975	0.95	0.9	0.8	0.7	0.6	0.5	0.4	0.3	0.2	0.1	0.05	0.025
1	7.68	6.63	5.02	3.84	2.71	1.64	1.07	0.71	0.46	0.27	0.16	0.06	0.02	0.00	0.00
2	10.00	9.21	7.38	5.99	4.61	3.22	2.41	1.83	1.39	1.02	0.71	0.45	0.21	0.10	0.06
3	12.84	11.34	9.35	7.61	6.26	4.64	3.66	2.95	2.37	1.87	1.42	1.01	0.58	0.38	0.22
4	14.66	13.28	11.14	9.49	7.78	6.00	4.88	4.04	3.36	2.75	2.19	1.68	1.06	0.71	0.48
5	16.75	15.09	12.63	11.07	9.24	7.29	6.06	5.13	4.35	3.66	3.00	2.34	1.61	1.16	0.83
6	18.65	16.81	14.45	12.69	10.64	8.66	7.23	6.21	5.35	4.67	3.83	3.07	2.20	1.64	1.24
7	20.26	18.48	16.01	14.07	12.02	9.80	8.38	7.26	6.36	5.49	4.67	3.82	2.83	2.17	1.69
8	21.96	20.09	17.63	15.51	13.36	11.03	9.62	8.35	7.34	6.42	5.63	4.59	3.49	2.73	2.18
9	23.09	21.67	19.02	16.92	14.66	12.24	10.66	9.41	8.34	7.36	6.39	5.38	4.17	3.33	2.70
10	25.19	23.21	20.49	18.31	15.99	13.44	11.78	10.47	9.34	8.30	7.27	6.18	4.87	3.94	3.26
11	26.76	24.73	21.92	19.68	17.28	14.63	12.90	11.63	10.34	9.24	8.18	6.99	5.68	4.57	3.82
12	28.30	26.22	23.34	21.03	18.65	16.81	14.01	12.56	11.34	10.18	9.03	7.81	6.30	5.23	4.40
13	29.82	27.69	24.74	22.36	19.81	16.98	16.12	13.64	12.34	11.13	9.93	8.63	7.04	5.89	5.01
14	31.32	29.14	26.12	23.68	21.06	18.16	16.22	14.69	13.34	12.08	10.82	9.47	7.79	6.67	5.63
15	32.80	30.58	27.49	25.00	22.31	19.31	17.32	15.73	14.34	13.03	11.72	10.31	8.56	7.26	6.26
16	34.27	32.00	28.85	26.30	23.84	20.47	18.42	16.78	15.34	13.98	12.62	11.16	9.31	7.96	6.91
17	35.72	33.41	30.19	27.59	24.77	21.61	19.81	17.82	16.34	14.94	13.63	12.00	10.09	8.67	7.56
18	37.16	34.81	31.83	28.87	25.99	22.76	20.60	18.87	17.34	15.89	14.44	12.86	10.86	9.39	8.23
19	38.68	36.19	32.85	30.14	27.20	23.90	21.69	19.91	18.34	16.85	15.35	13.72	11.66	10.12	8.91
20	40.00	37.67	34.17	31.41	28.41	26.04	22.77	20.95	19.34	17.81	16.27	14.58	12.44	10.86	9.59
21	41.40	38.93	35.48	32.67	29.52	26.17	23.86	21.99	20.34	18.77	17.18	15.44	13.24	11.89	10.28
22	42.80	40.29	36.78	33.92	30.81	27.30	24.94	23.03	21.34	19.73	18.10	16.31	14.04	12.34	10.96
23	44.18	41.64	38.08	35.17	32.01	28.43	26.02	24.07	22.34	20.69	19.02	17.19	14.86	13.09	11.66
24	45.56	42.98	39.36	36.42	33.20	29.85	27.10	26.11	23.34	21.65	19.94	18.06	16.66	13.85	12.40
25	46.93	44.31	40.66	37.65	34.38	30.68	28.17	26.14	24.34	22.62	20.87	18.94	16.47	14.61	13.12
26	48.29	45.64	41.92	38.89	35.66	31.79	29.25	27.18	25.34	23.68	21.79	19.82	17.29	15.38	13.84
27	49.65	46.96	43.19	40.11	36.74	32.91	30.32	28.21	26.34	24.64	22.72	20.70	18.11	16.16	14.57
28	50.99	48.28	44.46	41.34	37.92	34.03	31.39	29.25	27.34	25.51	23.65	21.69	19.94	16.93	15.31
29	52.34	49.69	46.72	42.65	39.09	35.14	32.46	30.28	28.34	26.46	24.68	22.48	19.77	17.71	16.06
30	53.67	50.89	46.96	43.77	40.26	36.25	33.63	31.32	29.34	27.44	25.51	23.36	20.60	18.49	16.79
31	55.00	52.19	48.23	44.00	41.42	37.36	34.60	32.35	30.34	28.41	26.44	24.26	21.43	19.28	17.64
32	56.33	53.49	49.49	46.19	42.58	38.47	35.65	33.38	31.34	29.38	27.37	25.15	22.27	20.07	18.29
33	57.65	54.78	50.73	47.40	43.76	39.57	36.73	34.41	32.34	30.34	28.31	26.04	23.11	20.87	19.05
34	58.96	56.06	51.97	48.60	44.90	40.68	37.80	35.44	33.34	31.31	29.24	26.94	23.95	21.66	19.81
35	60.27	57.34	53.20	49.80	46.06	41.78	38.86	36.47	34.34	32.26	30.18	27.84	24.80	22.47	20.67
36	61.68	58.62	54.44	51.00	47.21	42.68	39.92	37.50	35.34	33.25	31.12	28.73	25.64	23.27	21.34
37	62.88	59.89	55.67	52.19	48.36	43.98	40.98	38.53	36.34	34.22	32.05	29.64	26.49	24.07	22.11
38	64.18	61.16	56.90	53.38	49.51	45.08	42.05	39.55	37.34	35.19	32.99	30.54	27.34	24.88	22.88
39	65.48	62.43	58.12	54.57	50.66	46.17	43.11	40.59	38.34	36.16	33.93	31.44	28.20	25.70	23.65
40	66.77	63.69	59.34	55.76	61.81	47.27	44.16	41.62	39.34	37.13	34.87	32.34	29.06	26.61	24.43
41	68.05	64.95	60.66	56.94	52.95	48.36	45.22	42.65	40.34	38.11	35.81	33.25	29.91	27.33	25.21
42	69.34	65.21	61.78	58.12	54.09	49.45	46.28	43.68	41.34	39.09	36.75	34.16	30.77	28.14	26.00
43	70.62	67.46	62.99	59.30	55.23	50.65	47.34	44.71	42.34	40.05	37.70	35.07	31.63	28.98	26.79
44	71.89	68.71	64.20	60.46	56.37	51.64	48.40	45.73	43.34	41.02	38.64	35.97	32.49	29.79	27.67
45	73.17	69.96	65.41	61.66	57.81	52.73	49.45	46.76	44.34	42.00	39.58	36.98	33.36	30.61	28.37
46	74.44	71.20	66.62	62.63	58.64	53.82	50.51	47.79	45.34	42.97	40.63	37.80	34.22	31.44	29.16
47	75.70	72.44	67.82	64.00	59.77	54.91	51.56	48.81	46.34	43.94	41.47	38.71	35.08	32.27	29.96
48	76.97	73.68	69.02	65.17	60.91	55.99	52.62	49.84	47.34	44.92	42.42	39.62	36.96	33.10	30.76
49	78.23	74.92	70.22	66.34	62.04	57.06	53.67	50.87	48.33	45.89	43.37	40.63	36.82	33.93	31.55
50	79.49	76.15	71.42	67.60	63.17	58.10	54.72	51.89	49.33	46.85	44.31	41.45	37.69	34.76	32.36

column until 24 degrees of freedom is found, then go across to the column that is 0.9, which gives a χ^2 of 33.2. So in order to accept a theoretical fit to a set of data the χ^2 of that data must not be more than 33.2.

BIBLIOGRAPHY

- [1] M.I. Skolnik, *Introduction to Radar Systems*, McCraw-Hill, New York, 1962.
- [2] C.G. Bachman, *Laser Radar Systems and Techniques*, Artech House, Massachusetts, 1979.
- [3] P.W. Milonni, J.H. Eberly, *Lasers*, John Wiley & Sons, New York, 1988.
- [4] A.V. Jelalian, *Laser Radar Systems*, Artech House, Massachusetts, 1992.
- [5] M.J. Kavaya, A.W. Henderson, E. Russell, R.M. Huffaker, R.G. Frehlich, "Monte Carlo Computer Simulations of Ground-Based and Space-Based Coherent DIAL Water Vapor Profiling," *Applied Optics*, Vol. 28, No. 5, March 1989, pg. 840.
- [6] S.W. Henderson, *Eyesafe Solid-State Coherent LIDAR System for Wind and Water Vapor Measurements*, Technical Report CTI-TR-9008, 1991.
- [7] Coherent Technologies, Inc., P.O. Box 7488, Boulder, CO, 80306-7488.
- [8] J.W. Goodman, "Comparative Performance of Optical Radar Detection Techniques", *IEEE Transactions on Aerospace and Electronic Systems*, Vol. ALS-2, No. 5, September, 1966, pgs. 526-535.
- [9] R.J. Keyes, "Heterodyne and Nonheterodyne Laser Transceivers," *Rev. Sci. Instrum.*, 57, 4, April 1986, pgs. 519-528.
- [10] D. Sliney, M. Wolbarsht, *Safety with Lasers and Other Optical Sources*, Plenum Press, New York, 1980.
- [11] D.P. Beneditz, R.L. Lindsey, J.A. Labo, "Integrated Laser Hazard Assessment Program," "LHAZ," Ver. 2.0, Brooks A.F.B., TX, 1992.
- [12] R.H. Kingston, *Detection of Optical and Infrared Radiation*, Springer-Verlag, New York, 1978.
- [13] A. Yariv, *Optical Electronics 3rd Ed.*, Holt, Rinehart and Winston, Inc., New York, 1985.

- [14] S.O. Rice, "Mathematical analysis of random noise," *Bell System Technical Journal*, Vol 23, pg 282, 1944; Vol 24, pg 46, 1945.
- [15] J.W. Goodman, "Some Effects of Target-Induced Scintillation on Optical Radar Performance", *Proceedings of the IEEE*, Vol 53, No 11, Nov 65, pg 1693.
- [16] J.W. Goodman, *Statistical Optics*, John Wiley & Sons, New York, 1985.
- [17] M.D. Rotondaro, "Continuous Wave and Pulsed Scloid State Laser Model," Thesis, Air Force Institute of Technology, Academic Library, 1990.
- [18] M. Born and E. Wolf, *Principles of Optics*, Pergamon Press, NY, 1980, p. 398.
- [19] D. Fink, "Coherent Detection Signal-to-Noise," *Applied Optics*, Vol. 14, No. 3, March 1975, p. 689.
- [20] "Detection Circuits for Coherent Laser Radar," CTI Boulder, CO.
- [21] "Amplifier Specifications," Analog Modules, Inc., Longwood FL.
- [22] "Amplifiers to 2 GHz," Miteq, Hauppauge, NY.
- [23] RCA, *Electro-Optics Handbook*, Commercial Engineering, Harrison, NJ, 1974.
- [24] Optical Filter Corporation, specification sheet, part #NO2099.
- [25] *The Infrared Handbook*, editors W.L. Wolfe, G.J. Zissis, The Infrared Information & Analysis Center, Environmental Research Institute of Michigan, 1985.
- [26] private communication with A.V. Jelalian, Aug. 2, 1993.
- [27] "Pyroelectric Joulemeter, Molelectron Detector J25/J50," Molelectron Detector Inc., Operators Manual, Nov. 1990
- [28] R.M. Bethea, B.S Duran, T.L. Boullion, *Statistical Methods for Engineers and Scientists*, Marcel Dekker, Inc., New York, 1985.
- [29] J.E. Freund, *Mathematical Statistics*, 2nd ed., Prestice-Hall, Inc., Englewood Cliffs, New Jersey, 1971.
- [30] D.M. Papurt, J.H Shapiro, S.T. Lau, "Measured Turbulence and Speckle Effects in Laser Radar Target Returns," *Coherent Infrared Radar Systems and Applications II*, SPIE, Vol. 415, 1983.

- [31] J.H. Shapiro, S.T.Lau, "Turbulence Effects on Coherent Laser Radar Target Statistics," *Applied Optics*, Vol. 21, July 1, 1982, pgs. 2395-2398.
- [32] R.W. Boyd, Radiometry and the Detection of Optical Radiation, John Wiley & Sons, New York, 1983, p. 131.

VITA

October 9, 1968	Born-Lafayette, Indiana
1990-91	Lab Assistant, Center for Applied Optics, Rose-Hulman Institute of Technology
1991	B.S., Applied Optics, Rose-Hulman Institute of Technology, Terre Haute, Indiana
1991	Research Assistant, Rose-Hulman Institute of Technology, Terre Haute, Indiana
1991	Research Assistant, University of Dayton, Dayton, Ohio
1993	Junior Electro-Optic Engineer, Technology/Scientific Services, Inc.

PUBLICATIONS

Lt. Scott H. McCracken, Jay A. Overbeck, "Frequency Chirping a 2.09 μ m Laser Radar Pulse Using a Pockels Cell," Technical Memorandum, WL-TM-92-103, February 1992.

Jay A. Overbeck, Bradley Duncan, Paul McManamon, Scott McCracken, "Eye-safe lidar at 2.09 μ m," Optical Society of America, Annual Meeting, Albuquerque, New Mexico, September 25, 1992.

Jay A. Overbeck, Capt. Scott H. McCracken, Bradley, D. Duncan, "Coherent Versus Incoherent Eyesafe LIDAR Detection at 2.09 μ m," NAECON 93, May 24-28, 1993, Vol. 2, pgs. 1142-1147.

Jay A. Overbeck, Martin B. Mark, Scott H. McCracken, Paul F. McManamon, Bradley D. Duncan, "Coherent versus Incoherent LADAR Detection at 2.09 μ m," *Optical Engineering*, November 1993.